

Adsorption in Confined Aqueous Films

Prudhvidhar Gaddam

Dissertation submitted to the faculty of the Virginia Polytechnic Institute and State University in partial fulfillment of the requirements for the degree of

Doctor of Philosophy

In

Chemical Engineering

William A. Ducker

Scott T. Huxtable

Richey M. Davis

Stephen M. Martin

June 11th, 2019

Blacksburg, Virginia

Keywords: adsorption, surface excess, colloids, thin films, electrolytes, Debye-length

Adsorption in Confined Aqueous Films

Prudhvidhar Gaddam

ABSTRACT

This thesis describes direct measurements of equilibrium adsorption of ions in thin (< 100 nm) aqueous films. Adsorption in thin films is important because it is through adsorption that the stability of colloidal suspensions is frequently tuned. The vast majority of measurements of adsorption to date have been to a *single* interfaces, whereas the subject of this thesis is adsorption in a thin film between *two* interfaces. There are two isolated interfaces when particles in a suspension are far apart, but during the collision, a thin film forms between the particles, and the properties of the thin film determines the stability of the colloid. Thus, adsorption in the thin film determines the stability of the colloidal dispersion. There is a distinct gap in the scientific literature concerning adsorption in thin films mainly because there is no technique for measuring such adsorption. To fill this gap in knowledge, I first developed of a technique to directly measure adsorption in thin films, and then applied this technique to explore the behavior of co-ions near charged interfaces as a function of bulk solution composition and the thickness of the film.

The adsorption behavior of fluorescein, a di-anion, to negatively charged silica interfaces was studied in dilute electrolytes. The focus was on the effect of the electrostatic screening length, or Debye-length. The separation was measured using interference microscopy and the adsorption of fluorescein was measured using fluorescence microscopy. The Debye-length was altered by variation of the background salt (NaCl) concentration in dilute (<1 M) solution. The surface excess of adsorption for fluorescein was shown to depend on both the Debye-length and the separation distance between two interfaces. Increasing the Debye-length from 4 nm to 21 nm increased the plateau surface excess at large separations, and decreasing the separation lead to a monotonically decreasing surface excess. The surface excess varied over a range that scaled with the Debye-length. The results were compared to solution of the Poisson-Boltzmann model and good agreement was found between the model and the experiment.

The effect of background salt concentration on fluorescein adsorption was also studied in concentrated electrolytes (2.5 – 10 M) for various monovalent salts (LiCl, NaCl and CsCl). The results showed that the fitted electrostatic screening length showed an opposite trend to predictions from Poisson-Boltzmann, with the screening-length *increasing* with *increasing* salt concentration. That is, the Debye-length prediction was quantitatively incorrect and predicts the incorrect trend. For example, in 10 M LiCl where the Debye-length is 0.1 nm, and therefore colloidal chemists would traditionally predict that double-layer forces are negligible, my results show that the actual decay length is about 10 nm, which is about the same as in 10^{-3} M LiCl solution. The rate of increase of screening-length as a function of concentration was also an ion specific effect. In addition, the results show that there is an inversion of the surface charge in concentrated salt solution.

The original device on which all the above measurements were made had two limitations: (1) the maximum film thickness was 50 nm and (2) the film was asymmetric, which hampered calculation of the surface excess and increased the number of degrees of freedom in modeling of the adsorption. In the last part of my thesis, I describe development of a symmetric sample which (1) enables measurement of films up to 1 μm , (2) simplifies modeling of the optics by eliminating optical interference of the fluorescence excitation, and reduces the number of parameters when comparing to models.

Adsorption in Confined Aqueous Films

Prudhvidhar Gaddam

GENERAL AUDIENCE ABSTRACT

This thesis aims to understand the behavior of electrically charged molecules and atoms in thin nanometer scale (< 100 nm) liquid films subject to confinement between two charged interfaces. This situation frequently arises in colloidal suspensions, which consist of tiny sub-microscopic particles (colloid), droplets and large molecules dispersed in a second continuous medium. The stability of these suspensions, i.e. whether the colloidal materials agglomerate and sediment out of the suspension or remain stably suspended, depends on the surface forces between their interfaces during collision events, which frequently arise due to Brownian motion. As the fluid between particles thins as they approach each other during these collision events, the behavior of the dissolved molecules can be significantly different than when they are far apart due to the presence two interacting interfaces. Typically the dissolved molecules are used to tune the surface forces and understanding their behavior in confinement is relevant to a colloid scientist whose aim is to tune the behavior of the suspension.

In the first part of this work, a technique is developed that serves as the static analogue to colloidal objects colliding with each other. The equilibrium behavior of a negatively charged fluorescent ion is measured as a function of film thickness and background salt concentration between two negatively charged interfaces. The Poisson-Boltzmann model predicts that with decreased salt concentration, there is a greater magnitude of depletion of the fluorescent ion at large separations and the characteristic length over which there is a change in the magnitude of depletion increases. Good agreement is found between the model and the experiment validating the technique developed and providing the first direct observation of molecular behavior subject to confinement as a function of solution composition.

This effect of background salt type and concentration was tested for concentrated electrolytes as well. The experimental results showed an opposite trend to predictions from the Poisson-Boltzmann model. The fluorescent ion was now adsorbed to negatively charged interfaces indicating that the negatively charged interfaces were now positively charged. The magnitude of adsorption at large separations and characteristic length over which the magnitude of adsorption changes was a function of the salt concentration and the ion type.

Finally, improvements were made to the original device to overcome limitations with the original device. The limitations were that (1) the maximum film thickness was 50 nm and (2) the interfaces were asymmetric which complicated theoretical calculations of the equilibrium behavior of the ions. In the last part of my thesis, I develop a sample which (1) enables measurements of films up to 1 μm and (2) simplifies the optical modeling necessary in the first two sections of this thesis

Acknowledgements

Much of the work presented here would not have been possible without the guidance and support of a large number of people. A scientific and personal endeavor such as a PhD. is rarely a lone pursuit and getting through to the finish line is a team effort.

First and foremost, I am thankful for my wife, Stephanie Gaddam without whose support I do not think I would be here. She supported me when I was going through a tough time navigating what my project was going to be during the initial stages of my PhD, and she encouraged me when things started going well. She has been the rock in my life during the majority of this endeavor. I would also like to thank my friends Nick Merrill, Kate Vance, Marcus Thoreson, and Daniel Perkins who gave me the emotional support and help I needed to push through to the end.

A special thanks is in order for Robert Grayson, an undergraduate who worked with me on this project and holds a special place in my heart. It is rare to have an undergraduate who is so dedicated to a project and seeing him succeed inspired me and pushed me to work harder and think smarter. I loved talking about science, philosophy and love with him and can't wait to read and hear about his scientific achievements.

I am thankful for my mentor, Dr. William Ducker. I learned how to become a better scientist by opening myself to the idea that science is just as creative a pursuit as any other. I also learned how to be a better person and to take pride in my work and push myself to follow goals worthy of myself. I will miss his sense of humor dearly upon my ejection from this decade long education from Virginia Tech. I would also like to thank my co-advisor Dr. Scott Huxtable, with whom I worked during the first few years of my PhD, for giving me the guidance and allowing me the flexibility when it looked like the project I started on began going in a different direction.

I would like to thank my labmates Yow-Ren Chang, Zechen Zhang, Jon Hittel, Alfred Ritter and Alex Kriegel for making work an enjoyable experience. I would also like to thank Don Leber, the manager of the clean room, for his expert guidance regarding microfabrication and his training to perform much of the research presented in this work.

Table of Contents

Chapter 1. Introduction	1
1. Significance	1
1.1 Motivation	1
1.2 Adsorption to a single interface	2
1.3 Adsorption to a thin film between two planar interfaces	3
1.3 Current methods of measuring adsorption in confinement	4
2. Technique	5
2.1 Analogy between particle collision and CAA	5
2.2 Realization of CAA	6
2.2.1 Sample Preparation	6
2.2.2 Vary the Separation, D	6
2.2.3 Measurement of Separation	7
2.2.4 Measurement of Number of Molecules	8
2.3 Experiments	9
3. Theory	9
3.1 The Double-Layer at an Isolated Interface	9
3.2 The Poisson-Boltzmann Equation	9
3.3 The Debye-length	11
3.4 Surface Charging at an Interface	12
3.5 The Double-layer in a Thin Film between Two Interfaces	14
3.5.1 Symmetric Constant Surface-potential Boundary Condition	14
3.5.2 Constant-charge Boundary Condition	15
4. Literature Review	17
4.1 Measurement of adsorption to a single interface	17
4.2 Measurement of Ion Profile using Standing X-Ray Waves	17
4.3 Force Measurements in Electrolytes	20
4.4 Proximal Adsorption from Force Measurements in Aqueous Surfactants Solutions	21
Chapter 2. Effect of background electrolyte concentration on surface excess of fluorescein dianion in dilute electrolytes	25
Introduction	27
Analysis	29
Strategy for Measuring Surface Excess	29
Measurement of Thickness: Interference	30
Measurement of Amount: Fluorescence	31
Experimental	35
Modeling of Ion Density	35
Results	37
Validation of Optical Model	37
Qualitative Interpretation of Amounts in the Crack	38
Quantitative Analysis of the Amounts in the Crack	39
Effect of Fluorescein Equilibria	41
Discussion	42
Determination of the Molecular Distribution, $n(z)$, from the Fluorescence Emission	42
Measurement of Surface Potential	42
Conclusions	42

Supporting Information	43
Chapter 3. Effect of background electrolyte concentration on surface excess of the fluorescein dianion in concentrated electrolytes	44
Introduction	46
Experimental	49
Results	51
Surface Excess in Concentrated Salt	51
Quantification of Decay-Length in Concentrated Salt Solution	52
Model-Dependent Decay-Length	53
Discussion	55
The Decay Length	55
Charge Reversal	56
Comparison of Optical Model and Experiment for Thick Films	58
Conclusions	58
Supporting Information	59
Chapter 4. Symmetrical glass-glass based CAA	60
Motivation	60
Optical Modeling	61
Results	62
Discussion	64
Chapter 5. Future Work	65
Chapter 6. Conclusions	66
Appendix	67
Appendix A: Supplemental Information for Chapter 2	67
Appendix B: Supplemental Information for Chapter 3	76
Appendix C: Methods for fabrication of silica-glass and glass-glass cracks	87
References	89

List of Figures

Chapter 1. Introduction

- Fig. 1.** Three different concentration profiles for a thin confined film. The blue shaded area represents a case where there is positive adsorption i.e. surface excess is positive (Eq 2a > Eq 2b). The green shaded area represents a case where there is negative adsorption or depletion i.e. surface excess is negative (Eq 2a < Eq 2b) 4
- Fig. 2.** Correspondence between particle collision and crack. For the particle collision, the film thickness varies with time whereas for the crack, the film thickness varies with spatial location. In our apparatus, the crack geometry is invariant perpendicular to the page. 6
- Fig. 3.** Photograph of a bonded construct formed by bonding a silica and silicon wafer. At the perimeter of the wafer is a thin crack. 7
- Fig. 4.** Example of images obtained from the CAA. Interference (used to measure the separation, D) and its corresponding fluorescence image (used to obtain the total number of molecules). The separation increases left of the crack tip, represented by the dotted red line. Below is a cross sectional view of the crack showing how the separation varies as a function of the x -position. All images were captured in black and white but have been colorized to represent the frequency of optical filter prior to the camera. 8
- Fig. 5.** Comparison between low-potential and numerical solution of potential as a function of distance from the Poisson-Boltzmann equation for an interface with a surface potential of 150 mV and a Debye-length of 10 nm. 11
- Fig. 6.** Concentration profiles of a monovalent electrolyte for three Debye-lengths. Red represents the counter-ion and blue the co-ion. The surface potential used for these calculations here is $\psi_0 = 25$ mV. As the Debye-length is increased the distance from the interface there still exists a perturbation from the bulk concentration also increases 12
- Fig. 7.** Surface excess as a function separation calculated for a monovalent tracer ion interacting with charged interfaces in background electrolytes of varying Debye-lengths and a boundary condition of a constant symmetrical surface potential of -25 mV using the low-potential approximation. The blue lines represent positive ions or counter-ions and the red lines represent negative ions or co-ions. Co-ions are negatively adsorbed with adsorption decreasing as a function of separation for all Debye-lengths. 15
- Fig. 8.** Surface excess as a function of separation calculated for a monovalent tracer ion interacting with charged interfaces in background electrolytes of 10 nm Debye length and with a surface charge density, $\bar{\sigma}_0 = 1.59 \times 10^{-3} \frac{\text{C}}{\text{m}^2}$, $\psi_0 = 25$ mV for the different boundary conditions. The blue lines represent counter-ions and the red lines represent co-ions. Co-ions are negatively adsorbed with adsorption decreasing as a function of separation for all Debye-lengths. Calculations used the low potential approximation. 16
- Fig. 9.** Schematic of experimental system probed in X-Ray Standing Wave technique. From Ref 39. Reprinted with permission from AAAS 18
- Fig. 10.** Experimental data for the fluorescence intensity, represented by the filled dots and theoretical intensity represented by the solid and dashed lines using Eq 21. The solid line represents an ion profile from Poisson-Boltzmann and the dashed line is the Helmholtz model for the electrical double layer where counter-ions adsorb onto the surface neutralizing surface charge and there is no diffuse double layer. From Ref 39. Reprinted with permission from AAAS 19
- Fig. 11.** The interaction energy between two interacting crossed mica cylinders in the surface forces apparatus measured for salt concentrations from 10^{-1} to 10^{-4} . The solid lines represent 20

fits of forces calculated from DLVO theory where surface potential and decay lengths are the only fitting parameters. Reprinted by permission from Springer Nature: Nature, Ref 11, 1991.

Fig. 12. Interaction energy as a function of separation for surfactant concentrations from cmc/2000 to cmc/10. Here distance is given as $(S - S_0)$ where S is the separation between the bare silica surfaces and S_0 is the separation where the authors judged that the aqueous film thickness went to zero. Reprinted (adapted) with permission from Ref 46. Copyright 2001 American Chemical Society. 22

Fig. 13. Interaction energy and the gradient in interaction energy as a function of chemical potentials for a range of separations. At large and intermediate separations, below the cmc the gradient is roughly monotonic. The oscillations at small separations are due to the noise in the data in the lower left figure but are real in lower right figure where measurements are done significantly above the cmc. Reprinted (adapted) with permission from Ref 46. Copyright 2001 American Chemical Society. 23

Fig. 14. Proximal adsorption as a function of separation for CTAB. The filled circles are changes in surface excess assuming that $\Delta\Gamma_{Br} = 0$ and the open circles are if $\Delta\Gamma_{Br} = \Delta\Gamma_{CTA}$. The positive values at small separation indicates net adsorption i.e. there are more molecules per nm² than at infinite separation. Reprinted (adapted) with permission from Ref 46. Copyright 2001 American Chemical Society. 24

Chapter 2. Effect of background electrolyte concentration on surface excess of the fluorescein dianion in dilute electrolytes

Fig. 1. Schematics showing (a) proximal adsorption, and (b) the experimental sample. Films of different thickness, D , are created between the glass and silicon oxide. The sample is similar to a crack, and we refer to portion where $D \rightarrow 0$ as the crack tip. 27

Fig. 2. Schematic showing light rays contributing to interference and a subset (I', I'') of the possible multiply-reflected rays 30

Fig. 3. Schematic of fluorescence intensity. 31

Fig. 4. Intensity of emission of fluorophores calculated for three oxide film thicknesses: 2 nm, 38 nm, and 149 nm. Each plot is shown as a function of scaled distance in the film (z/D) and for 4 different film thickness, $D = 10$ nm (solid line), $D = 25$ nm (dashed), $D = 50$ nm (dot-dashed) and $D = 215$ nm (dotted). The top row shows the intensity, and the bottom row shows the Deviation from mirror symmetry about $z/D = 0.5$. Deviation is defined as $\frac{I_j(z,D) + I_j(D-z,D)}{2 \int_0^D I_j(z,D) dz} - 1$ 34

Fig. 5. Relative error in amount when assuming a uniform concentration profile. $\epsilon = \frac{|n_T(D) - n_u(D)|}{n_T(D)}$ where T is the amount calculated for the true profile and u is the amount calculated assuming a uniform distribution. 34

Fig. 6. Comparison between optical model (Eq. 11) and measurement of fluorescence intensity for 67 μ M fluorescein at pH 7.6 and $\kappa^{-1} = 0.5$ when the oxide layer is 37 nm thick. The vertical axis has arbitrary units. The model is fit to the data for $D > 20$ nm with a constant scaling factor. The effect of uncertainty in the oxide thickness and the shape of the crack are shown in Fig. S4. 37

Fig. 7. Interference ($\lambda = 445$ nm) and fluorescence emission ($\lambda = 525$ nm) images of the thinnest part of the crack with Debye length indicated. The part of the crack at the top of each image has approximately zero thickness and the the brighter strip is the thinnest part of the crack. The dotted red line on the fluorescence image is a guide, determined from interferometry, that shows the approximate position of the crack tip, i.e. the boundary between where $D = 0$ above and > 0 below. 38

Fig. 8. Number, n , of fluorescein molecules per unit area, A , for solutions of constant fluorescein concentration, $C_{\text{Fl}} = 67 \mu\text{M}$. Results are shown for two Debye-lengths. $C_{\text{NaCl}} = 0.40 \text{ M}$ ($\kappa^{-1} = 0.50 \text{ nm}$), and $C_{\text{NaCl}} = 0 \text{ mM}$, ($\kappa^{-1} = 21 \text{ nm}$). Lines show the results from the PB model calculated using a surface potential of -70 mV that was obtained from fits of surface excess at infinite separation. Data is collected over the entire image (239,360 pixels) and binned using a bin width of 0.25 nm .	39
Fig. 9. Surface excess of fluorescein as a function of film thickness for different solution Debye lengths. The Debye-length was reduced by addition of NaCl. The PB model includes a fit to the surface potential at infinite separation, which was -65 , -50 , -50 and -70 mV for κ^{-1} of 4 , 7 , 14 and 21 nm respectively. The 7 nm data did not fit well to the model. Error bars are \pm standard error of measurements for three different crack chips.	40
Fig. 10. Difference in surface excess of fluorescein in thin film (separation shown) and for isolated film. Isolated film was $D = 65 \text{ nm}$ for 4 and 7 nm solutions and $D = 215 \text{ nm}$ for 14 and 21 nm solutions. The PB fit for the 7.3 nm solution has been omitted.	40
Fig. 11. Comparison of Surface Excess measurements at $\text{pH } 7.6$ and 8.4 . The surface excess was calculated assuming that all of the fluorescein is in the F^{2-} form. The effect of pH on the surface excess is slight.	41
Fig. 12. Comparison of surface potential measured from fluorescence intensity and from force measurements for the glass–silica system. AFM results from Ducker et al. ⁶⁵ Surfaces Forces measurement from Horn et al. ⁷⁵ The huge error bar for $\kappa^{-1} = 4 \text{ nm}$ indicates that our technique is not useful for measuring potential for this condition.	42
Chapter 3. Effect of background electrolyte concentration on surface excess of the fluorescein dianion in concentrated electrolytes	
Fig. 1. Schematic of the effect of salt concentration on the decay of double-layer forces. The experimental data is contained in refs ¹⁰³ and ⁹³	47
Fig. 2. (a) and (b) Interference ($\lambda = 445 \text{ nm}$) and (c) and (d) fluorescence emission ($\lambda = 525 \text{ nm}$) images of the thinnest section of the crack with the salt concentrations indicated. The dotted lines serve as an approximate guide to the eye for the $D = 0 - 30 \text{ nm}$ region, as determined from the interference image. Images have been colorized at the interference and emission wavelengths. (e) Schematic of the chip (not to scale). Note that z is the distance from the midplane of the thin film.	51
Fig. 3. Surface excess of fluorescein as a function of separation (aqueous film thickness) for various salt concentrations and salt cations. The top row (a – c) shows the effect of salt concentration and the bottom row (d – f) shows the effect of salt type at a constant salt concentration. Error bars are the \pm standard error of measurements for three to four replicates; examples of replicates are shown in the supporting information. For the 10 M LiCl solution, the results are consistent with a large amount of fluorescein very near the two solid-liquid walls.	52
Fig. 4. Surface excess of the isolated solid–liquid interfaces and empirical decay lengths and as a function of salt concentration obtained from Eq. 4.	53
Fig. 5. Decay length of the potential obtained from fits to the Poisson-Boltzmann equation (Eq. 6) assuming low potential and constant surface potential, and that the decay length is a fitting parameter, rather than obtained from Eq. 1.	54
Fig. 6. Test of the scaling relationship of Lee et al ⁹⁶ (Eq. 11) to the decay-lengths obtained from PB-fits to surface excess measurements (Fig. 6). The lines are least squared fits to the data for each ion, and have R^2 values of 0.98 for Li^+ and 0.99 for Na^+ .	55

Fig. 7. Effective fraction of ions dissociated as a function of salt concentration. The fraction of ions was determined from the decay length obtained in our work (Fig. 6) and Eq. 12. The error bars are the standard error from fits to experimental replicates.	56
Fig. 8. Surface charge density at infinite separation obtained from fits to Eq. 6. The error bars are the standard error from fits to experimental replicates.	56
Fig. 9. Comparison of measured fluorescence intensity and optical model of intensity. For a 0.5 M LiCl, the model is for a uniform distribution of molecules, and has been multiplied by an arbitrary constant to fit the measurements in the range 10–150 nm. The close correspondence between model and data supports the idea that the molecules are uniformly distributed in the 0.5 M NaCl, even for $D = 0–30$ nm. (see also Fig S9). For 10 M LiCl, two models are shown: (1) a uniform distribution represented by the dashed line and (2) the distribution calculated from the potential obtained from fit of the experimental data to the solution to the PB equation for a range of 0 – 30 nm assuming constant symmetrical potential.	57
Chapter 4. Symmetrical glass-glass based CAA	
Fig. 1. Comparison of measured fluorescence intensity and optical model of intensity. For a 0.5 M LiCl, the model is for a uniform distribution of molecules, and has been multiplied by an arbitrary constant to fit the measurements in the range 10–150 nm. The close correspondence between model and data supports the idea that the molecules are uniformly distributed in the 0.5 M NaCl, even for $D = 0–30$ nm. (see also Fig S9). For 10 M LiCl, two models are shown: (1) a uniform distribution represented by the dashed line and (2) the distribution calculated from the potential obtained from fit of the experimental data to the solution to the PB equation for a range of 0 – 30 nm assuming constant symmetrical potential.	61
Fig. 2. Calculated theoretical fluorescence emissions for ions in a thin film. The first column is the surface excess calculated from PB an ion with charge $\pm 2e$ for a constant symmetrical surface potential of $\psi_0 = 50$ mV with a 15 nm Debye-length. The second column is for the fluorescence emission for silicon–glass and the third column is for glass–glass. The top row is for co-ions and the bottom row is for counterions. Note that the intensity oscillations are much smaller for the glass–glass system.	62
Fig. 3. Interference (445 nm) and fluorescence images (Ex: 475 nm, Em: 525 nm) for a glass-glass chip infused with a solution where the fluorescein concentration is 50 μ M and a Debye-length is 0.5 nm with taken with a 10x objectives. The red dotted line represents separations to the left of which are 0 nm as the two glass surfaces are bonded together and to the right of which the intensity is increasing monotonically as a function of film thickness.	63
Fig. 4. Intensity as a function of separation for a glass-glass chip infused with a fluorescein in water (50 μ M, $\kappa_D^{-1} = 0.1$ nm). The linear fit to the data is performed from 20 – 300 nm. The R^2 value of the fit is 0.99.	63

List of Tables

Chapter 1. Introduction

Table 1. Surface density of ions as a function of pH. Reprinted (adapted) with permission from Ref 45. Copyright 2001 American Chemical Society 20

Chapter 2. Effect of background electrolyte concentration on surface excess of the fluorescein dianion in dilute electrolytes

Table 1. Refractive indices of layers 32

Chapter 2. Effect of background electrolyte concentration on surface excess of the fluorescein dianion in concentrated electrolytes

Table 1. Number of water molecules per NaCl unit and ion spacing 47

Chapter 1: Introduction

1. Significance

1.1. Motivation

Colloids are substances that consist of micro to nanoscale materials suspended in a continuous medium. Examples of colloids in everyday life include milk, which consists of fat globules, proteins etc. suspended in water, latex paint,¹ which consist of polymer particles pigments, binders and other additives suspended in aqueous medium and smoke and smog² where fine solids or liquids, respectively are suspended in air.

One of the defining features of colloids is their inherently small size. This leads to a large surface area to volume ratio which scales as $\sim \frac{1}{a}$, where a is the characteristic dimension of the colloidal object. Because of the existence of surface tension, there is an energy cost associated with dividing matter into small particles. This surface tension arises because a smaller particle has a larger fraction of its constituent molecules at the surface. Absent other forces, surface tension pulls these colloidal objects together to minimize the fraction of exposed surface molecules. For example, in liquid colloids, such as emulsified droplets in an aqueous medium, surface tension manifests as the coalescence of smaller droplets into a larger droplet to minimize the surface area.

In a suspension, colloidal objects exhibit random motion as a result of the bombardment of its surface by the thermal motion of molecules in the continuous medium. This random motion is known as Brownian motion. Brownian motion can lead to collisions between the particles, which can result in the formation of larger particles through coalescence (liquid droplets) or the formation of aggregates of particles (solids). The ability to continue to exist as separate entities is called the colloidal stability, and it depends on the potential energy as a function of separation. The forces that describe the potential energy are commonly described as surface forces because there are short ranged and depends on surface properties. When repulsive forces dominate, particles tend to stay stable in solution whereas when attractive forces dominate the suspension is unstable relative to coagulation: aggregates grow in size over time.

Colloidal particles are also subject to gravitational forces. The upper cut-off of 1 μm particles in the definition of a colloid arises because this is the size for which many particles will sediment to the bottom of a laboratory container in a period of a day. However, if the colloid is unstable relative to coagulation, then the particles will grow with time, and the rate of sedimentation will increase. In this way stability to coagulation and to sedimentation are linked.

Examples of stabilizing surface forces between colloidal matter are repulsive electrostatic interactions between like charged interfaces³ or steric interactions⁴ between molecules such as polymers grafted or adsorbed onto colloidal matter. Attractive surface forces can include attractive Van der Waals forces,⁵ depletion interactions⁶ or attractive electrostatic interactions between oppositely charged interfaces.

Adsorption of molecules is one of the tools available to a colloidal scientist to alter the stability of a suspension by tuning the interaction between the colloidal objects. Ions, surfactants, particles, polymers, etc. can be adsorbed onto the surface of a colloid to alter the surface forces experienced between the interfaces leading to the stabilization or destabilization of a colloid. For example, to stabilize a hydrophobic uncharged colloid in an aqueous suspension, whose tendency is to aggregate and sediment out of solution due to the attractive

van der Waals interactions between the particles, one can adsorb surfactants or graft amphiphilic polymers⁷⁻⁹ with charged head-groups and hydrophobic tails to the colloids. The now like-charged interfaces result in repulsive interactions if the particles approach each other and the suspension is stabilized. Many scientists have studied adsorption, but almost exclusively adsorption to isolated interfaces. Particle stability depends on the interaction between two interfaces, and therefore adsorption in the thin film between two interfaces is the relevant adsorption to study for particle stability. Adsorption to a single interface is not necessarily a good proxy for adsorption in a thin film because the fields from both interfaces affect adsorption.

The principal aim of the work in this dissertation is to examine adsorption in thin films between two interfaces, a topic of great practical importance that has rarely been studied.

The specific aims of my research presented in this dissertation are to

1. Develop a technique that can directly observe the static and dynamic behavior of molecules subject to confinement between two extended interfaces, and
2. To measure the equilibrium adsorption of ions and nanoparticles in thin films as a function of solution composition and distance, D , between the interfaces.

1.2. Adsorption to a Single Interface

As this thesis primarily deals with adsorption, it is important to give a specific definition of adsorption that is relevant to all interactions with interfaces. The IUPAC definition of adsorption is “An increase in the concentration of a dissolved substance at the interface of a condensed and a liquid phase due to the operation of surface forces.” For the work described here, the interface is always between a solid and a liquid. For a simple, one dimensional system, surface forces affect the concentration through the Boltzmann Distribution:

$$c_i(z) = c_i(\infty) \exp\left(-\frac{w_i}{kT}\right), \quad (1)$$

where w_i is the potential, k is the Boltzmann constant and T is the temperature for species i . w_i is the integral of the surface force, with the reference point at infinite distance from the solid:

$$w_i = - \int_{\infty}^z F_{\text{surface}} dz. \quad (2)$$

According to this definition what exactly would we regard as the interface and how far from the interface do we consider the “increase in concentration”? Surface forces usually decay with distance, either with a power law (e.g. Van der Waals) or exponentially (e.g. electrostatic double-layer forces) so the change in surface forces and thus the change in concentration persists out to infinite distance. In practice, the surface forces by definition decay rather rapidly (they often become negligible at 1– 100 nm from the surface) or else they would be described as bulk forces, but there is no clear cut-off. To deal with this problem Gibbs defined adsorption to include all molecules out to infinity.¹⁰ He defined adsorption as the difference between the number of molecules that are actually present and the number that would be present if the bulk concentration persisted right up to the solid,

$$\Gamma = \int_0^{\infty} c(z) - c_i(\infty) dz, \quad (3)$$

where $c_i(\infty)$ is the bulk concentration of molecule i .

The tricky part of this definition is that the location of the interface affects the result because it sets the limit of the integral. Gibbs' solution was to set the interface at a position where there was no adsorption of the solvent. In this case, the adsorption of a solute is described as the surface excess and is expressed per unit area of the interface.

1.2. Adsorption to a Thin Film between Two Planar Interfaces

In this thesis, I more or less follow the same definitions as described by Gibbs, but for two interfaces. In this case, there is no need to integrate to infinity (Eq. 3) one only need to consider the finite fluid that lies between the two interfaces. In this case, I define the surface excess to be:

$$\Gamma(D) = \left(\frac{n_i}{A}\right)_{\text{film}} - \left(\frac{n_i}{A}\right)_{\text{bulk}}, \quad (4)$$

where $\left(\frac{n}{A}\right)_{\text{film}}$ is the total number of molecules per unit area in the thin film and $\left(\frac{n}{A}\right)_{\text{bulk}}$ is the number of molecules in the thin film, should the film behave exactly as bulk. Mathematically, the right hand side of Eq 4 this can be represented in terms of the concentration profile in the thin film as

$$\left(\frac{n_i}{A}\right)_{\text{film}} = \int_{-D/2}^{D/2} c_i(z) dz \quad (5a)$$

$$\left(\frac{n_i}{A}\right)_{\text{bulk}} = \int_{-D/2}^{D/2} c_{i,\text{bulk}} dz = c_{i,\text{bulk}} D \quad (5b)$$

where $c_i(z)$ is the concentration profile in the thin film, D is the distance between the two solid–liquid interfaces, and $c_{i,\text{bulk}}$ is the bulk concentration of species i . Here the zero for the z coordinate is at the midplane of the film. The tricky part for Gibbs was to define the position of the interface; in this case, we need to carefully consider the distance between the two interfaces. In practice we are able to measure the distance between the interfaces rather accurately using interferometry, but errors in this measurement of D do propagate into errors in the surface excess.

Depending on the nature of the interactions between the substance of interest and the interface, Eq 5a can be larger than Eq 5b resulting in positive adsorption or what is referred to colloquially as just adsorption, or smaller, resulting in negative adsorption, also known as depletion. In this thesis I define adsorption to include both positive and negative adsorption. As described above, adsorption accounts for all molecules interacting with the interfaces regardless of the distance between the molecule and the interface.

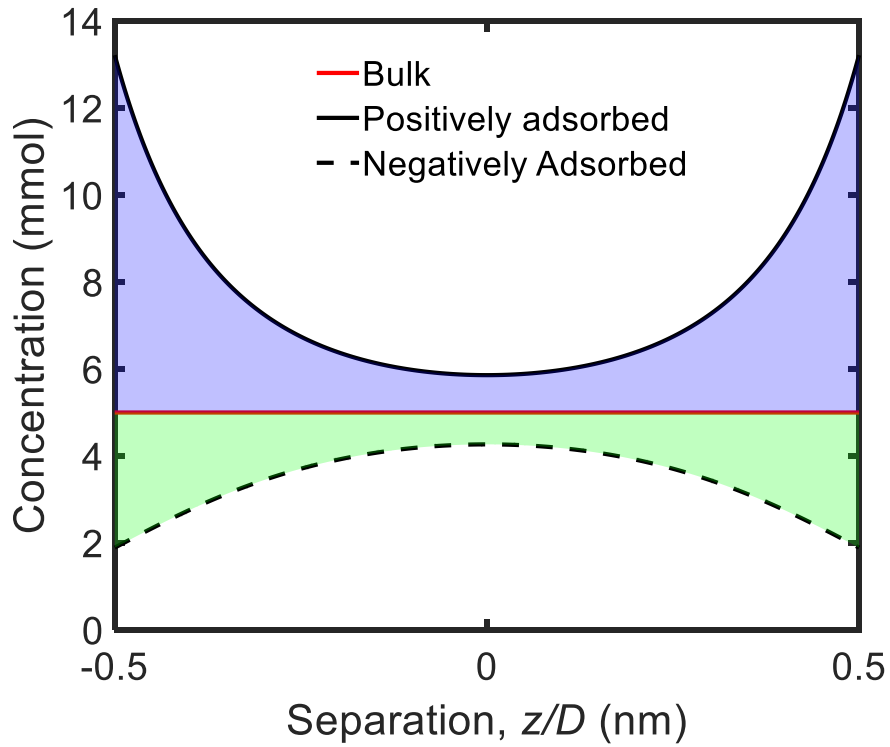


Fig 1: Three different concentration profiles for a thin confined film. The blue shaded area represents a case where there is positive adsorption i.e. surface excess is positive (Eq 2a > Eq 2b). The green shaded area represents a case where there is negative adsorption or depletion i.e. surface excess is negative (Eq 2a < Eq 2b)

1.3 Current Methods of Measuring Adsorption in Confinement

Currently, the only methods that exist to measure confined adsorption in nanoscale films are force measurements using techniques such as the Atomic Force Microscope (AFM)¹¹ or the Surface Forces Apparatus (SFA).¹² In these measurements two clean interfaces are brought close together while immersed in a solution. One surface is attached to a cantilevered spring and the force is calculated from the deflection multiplied by the spring constant. The force is measured as a function of separation between the surfaces.

Frequently, the data is fit to a theory, a common one being the Derjaguin, Landau, Verwey and Overbeek (DLVO) theory¹¹⁻¹³ which states the total interaction force experienced by two interfaces is the sum of the electrostatic and Van der Waals interactions. In situations where additional forces are present, such as structural or hydrophobic forces, additional terms are added such that the measured F_{Total} is

$$F_{\text{Total}} = F_{\text{VdW}} + F_{\text{ES}} + F_{\text{EF}}, \quad (6)$$

where F_{VdW} are the Van der Waals forces, F_{ES} are the electrostatic forces and F_{EF} are the extra force terms added to the equation to describe the total force experienced.¹⁴⁻¹⁷ From this model, parameters associated with the profile of adsorbed materials in confinement are extracted and the surface excess can be calculated as a function of separation. It is important to note that only the total force is measured and the division into components depends on definitions. The calculation of the various force contributions then depends on a model for the system. For example, the double-layer force is frequently described in terms of point ions and smeared potentials. With these assumptions, a surface potential can be extracted and thence an estimate of

the surface excess of molecules can be obtained. A critical aspect is that the interpretation depends on models. In contrast, the method described in this thesis does not rely on a model, it is a direct measure, and thus is useful for testing models of adsorption.

Alternatively, the surface excess can be determined from surface forces using a thermodynamic arguments, i.e. independent of a model. This will be discussed further in the *Literature Review* section.

The primary weakness of using force measurements is that all of these measurements are indirect measurements of adsorption. Molecular adsorption is inferred from the force between interfaces rather than measurement of a signal directly related to the number of molecules.

One of the purposes of the research presented in this dissertation is to overcome this limitation through the development of a technique to directly measure the adsorption behavior of materials subject to confinement and subsequently perform these direct measurements in a variety of systems.

2. *Technique*

The first phase of this project involved the development of a technique, which we have termed the “Confined Adsorption Analyzer”. The direct measurement of surface excess in a thin film requires the ability to:

1. Prepare a sample
2. Vary the separation, D , between two surfaces with nanometer resolution
3. Measure the separation.
4. Directly access the total number of molecules in the thin film.

2.1. *Analogy between particle collision and CAA*

Ideally, we would like to measure the adsorption as a function of the distance between two particles. This is a daunting task because particle collisions occur over a narrow time window ($ms-\mu s$), at a range of positions and orientations. The area of overlap is adsorption layers is very small and the amount of material at the interface is very small. Instead of studying a collision, we study a crack (See Fig. 4). The crack is fixed in position and orientation. Instead of studying a time series of film thicknesses, as in a collision, I have studied a static series of film thicknesses. Thus, I study the adsorption in the crack at equilibrium, which is directly related to the adsorption on the particles when the timescales of diffusion and adsorption are much faster than the timescales of collision. For the crack, the film thickness is a continuous variable. In experiments, we take photographs that contain pixels ($1\ \mu m \times 1\ \mu m$). In my implementation, the crack gradient is so small that the film thickness varies by only $< 0.5\ nm$ within each pixel. So we treat data from each pixel as being from a set of parallel plates at a fixed distance.

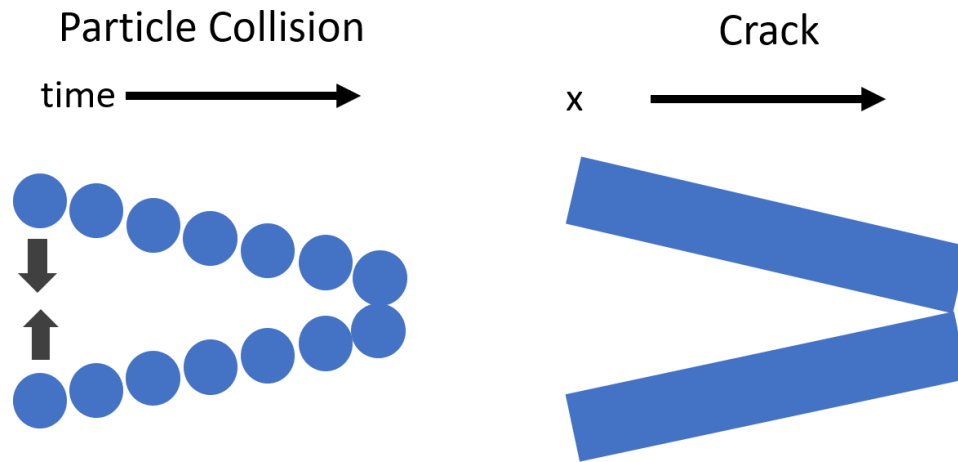


Fig 2: Correspondence between particle collision and crack. For the particle collision, the film thickness varies with time whereas for the crack, the film thickness varies with spatial location. In our apparatus, the crack geometry is invariant perpendicular to the page.

2.2 Realization of the CAA

2.2.1 Sample Preparation

As described above, we used a crack to enable measurements of adsorption at all separations simultaneously. The crack was prepared by bonding together two wafers using a commercial wafer bonder or by hand. The wafers can be silicon with a thin film of thermal oxide or glass bonded to a second glass wafer. For more detail on how this is achieved, see Appendix C.

2.2.2. Varying the Separation, D

At the perimeter of the bonded construct there is a defect where the wafers do not bond, leaving a crack as shown in Fig 3. As described above, In the photographs we take, from pixel to pixel, the gradient is tiny < 0.5 nm/ μ m providing us with nanometer resolution of the separation between two surfaces.

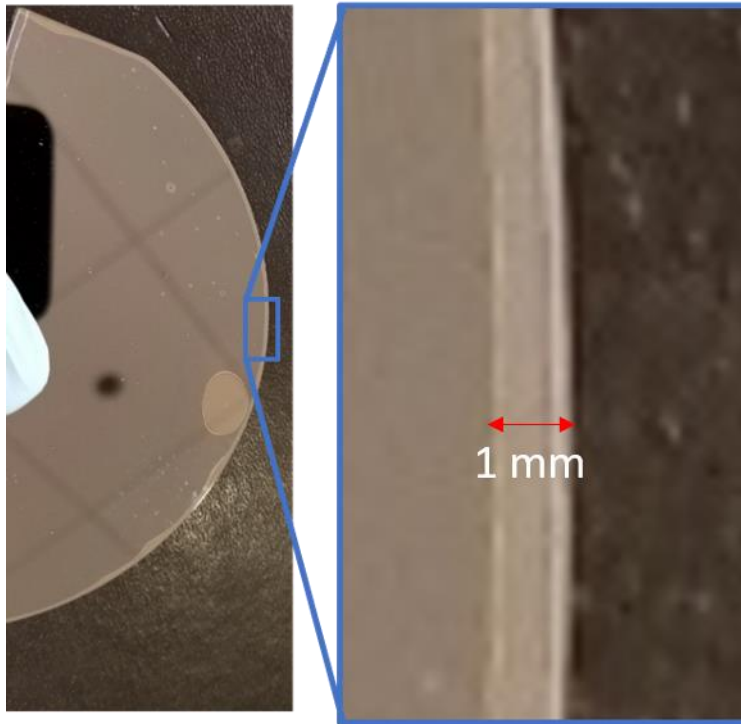


Fig 3: Photograph of a bonded construct formed by bonding a silica and silicon wafer. At the perimeter of the wafer is a thin crack.

2.2.3. Measurement of Separation

The separation between the two interfaces, D , can be measured using interference microscopy. In this technique, monochromatic light seen in reflection produces oscillating bright and dark bands of intensity as shown in Fig 4. The variation in interference is a result of the variation in the film thickness between the wafers. The thin film has air or water so that refractive index is different than the materials on either side of it. For a simple three-medium system with increasing refractive indices, $n_1 < n_2 < n_3$. The total measured intensity I_1 is given by

$$I_1(D) = \frac{1}{2}I_1 + \frac{1}{2}I_2 + I_1I_2 \cos \phi \quad (7)$$

where the interference term ϕ is

$$\phi = \frac{4\pi n_2 D}{\lambda} + \pi \quad (8)$$

where λ is the wavelength of light. As D increases monotonically orthogonal to the crack tip, the intensity $I(D)$ oscillates as a result of the interference term. In practice, the optical model is more complicated because of multiple reflections and additional interfaces. The calculation of the intensity for the experimental system can be found in Chapter 2 and Appendix A and the code used to solve this problem in Appendix D. From the intensity we determine the separation for every pixel in the image.

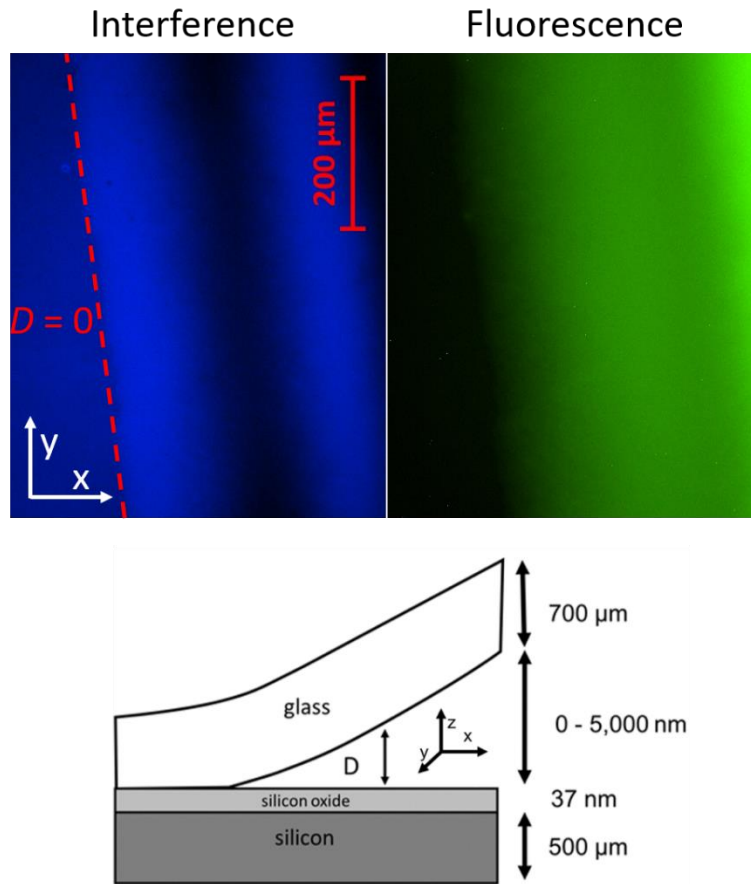


Fig 4: Example of images obtained from the CAA. Interference (used to measure the separation, D) and its corresponding fluorescence image (used to obtain the total number of molecules). The separation increases left of the crack tip, represented by the dotted red line. Below is a cross sectional view of the crack showing how the separation varies as a function of the x -position. All images were captured in black and white but have been colorized to represent the frequency of optical filter prior to the camera.

2.2.4. Measurement of Number of Molecules

The number of molecules per area can be determined for every separation, D , using fluorescence microscopy. Fluorescence is a property of many materials to re-emit a photon of a lower energy wavelength after absorption of light. The advantage of fluorescence is that one observes light against a very dark background, so there is very good signal to noise. This is a necessity in our measurements as we are observing as few as 100 molecules per pixel. In contrast, in absorption one measures loss of light in a bright background, which has much lower signal to noise. The fluorescence intensity is measured along with the interference in each pixel so that the amount and film thickness is measured in each pixel. In this way we can build up a plot of amount as a function of thickness. The thin film is almost constant in thickness in the y -direction, so we measure the adsorption at very many thicknesses.

The total number of molecules per area can be calculated from the measured pixel fluorescent intensity, I_T :

$$\left(\frac{n_i}{A}\right)_{\text{film}} = \frac{I_{M,\text{ave}}}{I_T} \quad (9)$$

where $I_{M,ave}$ is the intensity per molecule per unit area. Combining Eq 9 with Eq 5 and Eq 4, the surface excess of a fluorescent probe can be directly calculated as a function of separation.

Determination of $I_{M,Ave}$ in glass-silicon systems is provided in Chapter 2 and for glass-glass systems is discussed in Chapter 4 of this dissertation.

2.3. Experiments

The experiments considered in this dissertation focus on confined adsorption at equilibrium in systems where electrostatics is the dominant mechanism driving perturbations from bulk behavior in solutions. Specifically, these are measurements of fluorescein, a di-anion, in 1. dilute electrolyte (Chapter 2) and 2. concentrated electrolytes (Chapter 3), both at basic pH. Improvements made to the technique will be discussed in Chapter 4.

A list of potential experiments and experiments in progress by coworkers that can be performed using the technique as well are discussed (Chapter 5).

3. Theory

3.1. The double-layer at an Isolated interface

Frequently, in nature and industry one encounters charged interfaces in aqueous colloidal systems. A commonly encountered example is the silica interface in contact with water. The surface silanol group dissociates leaving a negative charge on the solid and protons in solution.

In electrolytes, this charged interface attracts counter-ions to the surface and repels co-ions. Due to the inherent thermal motion of the ions however, the counter-ions do not become bound to the surface neutralizing the charged interface but are rather smeared out, with their concentration much higher than bulk immediately adjacent to the interface and monotonically decreasing as a function of distance away from the interface. This is known as the Gouy-Chapman model of the double layer and has the following key assumptions.

1. The ions behave as point objects.
2. The ions respond only to the mean electric field.
3. Often there is no specific adsorption of ions. All ions are treated as essentially the same.
4. The dielectric constant of the medium, ϵ , is constant in the double layer
5. The surface charge is uniformly distributed over the surface

3.2. The Poisson-Boltzmann equation

For a collection of ions in space with a uniform dielectric constant, the distribution of ions can be described by Poisson's equation,

$$\nabla\psi = -\frac{n(x, y, z)}{\epsilon\epsilon_0}. \quad (10)$$

Where $n(x, y, z)$ is the space charge density of ions, ε is the dielectric constant of the medium and ε_0 is the permittivity of free space.

For a planar one-dimensional system, the equation simplifies to

$$\frac{d^2\psi}{dz^2} = -\frac{1}{\varepsilon\varepsilon_0} \sum_i Z_i e n_i(z). \quad (11)$$

The number density of ions of species i at a position x is related to the local electrostatic potential via the Boltzmann distribution,

$$n_i(z) = n_i(\infty) \exp\left(-\frac{\phi}{kT}\right), \quad (12)$$

where k is the Boltzmann constant, T is the temperature and $n_i(\infty)$ is the bulk ion number density and ϕ is the potential of the ion relative to the value at $z = \infty$. If we assume that electrostatic forces are the only contribution to the potential energy, then:

$$n_i(z) = n_i(\infty) \exp\left(-\frac{Z_i e \psi(z)}{kT}\right), \quad (13)$$

where ψ is the local electrostatic potential, Z_i is the valence on species i and e is local electrostatic potential.

Eq 8 and 9 above can be combined to create the Poisson-Boltzmann equation:

$$\frac{d^2\psi}{dz^2} = -\frac{1}{\varepsilon\varepsilon_0} \sum_i Z_i e n_i(\infty) \exp\left(-\frac{Z_i e \psi(z)}{kT}\right). \quad (14)$$

For a symmetric electrolyte the Poisson-Boltzmann equation can be written as,

$$\frac{d^2\psi}{dz^2} = \frac{Z_i e n_i(\infty)}{\varepsilon\varepsilon_0} \left(\exp\left(\frac{Z e \psi(z)}{kT}\right) - \exp\left(\frac{-Z e \psi(z)}{kT}\right) \right). \quad (15)$$

Applying the boundary condition that the potential at the interface is a constant of a certain value, ψ_0 and the potential ψ_∞ is 0 at infinity, when the potential is low i.e $|Z\psi_0| < \frac{kT}{e} \sim 25$ mV, the exponentials in Eq 11 can be linearized to give:

$$\frac{d^2\psi}{dz^2} = \frac{2Z_i^2 e^2 n_i(\infty)}{\varepsilon\varepsilon_0 kT} \psi(z) \equiv \kappa_D^2 \psi(z). \quad (16)$$

For a single interface, the linearized equation can be solved exactly:

$$\psi(z) = \psi_0 \exp\left(-\frac{z}{\kappa_D^{-1}}\right). \quad (17)$$

The ion density profile away from the interface can then be determined by substituting Eq 13 into Eq 9 where

$$n_i(z) = n_i(\infty) \exp\left(\frac{Z_i e \psi_0 \exp\left(-\frac{z}{\kappa_D^{-1}}\right)}{kT}\right). \quad (18)$$

3.3. The Debye-length

In the solution to the linearized equation, I introduced the Debye length, κ_D^{-1} ,

$$\kappa_D^{-1} \equiv \sqrt{\frac{\epsilon \epsilon_0 kT}{2e^2 Z_i^2 n_i(\infty)}} = \sqrt{\frac{\epsilon \epsilon_0 RT}{2000e^2 N_{AV}^2 c_i(\infty)}}, \quad (19)$$

where $c_i(\infty)$ is the concentration of ions in mol/L, N_{AV} is Avogadro's constant, R is the gas constant.

For a symmetric electrolyte at low potential, the potential decays to roughly 5% of ψ_0 by 3 Debye lengths from the interface.

The non-linear Poisson-Boltzmann equation can also be solved exactly for any surface potential numerically. Fig. 5 compares the exact numerical and the low potential approximation for a constant surface potential boundary condition of 150 mV. Clearly the low potential approximation is poor for this condition.

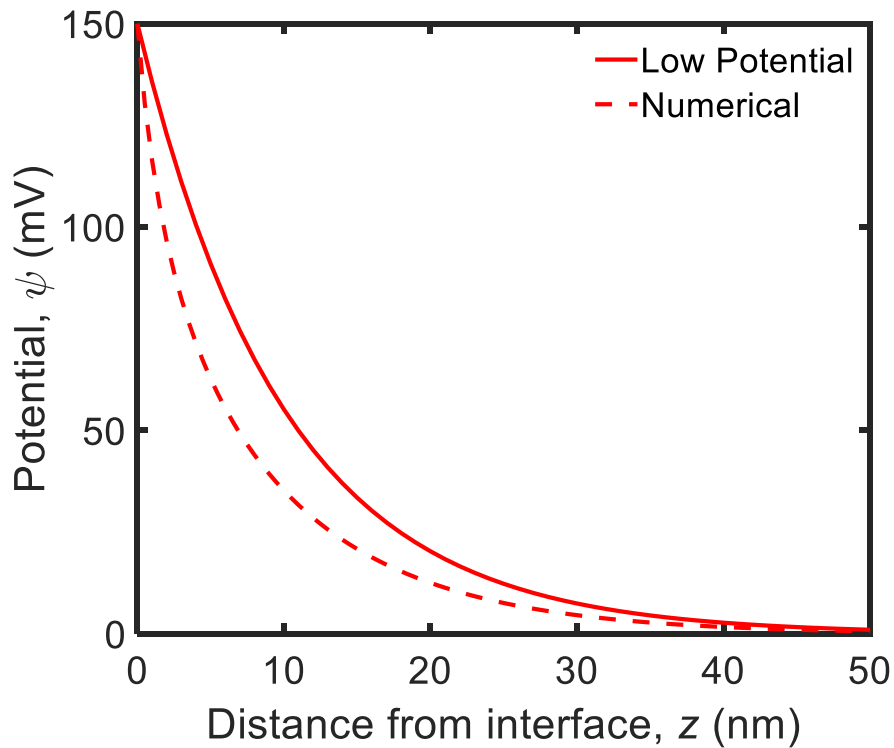


Fig 5: Comparison between low-potential and numerical solution of potential as a function of distance from the Poisson-Boltzmann equation for an interface with a surface potential of 150 mV and a Debye-length of 10 nm.

A key feature is readily apparent from the Debye-length. As the ionic strength of the solution increases, the Debye length drops rapidly i.e. greater screening occurs of the surface potential by the background electrolyte. This has consequences for the concentration profile as well which decays as an exponential of an exponential away from the interface. Increasing concentration of ions in the bulk means decreasing positive adsorption of counter-ions in the diffuse double-layer to the interface and increasing negative adsorption of co-ions. The normalized concentration profiles for a symmetrical monovalent electrolyte to the interface is illustrated in Fig 6.

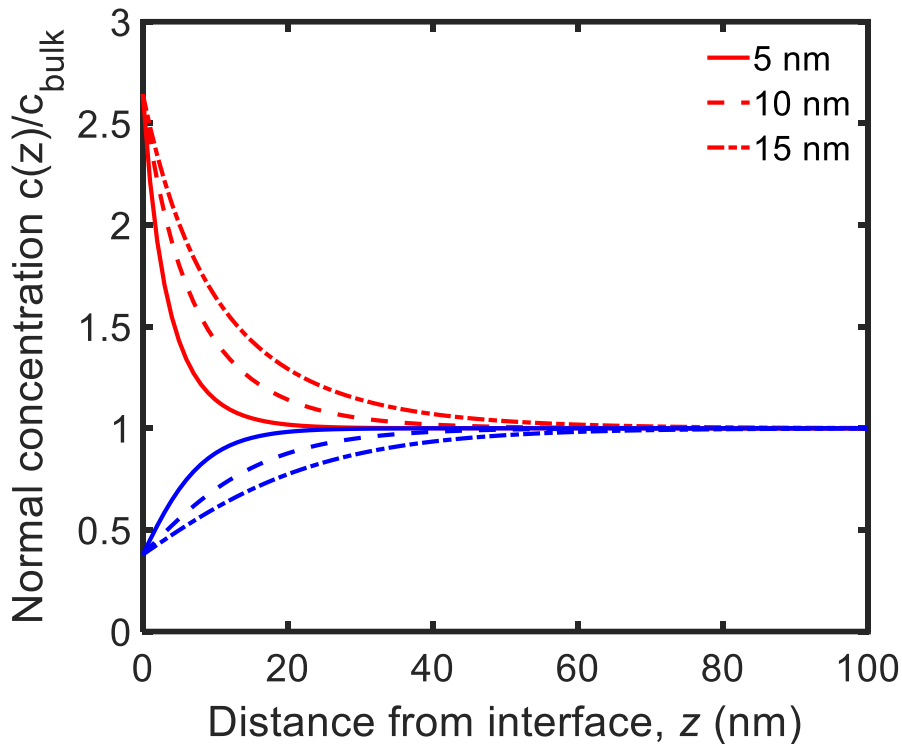


Fig 6: Concentration profiles of a monovalent electrolyte for three Debye-lengths. Red represents the counter-ion and blue the co-ion. The surface potential used for these calculations here is $\psi_0 = 25$ mV. As the Debye-length is increased the distance from the interface there still exists a perturbation from the bulk concentration also increases

The main point of the Debye-length is this, increasing the bulk concentration of ions decreases the screening length of the potential which results in less positive adsorption of counter-ions and negative adsorption of co-ions away from the surface. This statement assumes that the surface potential is independent of the concentration which is not always the case and will be discussed in the next section.

3.4. Surface Charging at an Interface

As the diffuse double layer is electrically neutral, the surface charge density of the solid is equal to diffuse double layer ion density. This can be expressed in terms of the potential profile from Poisson's equation,

$$\bar{\sigma}_0 = - \int_0^{\infty} \epsilon \epsilon_0 \frac{d^2 \psi}{dz^2} dz = - \epsilon \epsilon_0 \left. \frac{d\psi}{dz} \right|_{z=0}. \quad (20)$$

The surface charge density however can depend on the degree of charging of the interface which in turn depends on the bulk ion concentration. For example, consider an interface that ionizes in an aqueous solution to form negatively charged sulfate sites on the surface:



The concentration of H_s^+ ions at the surface is then given by the Boltzmann equation,

$$[\text{H}_s^+] = [\text{H}^+] \exp\left(-\frac{e\psi_0}{kT}\right), \quad (22)$$

where I have assumed that the only contribution to the potential is electrostatic.

Substituting the above expression in the expression for the equilibrium constant, K_{eq} for the surface sulfate sites gives

$$K_{\text{eq}} = \frac{[-\text{SO}_4^-]}{[-\text{SO}_4\text{H}]} [\text{H}^+] \exp\left(-\frac{e\psi_0}{kT}\right). \quad (23)$$

For an interface, the total number of sites is fixed by nature, thus the total site density, N_s is

$$N_s = [-\text{SO}_4^-] + [-\text{SO}_4\text{H}] \quad (24)$$

The surface charge density for an interface

$$\bar{\sigma}_0 = -e[-\text{SO}_4^-] \quad (25)$$

Substituting from Eq 24 and Eq 23 one obtains the boundary condition at the interface

$$\bar{\sigma}_0 = -\epsilon \epsilon_0 \left. \frac{d\psi}{dz} \right|_{z=0} = -\frac{eN_s}{1 + \frac{[\text{H}^+]}{K_{\text{eq}}} \exp\left(-\frac{e\psi_0}{kT}\right)} \quad (26)$$

As low pH when there are a large number of hydrogen ions in solution, the majority of surface sites remain associated, resulting in $\bar{\sigma}_0 \rightarrow 0$. However at high pH $\bar{\sigma}_0 \rightarrow -eN_s$. Effectively this means that the surface potential is high at high pH and low at low pH for an anionic surface site. An ion that adsorbs to the surface to change the surface charge and potential directly (e.g. the proton in Eq. 21) is known as a potential determining ion.

In summary, the effect of addition potential determining ions into solution is twofold 1. The dissociation equilibrium is shifted, e.g. more proton binding to sulfate groups, which directly affects the surface charge and indirectly affects the potential, and 2. The Debye length is shorter as more ions are added into solution.

3.5. The Double-layer in a Thin Film between Two Interfaces

For a thin film, we will continue to use the Poisson-Boltzmann equation and again consider the one-dimensional planar system, but now the boundary conditions change. Instead of zero potential at infinite distance from the surface, there is now a boundary condition at the other interface, at a variable distance, D , from the first interface. Here we will consider only symmetric systems, such that (a) the same boundary condition occurs at both solid–liquid interfaces, and (b) at the midplane, the gradient in potential is zero.

The results provided in the subsequent sections use the same underlying assumptions as the solutions for the single-interface case, namely

1. The ions behave as point objects.
2. The ions respond only to the mean electric field.
3. Often there is no specific adsorption of ions. All ions are treated as essentially the same.
4. The dielectric constant of the medium, ϵ , is constant in the double layer
5. The surface charge is uniformly distributed over the surface

3.5.1. Symmetric constant surface-potential boundary condition

For the boundary condition that surface potential is constant and the same at either interface for confined system with geometry as shown in Fig 3, and a Z:Z electrolyte, at low potentials Eq 11 results in a potential that is a hyperbolic function of the surface potential,

$$\psi(z) = \frac{\psi_0 \cosh(-\kappa_D z)}{\cosh\left(-\frac{\kappa_D D}{2}\right)} \quad (27)$$

Note that the numerator is a constant for fixed film thickness, such that the potential is the sum of two exponentials, each of which decays with the Debye-length. We still refer to the Debye-length as the decay length, even though strictly it is the scaling parameter rather than a decay length, because the functional form is not a simple exponential.

If the only force is electrostatic, once the electrical potential is known, the concentration profile can be determined from the Boltzmann distribution (Eq. 13) and the surface excess can be calculated using Eq 4 and 5. In Chapter 2 I always calculated the potential using the exact numerical solution, and in Chapter 3 I always calculated the potential using the low-potential approximation. In all chapters referenced above, I ignored any non-electrostatic contributions to the total potential.

An example of a calculation of surface excess driven by electrostatics for a monovalent ion is shown in Fig. 7. For a counterions there is a positive surface excess that reaches a plateau value at about 3 Debye-lengths and for co-ions, there is a negative surface excess that reaches a plateau value at about 4–5 Debye-lengths.

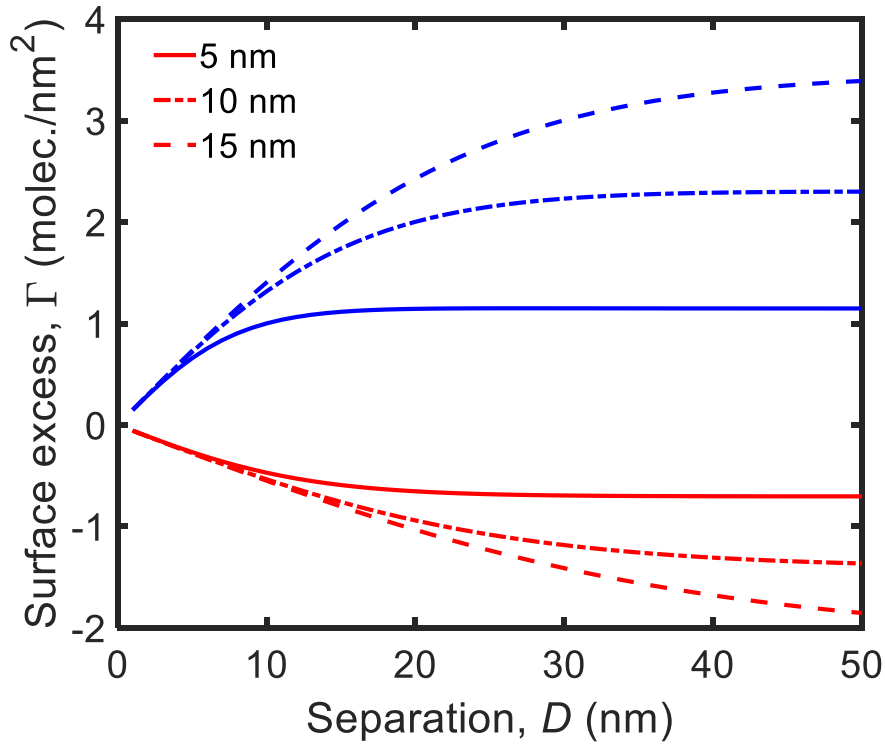


Fig 7: Surface excess as a function separation calculated for a monovalent tracer ion interacting with charged interfaces in background electrolytes of varying Debye-lengths and a boundary condition of a constant symmetrical surface potential of -25 mV using the low-potential approximation. The blue lines represent positive ions or counter-ions and the red lines represent negative ions or co-ions. Co-ions are negatively adsorbed with adsorption decreasing as a function of separation for all Debye-lengths.

3.5.2. Constant-Charge Boundary Condition

Another common boundary condition that can be applied is the constant charge boundary condition. This occurs when the dissociation constant for the surface is so low that there is no change in binding to each surface when the separation between interfaces decreases. In this case, the surface potential will change. Integrating the Poisson Eq. from the midplane to the solid-liquid interface, and equating the surface charge to the sum of all the dissolved charge in the same range (electroneutrality):

$$\left. \frac{d\psi}{dz} \right|_{z=D/2} = \frac{\sigma_0}{\epsilon\epsilon_0} \quad (28)$$

where σ_0 is the surface charge density in the thin film. Thus we see that the constant surface charge boundary condition is the same as a constant surface gradient in potential.

Solving the Poisson-Boltzmann Eq. for assumptions listed above and symmetrical surface charge densities with the low potential approximation, in a one-dimensional system the potential is given by:

$$\psi(z) = \frac{\sigma_0 \cosh(-\kappa_D z)}{\epsilon\epsilon_0 \kappa_D \sinh\left(-\frac{\kappa_D D}{2}\right)} \quad (29)$$

As the separation decreases, to maintain constant surface charge, the surface potential must rise. Therefore the low potential approximation is only valid for $2\kappa_D^{-1}$. For small separations, the exact numerical solution should be used for constant potential.

At large separations, the constant charge boundary condition is equivalent to the constant potential boundary condition and the potential is related to the charge density as

$$\sigma_0 = \varepsilon\varepsilon_0\psi_0\kappa_D \quad (30)$$

Fig 8 shows an example of a calculation of surface excess for the low potential approximation for the constant potential and constant charge boundary conditions. The surface excess for co-ions looks similar to the surface potential case, however for counter-ions results in surface excess in thin films that are significantly larger than that of thick films. The steep rise in counter-ion concentration in thin films is due to the rise in potential to maintain a constant surface charge. This results in a large positive adsorption of counter-ions in thin films and large negative-adsorption of co-ions.

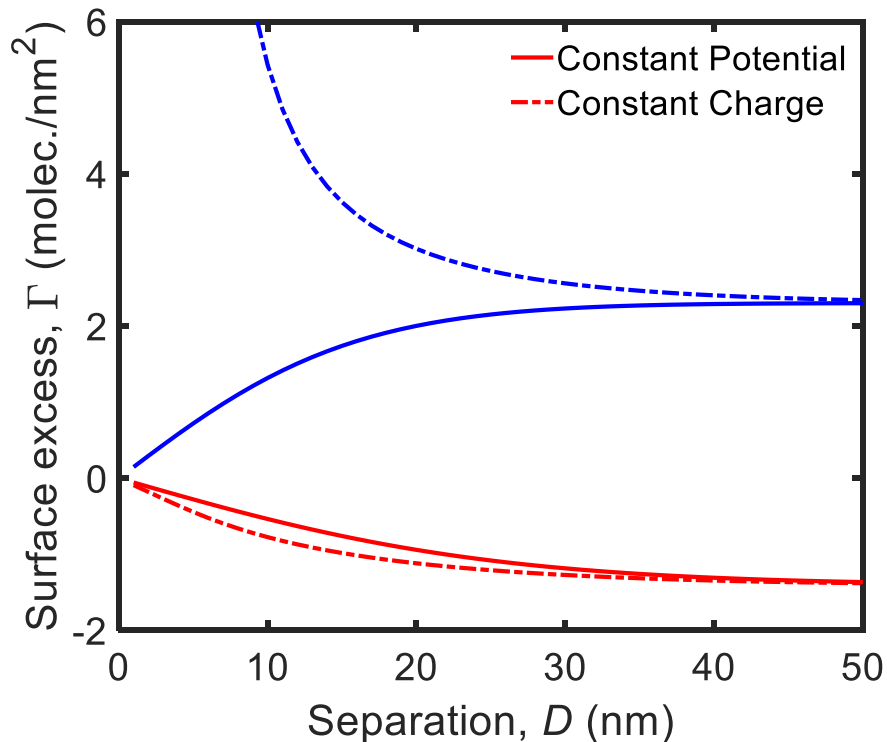


Fig 8: Surface excess as a function of separation calculated for a monovalent tracer ion interacting with charged interfaces in background electrolytes of 10 nm Debye length and with a surface charge density, $\bar{\sigma}_0 = 1.59 \times 10^{-3} \frac{\text{C}}{\text{m}^2}$, $\psi_0 = 25$ mV for the different boundary conditions. The blue lines represent counter-ions and the red lines represent co-ions. Co-ions are negatively adsorbed with adsorption decreasing as a function of separation for all Debye-lengths. Calculations used the low potential approximation.

4. Literature Review

4.1. Measurement of Adsorption to a Single Interface

A large number of techniques exist to measure adsorption to a single interface and a few of these are discussed here.

X-Ray Photoelectron spectroscopy (XPS) is one technique that can be used to measure the surface properties in vacuum via the photoelectric effect. Absorption of X-Rays causes electrons in the top few nm of the sample to be emitted. The binding energy is known from the energy of the emitted electron, and is a characteristic of the element and the binding. This technique does not measure the surface excess, but can be used to determine the composition of the first few nm of the solid. This technique has been used to measure the adsorption of proteins,¹⁸⁻²⁰ adsorption of alcohols^{21, 22} and gases²³ to various surfaces to name a few.

Another common technique used to measure adsorption to a single interface Surface Plasmon Resonance (SPR).²⁴ In this technique, a beam of polarized light (typically a laser) is used to excite a thin metal film at the interface between media with different refractive indices. Free electrons at the surface of the material oscillate and their collective oscillations are referred to as plasmons. At certain angles, there exists a resonance between the angle of the incident light and the plasmons at the interface resulting in light absorption at that specific angle. As materials adsorb the interface the angle at which absorption of light occurs changes and this can be used to detect adsorption events at that interface. This technique can be used to determine the surface excess,²⁵ adsorption of proteins to functionalized metals²⁶⁻²⁸ and for gas-sensing applications.^{29, 30}

Fluorescence microscopy is a relatively simple technique used to measure adsorption. If a fluorescent probe is adsorbed to an interface, it fluoresces, and if it does not, no fluorescent signal is observed. Protein adsorption,³¹⁻³³ surfactant adsorption³⁴ and even bacterial adsorption to interfaces³⁵ can be quantified and measured using fluorescence microscopy.

While three techniques that perform direct measurements of adsorption have been discussed here with some detail, many others exist as well such as quartz crystal microbalances (QCM),³⁶ total internal reflection microscopy (TIRF),³⁷ Infrared Spectroscopy,³⁸ X-Ray Standing Waves,³⁹ solution depletion studies,⁴⁰ optical reflectometry,⁴¹ ellipsometry,⁴² calorimetry,⁴³ neutron reflectometry⁴⁴ and many others.

4.2. Measurement of the Ion Profile using Standing X-Ray Waves

Few direct measurements of electrical double layer in solution exist in the literature. This is primarily due to the difficulty in the measurement of ion concentrations which decay relatively rapidly (on the order of nanometers) in solution.

Bedzyk et al. were the first to measure the ion profile by exploiting the fluorescence of metal atoms when excited by X-Rays.³⁹ In this technique, a charged functionalized silica interface as shown in Fig 9 in contact with a solution of ZnCl₂ is illuminated with X-Rays at variable angles. The total detected intensity of fluorescence emitted by the Zn²⁺ ions as a function of illumination angle is,

$$Y(\theta) = \int_0^{\infty} N(z)I(\theta, z)dz \quad (31)$$

Where $Y(\theta)$ is the total detected intensity, $N(z)$ is the number density of ions and $I(\theta, z)$ is the intensity per molecule for a Zn^{2+} ion at a certain illumination angle and position in the diffuse double layer.

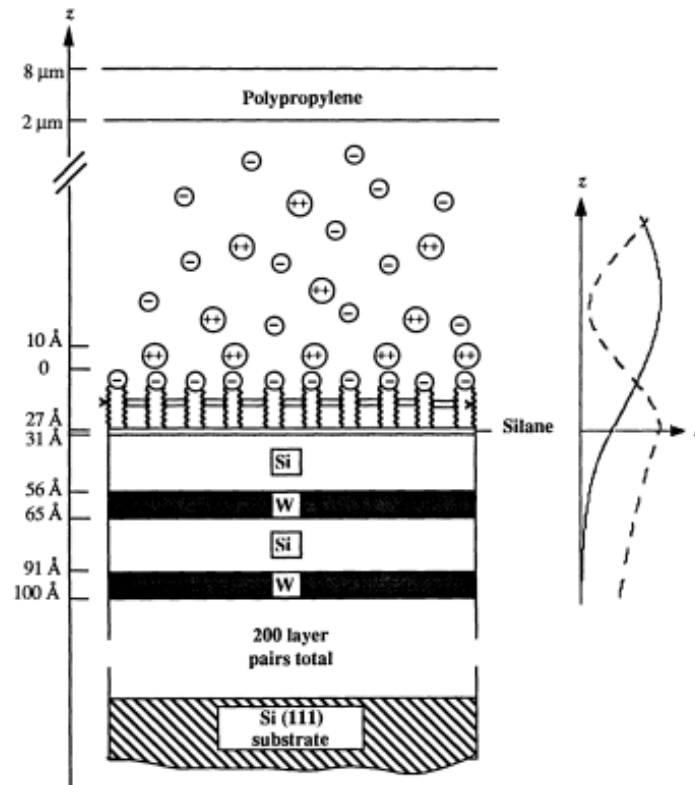


Fig 9: Schematic of experimental system probed in X-Ray Standing Wave technique. From Ref 39. Reprinted with permission from AAAS

They fit the intensity data to the Gouy-Chapman-Stern and Helmholtz distribution for $N(z)$ and as shown in Fig 10. The Helmholtz model for $N(z)$ which posits that there is a layer of irreversibly adsorbed set of ions that effectively neutralizes the surface does not describe the experimental data. The Guoy-Chapman-Stern model for a partially irreversibly adsorbed set of ions and a subsequent diffuse double layer above the surface offers a more accurate picture of ion behavior next to charged interfaces.

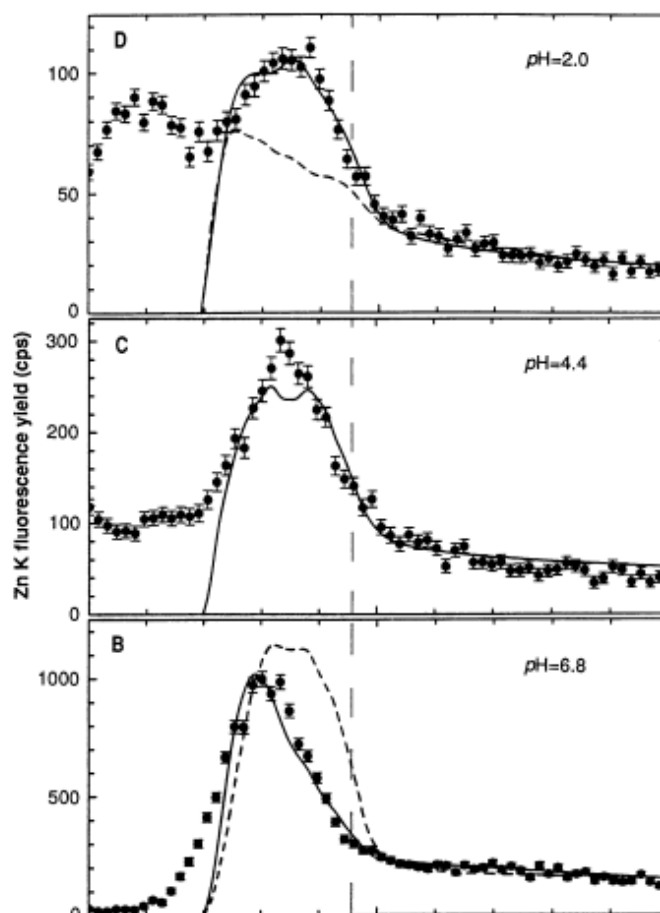


Fig 10: Experimental data for the fluorescence intensity, represented by the filled dots and theoretical intensity represented by the solid and dashed lines using Eq 21. The solid line represents an ion profile from Poisson-Boltzmann and the dashed line is the Helmholtz model for the electrical double layer where counter-ions adsorb onto the surface neutralizing surface charge and there is no diffuse double layer. From Ref 39.
 Reprinted with permission from AAAS

Wang et al. used the standing-wave technique to show that the ion adsorption profile can be reversibly changed by altering the pH of the solution for a 0.1 mM solution of $ZnCl_2$ in contact with a charged phospholipid monolayer. Lowering the pH from 5.8 to 2 effectively discharges the interface lower the pH to below the pK_a of interfacial groups.⁴⁵ This results in a change in the measured fluorescence signal which is easily reversed when titrated back up to pH 5.8. Table 1 gives the measured surface excess values of Zn^{2+} ions in the diffuse double layer. As the pH is lowered the surface excess of ions decreases as the interface becomes discharged and no longer attracts ions to the surface and as the interface is charged again, the surface excess of ions increases.

Table 1: Surface density of ions as a function of pH. Reprinted (adapted) with permission from Ref 45. Copyright 2001 American Chemical Society

pH	zinc surface density (10^{12} ions/cm 2)	
	equivalent in diffuse double layer ^a	surface bound ^b
5.8(-)	14.7	2.2
4.2(-)	4.01	0.67
2.0(-)	1.71	0.34
4.2(+)	3.78	0.59
5.8(+)	13.2	2.1

4.3. Force Measurements in Electrolytes

Ducker et al.¹¹ and Israelchvili et al.¹² measured the energy of interaction between two interacting like-charged interfaces using the colloid probe technique for silica interfaces and the surfaces forces apparatus for mica interfaces respectively. As shown in Fig 11, at large separations (10 – 100 nm), they showed that the experimental interaction energy per unit area agreed with predictions from Poisson-Boltzmann,

$$\frac{\text{energy}}{\text{area}} = E_a = \frac{F}{2\pi R} = \frac{64nkT}{\kappa_D} \tanh^2\left(\frac{e\psi_0}{4kT}\right) \exp(-\kappa_D D) \quad (32)$$

where F is the force and R is the radius of curvature of the interface.

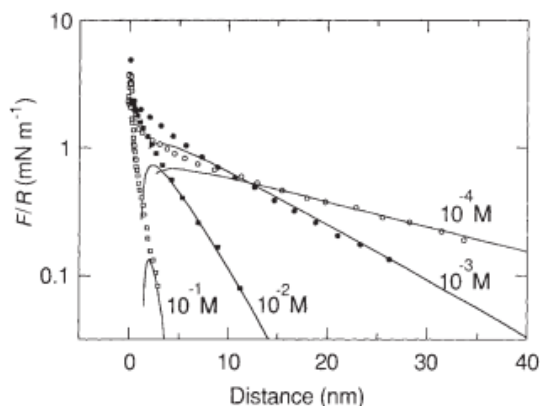


Fig 11: The interaction energy between two interacting crossed mica cylinders in the surface forces apparatus measured for salt concentrations from 10^{-1} to 10^{-4} . The solid lines represent fits of forces calculated from DLVO theory where surface potential and decay lengths are the only fitting parameters. Reprinted by permission from Springer Nature: Nature, Ref 11, 1991.

The experimental decay length of the forces was shown to closely match the theoretical Debye length κ_D^{-1} .

While the surface excess is not directly measured in these experiments, the good fits between Poisson-Boltzmann theory and experimental data indicate that it can be readily calculated for electrolytes from Eq. 22. The primary weakness of this work with regards to measurement or calculation of surface excess is that it is a model-dependent, indirect measurement of adsorption. It relies on the validity of the Poisson-Boltzmann model, which can fail in more complicated systems such as concentrated electrolytes or in systems with surfactants where hydrophobic interactions between the surfactant molecules also becomes relevant.

4.4 Proximal Adsorption from Force Measurements in Aqueous Surfactant Solutions

Ash et al.⁴⁶ and Hall⁴⁷ developed a thermodynamic approach for the measurement of the surface excess of adsorption as a function of separation between two interfaces. The experimental measurement is essentially the same i.e. the measurement of forces between two interacting interfaces, however the approach to the analysis of data is different. The conventional analysis of force measurements using DLVO theory dictates that the force between two interfaces is the sum of multiple forces (see Eq 3) and by adding additional force terms using a model that one thinks describes the data well, one can extract out the surface excess of adsorption. The weakness is the reliance on the model, as a complicated system requires a complicated model which may or may not be correct. The advantage of the thermodynamic approach is that it is model-independent. From the thermodynamic approach, the change in surface excess as a function of separation is related to the energy of interaction as

$$\Gamma_i(s) - \Gamma_i(\infty) = -\frac{1}{2} \left(\frac{\partial E_a}{\partial \mu_i} \right)_{T,p,\mu_j,s} \quad (33)$$

where $\Gamma_i(s)$ is the surface excess of component i .

The changes in adsorption that occur when two interfaces are brought close together is termed as “proximal adsorption” and has been studied in the Ducker group. Subramanian et al.⁴⁸ and Lokar et al.⁴⁹⁻⁵¹ made use of this thermodynamic argument to calculate the proximal adsorption of surfactants for a range of separations and solution conditions.

Subramanian from our group performed the first experimental study using this approach to analyzing surface forces to look at the effect of concentration of a cationic surfactant, dodecyltrimethylammonium bromide (C₁₂TABr) and separation on its proximal adsorption in thin confined films. The critical micellar concentration (cmc), where surfactant molecules begin to form micelles instead of existing exclusively as monomers in solution is 14.2 mmol/kg in water. Fig 12 shows the energy of interaction between two silica surfaces for a range of surfactant concentrations far below the cmc.

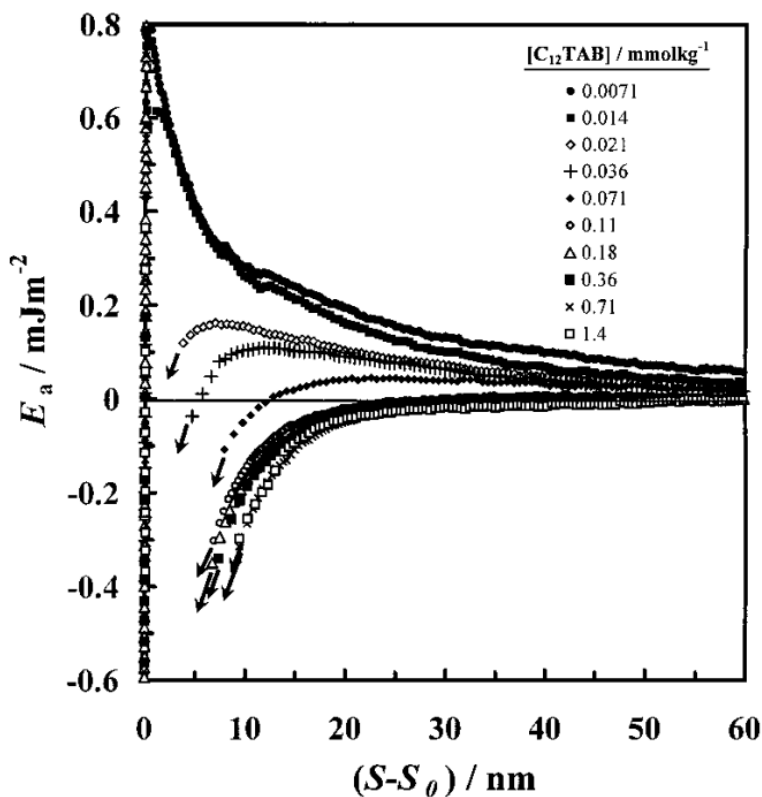


Fig 12: Interaction energy as a function of separation for surfactant concentrations from $\text{cmc}/2000$ to $\text{cmc}/10$. Here distance is given as $(S - S_0)$ where S is the separation between the bare silica surfaces and S_0 is the separation where the authors judged that the aqueous film thickness went to zero. Reprinted (adapted) with permission from Ref 46. Copyright 2001 American Chemical Society

One disadvantage of the use of Eq. 33 is that one must also measure or calculate the chemical potential at each concentration. For any substance other than a simple ion, it is non-trivial to calculate the chemical potential, so it must be measured. The gradient in interaction energy as a function of the activity coefficient is shown in Fig 13 for a few separations.

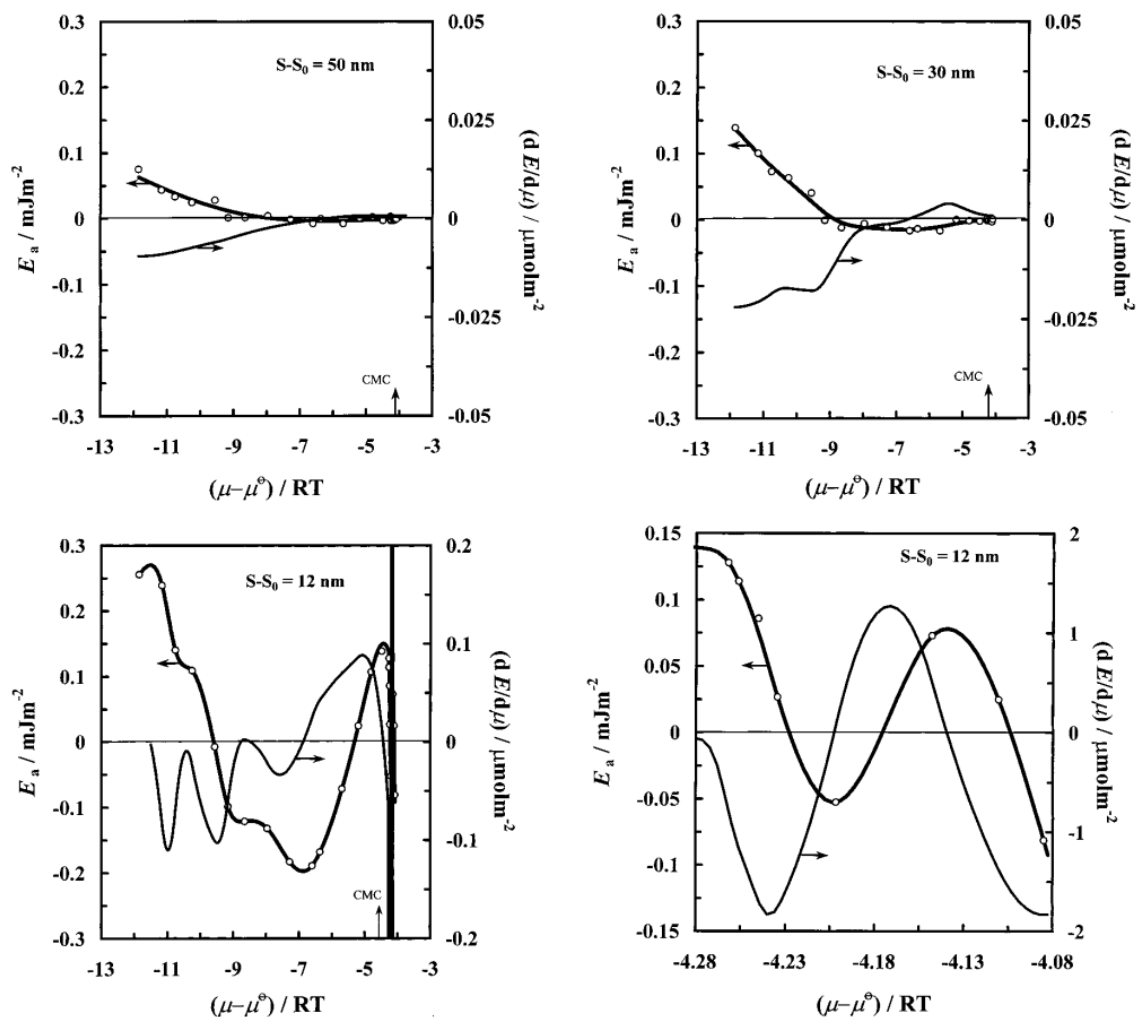


Fig 13: Interaction energy and the gradient in interaction energy as a function of chemical potentials for a range of separations. At large and intermediate separations, below the cmc the gradient is roughly monotonic.

The oscillations at small separations are due to the noise in the data in the lower left figure but are real in lower right figure where measurements are done significantly above the cmc.

Reprinted (adapted) with permission from Ref 46. Copyright 2001 American Chemical Society.

Once the relationship between interaction energy and chemical potential is known, the proximal adsorption can be calculated using Eq 23. Fig 12 shows that for a dilute suspension of surfactant molecules the change in surface excess decays exponentially with separation and is positive at small separations i.e. as the surfaces comes close together, net adsorption of positive ions occurs.

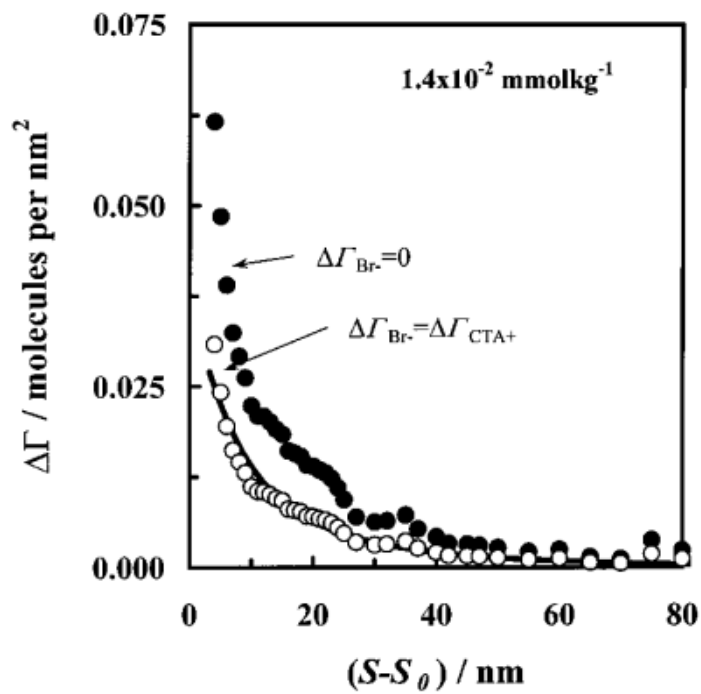


Fig 14: Proximal adsorption as a function of separation for CTAB. The filled circles are changes in surface excess assuming that $\Delta\Gamma_{\text{Br}^-} = 0$ and the open circles are if $\Delta\Gamma_{\text{Br}^-} = \Delta\Gamma_{\text{CTA}^+}$. The positive values at small separation indicates net adsorption i.e. there are more molecules per nm^2 than at infinite separation. Figure reproduced from Ref 46. with permission from ACS.

They also find that for concentrations between $\text{cmc}/130$ and $\text{cmc}/10$, adsorption is independent of separation i.e. $\Delta\Gamma_{\text{CTA}} \sim 0$ for $(S - S_0) > 7$ nm. At higher surfactant concentrations, from $\text{cmc}/10$ to the cmc , the surfactant desorbs and $\Delta\Gamma_{\text{CTA}}$ is negative as the surfaces approach each other. When the concentration is > 4 cmc , the surface excess initially increases at intermediate separations due to the depletion force and then decreasing once surfactant is squeezed out from the film. At concentrations > 8 cmc , the surface excess becomes an oscillatory function of the separation as structural rearrangement of the surface micellar layers occurs.

Lokar extended these studies and studied the effect of chain length, pH and the ionic strength on the surface excess of surfactants as a function of separation.⁴⁹ He showed that the decay length of the surface excess profile correlated with the Debye-length of the solution and that short-chain hydrocarbon surfactants displayed significantly reduced surface excess compared to long-chain hydrocarbons. He also examined more complex systems looking at mixtures of cationic and zwitterionic surfactants and showed that zwitterionic surfactants (specifically N-dodecyl-N,N-dimethyl-3ammonio-1propanesulfonate or DDAPS) adsorbs minimally to the interface up to $2/3$ cmc .⁵¹ The presence of a small amount a cationic surfactant (dodecylpyridinium chloride or DPS) results in a change in the surface excess of DDAPS increasing with decreasing separation. The adsorption of the cationic surfactant is less sensitive to the inclusion of the zwitterionic surfactant. The inclusion of both results in a large net surface excess of surfactant as a function of concentration with decreasing separation due to the coupling of the hydrophobic tails of the surfactants.

The most important conclusion from the thermodynamic approach is that there are large changes in adsorption in confined films. It is important to consider these changes and therefore worthwhile to develop a technique for measuring them directly.

Chapter 2: Effect of background electrolyte concentration on surface excess of the fluorescein dianion in dilute electrolytes

This chapter reproduces original work published in *Langmuir* on August 5, 2018 in Volume 34, pages 10469 – 10479. In this chapter I outline the development of the technique to measure adsorption in confinement and study the effect of background electrolyte concentration (NaCl) on the equilibrium adsorption behavior of fluorescein, a dianion, next to negatively charged interfaces under basic conditions in dilute systems (0 – 0.4 M).

Robert Grayson developed and wrote the code for the optical modeling detailed in this section and Dr. William Ducker provided guidance on experiments and contributed to the writing of the paper.

The following article is reprinted (adapted) with permission from Gaddam, P.; Grayson, R.; Ducker, W., A., Adsorption at Confined Interfaces. *Langmuir* **2018**, 34 (36), 10469-10479. Copyright 2018 American Chemical Society.

Adsorption at Confined Interfaces

Prudhvidhar Gaddam[†], Robert Grayson[†], and William Ducker^{*}

Department of Chemical Engineering and Center for Soft Matter and Biological Physics, Virginia Tech, Blacksburg, VA 24061, USA.

[†]These authors contributed equally

^{*}For correspondence: wducker@vt.edu

ABSTRACT

We describe measurements of adsorption between two flat plates when the plates are separated by 0 – 65 nm. The objective is to examine how adsorption is affected by confinement in very thin films. The specific measurement is of the depletion of a divalent anion, fluorescein, in aqueous solution between two anionic solids, but the measurement could apply to a range of fluorescent dye molecules. At large separations between the flat plates, the dye is depleted relative to the bulk concentration. At smaller separations, the depletion of the dye decreases. The range of the depletion and the magnitude of depletion decrease with shorter Debye-length. Both of these effects are consistent with a simple calculation using the Poisson-Boltzmann equation. The measurement of all separations is achieved simultaneously by measuring visible-light interference in a wedge-shaped crack created between an oxidized-silicon wafer and a glass wafer. The amount of dye is measured from the fluorescence emission, after accounting for the optical interference. There is a multitude of applications where surfactants, polymers, ions, etc. are adsorbed to effect changes in thin films. One example is adsorption designed to alter the stability of colloidal particles. It is well known that adsorption of simple ions can change with the thickness of a thin film (charge regulation); here we describe a direct method to measure adsorption of as a function of confinement, and results for one example.

INTRODUCTION

Much of the practical interest in adsorption arises when molecules adsorb in confined places such as in the gaps between particles or other thin films. Adsorption to a *single* interface has been very widely studied (e.g.^{41, 52, 53}) but adsorption in confined spaces has been the subject of less attention. Adsorption in the confined film may be different to adsorption in the isolated film because of fields or concentration profiles altered by the “second” interface and because of geometric confinement. The purpose of this work is to describe a method for the direct measurement of adsorption in a confined film as a function of thickness (See Fig. 1a) and to report a detailed measurement for one particular example: adsorption of fluorescein in aqueous solution between two silica-like materials.

Surfactants, polymers and particles are often adsorbed to particles or droplets in order to stabilize the suspension.⁵⁴ The key event in stabilization is the collision between particles, so it is interesting to know how adsorption changes during the collision, i.e. as a function of the separation between the particles. In some cases, the adsorption energy may be so strong compared to the effects of the interface that very little change in adsorption occurs during the collision. This might occur for a silane covalently bonded to silica. At the opposite end of the spectrum, the adsorbate may be held by weaker forces such that the intrusion of a second surface may cause significant change in adsorption. This could occur for surfactant layers held by the hydrophobic effect or van der Waals forces.

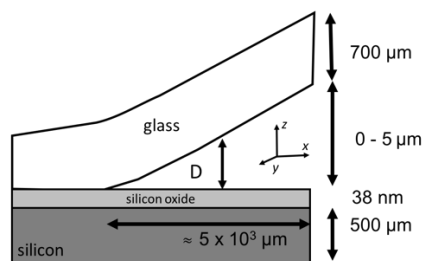
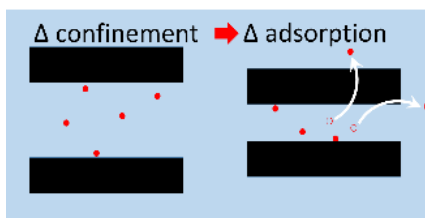


Fig. 1 Schematics showing (a) proximal adsorption, and (b) the experimental sample. Films of different thickness, D , are created between the glass and silicon oxide. The sample is similar to a crack, and we refer to portion where $D \rightarrow 0$ as the crack tip.

The situation where adsorbed species are in equilibrium with bulk during changes in separation has been described in detail by Hall⁴⁷ and by Ash et al.⁴⁶ Their treatment shows that when a surface force is altered by changes in chemical potential of an adsorbate (often by changing the concentration in solution) then it is a thermodynamic necessity that the adsorption must change as function of the thickness of the film. In other words, when a molecule is added to effect changes in stability of the dispersion, then the adsorption *must be* a function of separation of the particles. Changes in adsorption are therefore at the heart of controlling surface forces and colloidal stability. It is somewhat surprising that this concept has not been more widely considered.

An important paper in this field is the work by Ninham and Parsegian⁵⁵ where they considered how changes in adsorption of ions as a function of separation between two particles affects double-layer forces. They refer to this concept as “charge regulation” and their approach has been widely adopted for the calculation of electrostatic double-layer forces.^{56, 57} There is an extensive body of work measuring the forces between particles that result from charge regulation, but little effort to *measure* the change in adsorption of ions. Depletion forces are another important example of how changes in adsorption during a collision can affect the forces between particles.^{58, 59}

The change in adsorption during confinement *of ions* can be determined indirectly through comparison of measured surface forces and calculated surface forces (e.g. using the formalism of Ninham and Parsegian). Such an approach is complex if there are many ions, because all affect the surface charge. Alternatively the thermodynamic approach of Hall and Ash *et al* can convert measurements of surface forces as a function of solution chemical potential into descriptions of surface excess as a function of separation. This approach has been used by Pethica⁶⁰ and also by Ducker’s group.^{49, 61-63} In particular Ducker’s group has used this approach to show how confined adsorption of charged surfactants can be very large in magnitude because of the coupling of electrostatics to the hydrophobic effect. A consequence is that the short-ranged hydrophobic effect can strongly affect long-range range double-layer forces. Self-consistent field calculations have also been used to describe confined adsorption.⁶⁴

The purpose of this paper is to describe a *direct* measurement of adsorption as a function of distance between two interfaces. The key application is colloidal stability, but it is difficult to measure tiny amounts at the speeds of particle collision. Instead we transform the time-dependent measurement into a spatial measurement: we investigate a crack where all the separations are measured simultaneously at different film thicknesses within the crack (see Fig. 1b).

Our method consists of two optical measurements: (a) fluorescence emission intensity to obtain the amount of a particular molecule per unit area of a thin film, and (b) interferometry to obtain the thickness of the film. The measurements are made by photographing a liquid-filled crack formed between a silicon wafer and a glass wafer (Fig. 1b). The crack is quasi 2-dimensional such that the liquid film thickness, D , is a function of the distance normal to the crack tip, x , but almost independent of the coordinate parallel to crack tip, y . Because the film thickness varies as a function of distance from the crack tip, a pair of photographs that record both fluorescence intensity and interference as a function of pixel position (x, y location) yield the total amount in the volume that has the area of the pixel and thickness, D , as a function of D . The crack angle is very small, about 0.02° , such that the range of D within each pixel is about 0.7 nm. By comparison of the measured amount to the amount per volume in bulk solution, we obtain the surface excess, Γ , as a function of D . This surface excess includes contributions from molecules directly on the solid and in solution. Here we treat the word “adsorption” as a synonym for surface excess and use the term depletion to mean a negative surface excess. So our measurement of surface excess as a function of D is the desired adsorption as a function of confinement.

We have chosen to investigate the confined adsorption of fluorescein in a thin aqueous film between silica and glass because (a) the high quantum yield enables accurate measurement of a small number of molecules with a simple camera, and (b) fluorescein is charged, so that we expect a strong electrostatic interaction with each interface. Some of the surface silanol groups of silica/glass are dissociated and thus the solids bears a negative potential of -65 to -25 mV⁶⁵ depending on the salt concentration in solution. Fluorescein has two acidic protons ($pK_{a1} = 4.3$ and $pK_{a2} = 6.43$) so at pH 7.6 the fluorescein in bulk solution primarily has a charge of $-2e$, and therefore we expect that fluorescein will be repelled from each interface to produce a negative surface excess.

This paper describes both the development of the method, and results of experiments measuring ion depletion in a thin film. The development of the method is described in the **Analysis** section that follows; this section can be skipped for those interested only in the depletion results. To gain a good understanding of the depletion results however, we encourage the reader to read through at least the **Strategy for measuring surface excess** subsection where the majority of the terms used in the **Results and Discussion** is defined.

ANALYSIS

Strategy for Measuring Surface Excess

The surface excess, Γ , was calculated according to the usual definition, originating from Gibbs:⁶⁶

$$\Gamma_i(D) = \left(\frac{n_i}{A}\right)_f - \left(\frac{n_i}{A}\right)_b, \quad (1)$$

where n_i the amount of species i , and A is the cross sectional area of the solid–liquid interface. From here we will drop the subscript i , and it is understood that we are investigating a single compound, in this case, fluorescein. The subscript, f , refers to the actual amount present in the film, whereas the subscript, b , refers to the amount that would be present if the concentration were the same in the film as in the bulk solution. Note that the results for Eq. 1 is for two interfaces, so the conventional “per interface” surface excess for a film constructed from two identical interfaces is simply the result from Eq 1 at $D = \infty$, divided by 2. Although it was not possible for us to fabricate both walls from the same materials, we did fabricate them from similar materials—thermally grown silicon oxide, and glass. The **Analysis** section is divided into two parts, **Measurement of D** and **Measurement of Γ** , which we measure pixel by pixel in a crack. In our experiments, the crack angle is very small in the x direction and negligible in the y direction, so we treat information from each pixel as if it were of uniform D .

The second term in Eq. 1 can be calculated from the concentration in bulk, c , as follows:

$$n = c \times D, \quad (2)$$

such that:

$$\Gamma(D) = \left(\frac{n}{A}\right)_f - c \times D. \quad (3)$$

In general, there may be systematic errors in the measurement of n_i or perhaps c that might propagate into large errors in the left side of Eq 3. In this case, it might be better to consider the difference between the surface excess at two different thicknesses:

$$\Gamma(D_2) - \Gamma(D_1) = \frac{1}{A} \left(n_f(D_2) - n_f(D_1) \right) - c \times (D_2 - D_1). \quad (4)$$

Note that we measure n_f from the intensity of fluorescence emission, I . In the next section we show that, in general n_f is a complicated function, f , of I , such that:

$$\Gamma(D_2) - \Gamma(D_1) = \left(f(I, D_2) - f(I, D_1) \right) - c \times (D_2 - D_1). \quad (5)$$

Some insight into the use of Eq. 5 can be obtained from the hypothetical situation that would occur if the intensity were simply proportional to the number of molecules. This is very approximately true in our work for $D < 50$ nm and would be a good approximation if interference were very slight. For this situation:

$$\Gamma(D_2) - \Gamma(D_1) = k(D_2)I(D_2) - k(D_1)I(D_1) - c \times (D_2 - D_1). \quad (6)$$

where k is a factor that depends on D . After calibration of k as function of D , we could obtain the surface excess. As we show in the next section, the calibration is more complex. When both D_1 and D_2 are sufficiently large compared to the range of interactions between the solid–liquid interfaces, and channels of the two thicknesses are in equilibrium, then the surface excess should be the same for each, and the right side of Eq. 4 should equal zero. If systematic multiplicative errors in the measurement of amount occur, a correction constant, a , should be incorporated such that

$a \frac{1}{A} \left(n_f(D_2) - n_f(D_1) \right) = c \times (D_2 - D_1)$, for large D_2, D_1 . In practice, we found that $a = 1$ for our experiments.

Measurement of Thickness: Interference

The thickness is required both because our overall objective is to measure the surface excess as a function of known thickness and also because our Eq. 5 requires D . We used interferometry to measure D *in-situ* simultaneously for all x and y .

Fig. 2. is a schematic of interference which occurs between light waves reflected from the glass–solution interface (II), the solution–SiO₂ interface (III) and the SiO₂–silicon interface (IV). Although light also reflects from the air–glass interface (I), the thickness of the Glass ($\approx 800 \mu\text{m}$), is much greater than the coherence length of the illuminating light, and does not contribute to the interference. The incident beam is both reflected and transmitted at each interface resulting in an infinite series of almost parallel beams with decreasing amplitude combining at each pixel of the camera. The action of the objective lens of our microscope means that these rays are not entirely parallel or normally incident and a correction for this effect will be described later. For a perfectly coherent light source each of these rays interferes with every other wave at the point of observation. With the additional consideration of optical incoherence the contributions of multiply-reflected rays vanishes quickly. This interferometry is known as multiple-beam optical interferometry, and we determine the intensity using the transfer matrix method described by Lambacher⁶⁷ (also by Hecht⁶⁸), which accounts for multiple-beam interference from multiple layers.

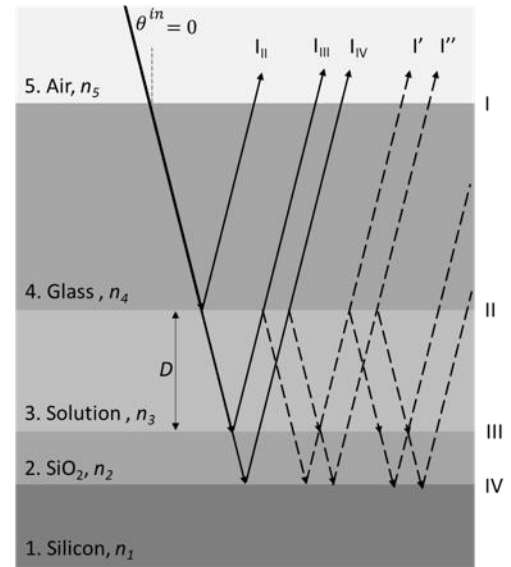


Fig. 2. Schematic showing light rays contributing to interference and a subset (I' , I'') of the possible multiply-reflected rays

To obtain a feel for this method, we briefly describe the situation where there is no oxide layer and only normal incidence, neglecting multiply-reflected rays. Light reflecting from the silicon travels a greater optical path length than light reflecting from the glass–solution interface, a distance which depends on the wavelength, λ , and the refractive index of the solution, n_3 . The relative phase shift is given by

$$\Phi = \frac{4\pi n}{\lambda} D + \pi, \quad (7)$$

where the second term is the additional phase shift on reflection from the silicon. Destructive interference occurs when the phase shift is equal to odd integer multiples of π and constructive interference when Φ is equal to even integer multiples of π . The time-average reflected intensity is given by:

$$I = \frac{1}{2}I_{II} + \frac{1}{2}I_{IV} + I_{II}I_{IV} \cos \Phi, \quad (8)$$

where we have used IV to represent the silicon–solution interface because there is no oxide layer. The intensities can be calibrated by measuring the intensity at both a maximum (constructive interference) and a minimum (destructive interference) in intensity in an image of the crack. Combining these we obtain I_{II} and I_{IV} scaled appropriately. The measured I is used to obtain $\cos \Phi$ from Eq. 8 and thence D from Φ in Eq 7. Due to the periodic nature of the intensity produced by interference (\cos function in Eq. 8), a single value of intensity could correspond to a number of different channel heights. Therefore, to determine the thickness profile, $D(x)$, we assume that $dD(x)/dx < 0$, i.e. D increases with distance from the crack tip. For the more complicated situation where the oxide layer is present, and the angle of incidence is not exactly normal, we use the transfer matrix method to obtain I as a function of D and angle of incidence, averaged over the range of angles admitted by the microscope objective, and invert to obtain D from the measured I .

In practice, we found that the intensity was not uniform in the field of view, independent of the channel width. We correct for this by subtracting the background intensity using a moving average surface fit to the intensity for an area with no features in the field of view.

Measurement of Amount: Fluorescence.

Approach. The total amount of fluorophore per pixel (i.e. at various x,y positions in the channel) was measured by fluorescence emission. The total emission intensity is equal to the sum of contributions from fluorophores at all values of z between 0 and D since there is no interference of fluorescent emission between fluorophores (emission is incoherent). Because the film is thin, we assume that the electric field does not decay from absorption as it travels through the solution. However, interference means that the electric field in the channel, which dictates the fluorescence emission and excitation, is a function of z , which makes this sum non-trivial.

The effect of interference on fluorescence emission was previously described by Lambacher.⁶⁷ In Lambacher's work, the fluorophores were confined to a plane of uniform distance from interface III and there was no glass layer. Here fluorophores are distributed at various distances from interface III.

The forward process of calculating the intensity for a *known distribution* of fluorophores is relatively simple, but the reverse process of determining the number of fluorophores from a given intensity does not have a unique solution. This is because the emission *per fluorophore*, I_j , is a function of z within the aqueous film. Thus a few fluorophores at a z where the I_j is high might give the same total I as a greater number of fluorophores where the I_j is low. Ideally, we would like no interference such that I_j is independent of z , but we need interference to measure the crack thickness. In practice, we have used a thin oxide layer on the silicon to control $\frac{\partial I_j}{\partial z}$. For the conditions of our experiment, this oxide thickness was about 38 nm (See **Minimizing the Error in Assuming Uniform I_j**).

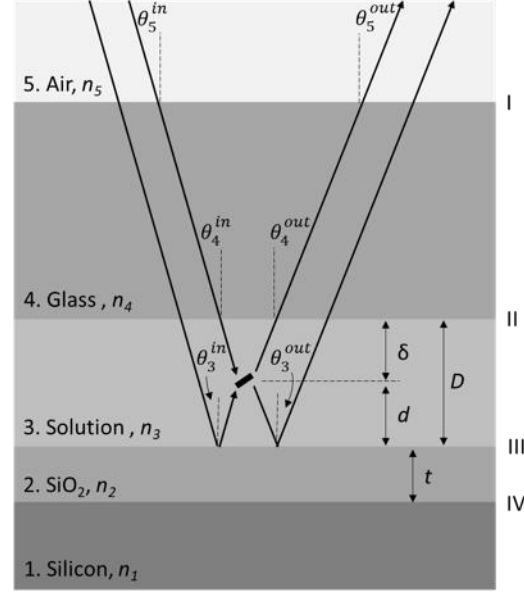


Fig. 3. Schematic of fluorescence intensity.

Optical model We now describe the method for calculating the intensity of emission using the schematic shown in Fig. 3. We introduce the distances of the fluorophore to the SiO_2 , d , and Glass, δ , which are related by $D = d + \delta$. The angle θ_5^{in} is related to θ_4^{in} and subsequent angles by Snell's law. Assuming that the fluorescent lifetime is constant, the detected intensity of fluorescent emission from a particular fluorophore, I_j , is proportional to the product of the probability of excitation, P_j^{ex} , and the probability of detecting emission, P_j^{em} .⁶⁷

$$I_j \propto P_j^{\text{ex}} P_j^{\text{em}}. \quad (9)$$

The probability of excitation is proportional to the time average of the squared projection of the local incident electric field onto the transition dipole of excitation:⁶⁷

$$P_j^{\text{ex}} \propto \int I(\lambda_{\text{in}}) \epsilon_{\text{abs}}(\lambda_{\text{in}}) \int \sin \theta_3^{\text{in}} A(\theta_3^{\text{in}}) U_j^{\text{ex}}(\lambda_{\text{in}}, \theta_3^{\text{in}}) d\theta_3^{\text{in}} d\lambda_{\text{in}}.$$

$$U_j^{\text{ex}} = |\Psi_{\text{in}}^{\perp}|^2 + \cos^2 \theta_3^{\text{in}} |\Psi_{\text{in}}^{\parallel, p}|^2 + \sin^2 \theta_3^{\text{in}} |\Psi_{\text{in}}^{\parallel, n}|^2. \quad (10)$$

Here we have made some changes to Lambacher's original terminology. The unpolarized illumination intensity, I , is written as a function of the incident wavelength, λ_{in} , to account for the emission spectrum of our light source, but in practice we assume that the illumination is uniform across the absorption spectrum. We do account for the wavelength-dependent absorption of the fluorophore, $\epsilon_{\text{abs}}(\lambda_{\text{in}})$. The magnitude of the projection of the incident electric field onto the transition dipole depends on the angle of incidence, θ_3^{in} , and the orientation of the transition dipole. In contrast to Lambacher's work, we have a solution of fluorophores that rotate freely, so we have integrated analytically over all possible orientations of the transition dipole. The aperture function, A , is included to account for the numerical aperture of the microscope. We integrate over the range of λ_{in} transmitted by our excitation filter and the range of angles of illumination. The Ψ refer to the interference terms, which are described in **Supporting Information**.

Similarly, the probability of emission is proportional to the squared projection of the local electric field onto the transition dipole of emission.⁶⁷ In determining the probability of detection, we also account for a wavelength-dependent quantum yield of the detector, Φ_{det} , and the emission spectrum of the dye, $f(\lambda_{\text{out}})$, where λ_{out} is the emission wavelength. We again assume a random dipole orientation. We integrate over the wavelengths transmitted by the emission filter and the range of angles, θ_3^{out} , accepted by the microscope objective.

$$P_j^{\text{em}} \propto \int \Phi_{\text{det}}(\lambda_{\text{out}}) f(\lambda_{\text{out}}) \int \sin \theta_3^{\text{out}} A(\theta_3^{\text{out}}) U_j^{\text{em}}(\lambda_{\text{in}}, \theta_3^{\text{out}}) d\theta_3^{\text{out}} d\lambda_{\text{out}}$$

$$U_j^{\text{em}} = |\Psi_{\text{out}}^{\perp}|^2 + \cos^2 \theta_3^{\text{out}} |\Psi_{\text{out}}^{\parallel,p}|^2 + \sin^2 \theta_3^{\text{out}} |\Psi_{\text{out}}^{\parallel,n}|^2 \quad (11)$$

Lambacher gives the detailed derivation for these proportionalities (Eqs. 10 and 11) but does not integrate analytically over the polar angle of dipole orientation, as we do here. Lambacher also presents experimental validation for his optical model.⁶⁷ The interference coefficients are calculated from the Fresnel coefficients, which are given in the Supporting Information (Eq E1). In order to account for reflection from both the solution/SiO₂ interface (III) and the SiO₂/Silicon interface (IV), we use the transfer matrix method to calculate Fresnel coefficients of reflection for a virtual interface, r^{\parallel} and r^{\perp} , at the position of interface III.

The emissions from individual fluorophores do not interfere measurably with each other because of (a) a random phase lag and broad frequency range and (b) a random subpopulation of fluorophores emit at a given time. Therefore, the intensity contributions of each fluorophore can be summed to give the total intensity. The theoretical fluorescence from a single pixel within the channel (i.e. from a column of solution) containing a uniform distribution of fluorophores spanning $z = 0$ to $z = D$ is proportional to the integral of Eq. 9 from $z = 0$ to $z = D$.

In the next section, we describe some calculations of the expected intensity for various situations. The refractive indices used for these calculations are in Table 1, and the emission and absorption spectra were measured in a Horiba Scientific Fluoromax-4 spectrofluorometer. Our objective accepts light at angles between 0 and 26.74 degrees from the normal, so we set the aperture function equal to 1 for this range and zero elsewhere. Transition dipoles of excitation and emission are assumed to be independently and randomly oriented, since the rotation of the fluorophore is much faster than the fluorescence life-time.¹⁴ The emission and absorption spectra were assumed to be independent of fluorophore position and D . The quantum yield of the detector, illumination intensity, and quantum yield of fluorescence were regarded as constant with respect to wavelength and fluorophore position. Unpolarized light of wavelength 470 ± 20 nm was used for excitation. Emission in the wavelength range of 525 ± 25 nm was received by the detector. All layers other than silicon were assumed to be non-absorbing. The refractive index of silicon is a relatively strong function of wavelength and was treated as such in our calculations.

Table 1. Refractive indices of layers

Layer	Material	n , interferometry ($\lambda=445\text{nm}$)	n , excitation ($\lambda=470\text{nm}$)	n , emission ($\lambda=525\text{nm}$)
1	Air	1.00028 ⁶⁹	1.00028 ⁶⁹	1.00028 ⁶⁹
2	Glass	1.479 ⁷⁰	1.477 ⁷⁰	1.474 ⁷⁰
3	Water	1.337 ⁷¹	1.336 ⁷¹	1.334 ⁷¹
4	SiO ₂ (thermal)	1.469 ⁷²	1.469 ⁷²	1.469 ⁷²
5	Silicon	4.753+0.163 i * ⁷³	4.503+0.108 i ** ⁷³	4.185+0.056 i *** ⁷³

[†] at 546.1 nm

* averaged over 445 ± 25 nm

** averaged over 470 ± 20 nm

*** averaged over 525 ± 25 nm

Minimizing the Error in Assuming Uniform I_j As described above, if I_j were independent of z then we could immediately determine the number of molecules in a column of solution in the crack by measuring the intensity of a particular pixel. I_j is, in general, a function of z , but we can vary the thickness of the oxide thin film, t (see Fig. 1 b), to alter this function. In general, we want experimental conditions such that $\frac{\partial I_j}{\partial z}$ is minimized for all z , and preferably for all D . In some cases, the molecular distribution will have mirror symmetry about the midplane of the channel ($D/2$) because the walls are identical. Our current experiment approximates this symmetry because oxidized silicon is chemically similar to Glass. For cases with mirror symmetry, we should alter t to minimize the gradient of $I_j(z) + I_j(D - z)$ over the range D that is most interesting. In this case, our interest is $0 < D < 65\text{nm}$, where the molecules are most confined.

Some intuition for either minimization can be obtained by considering a simple analogy to conventional interference that produces oscillating patches of high and low intensity. (See Fig. S1 for the interference in a 600 nm thick film.) The gradient in intensity is small at the maxima and minima of intensity, so we could alter the thickness of the oxide such that the aqueous film where we want to measure the adsorption spans a region near the maximum or minimum interference. A high gradient within the oxide is not a problem because there are no molecules of interest there. In contrast, for cracks with mirror symmetry, we might want to position the the aqueous film with the midpoint at points of inversion symmetry of I_j in the interference pattern because a a region of more than average intensity on one side of the mid-plane will compensate for a region of lower than average intensity on the other side.

We expect that changes in adsorption will occur on the length-scale of fields that extend from the surface. For a 1 mM and more concentrated ionic solutions, this is about 0 – 50 nm. For this range it turns out that the variation of $I_j(z) + I_j(D - z)$ is smaller at the inflection point than at a maximum or minimum. Fig.4, top row, shows calculated values of I_j as a function of scaled distance though the film, (z/D) , for oxide thicknesses of 2 nm (native oxide), 38 nm (interference inflection) and 149 nm (interference minimum). The ideal situation is a horizontal flat line for all D , since the intensity could be inverted to give the number of fluorophores for any arbitrary distribution across z . The dotted and dashed lines on each subfigure show the emission for various D . For now, ignore the dotted line that shows a calculation for $D = 215$ nm that is outside the range that immediately interests us. Even for the range of 10–50 nm , the emission for a native oxide film varies by up to $20 \times$ for different positions in the film, so the model says that molecules make vastly unequal contributions to the total intensity of the film. The oxide thickness of 149 nm is locally optimal for minimizing the variation of I_j but the variation is still about 40% from the average, which is unsuitable for interpreting the amount in the film.

The bottom row of Fig. 4 shows deviation of I_j from reflection symmetry about $D/2$. We define deviation as $\frac{I_j(z,D)+I_j(D-z,D)}{2 \int_0^D I_j(z,D) dz} - 1$. The deviation for the native oxide is up to 60%, whereas for the 38 nm oxide, the deviation *varies by a maximum of only 4% over the entire depth of the film for all film thickness in the range $0 < D < 50$* . For this optimized situation, n can be calculated from I with small uncertainty propagating from an unknown molecular distribution than for the native oxide.

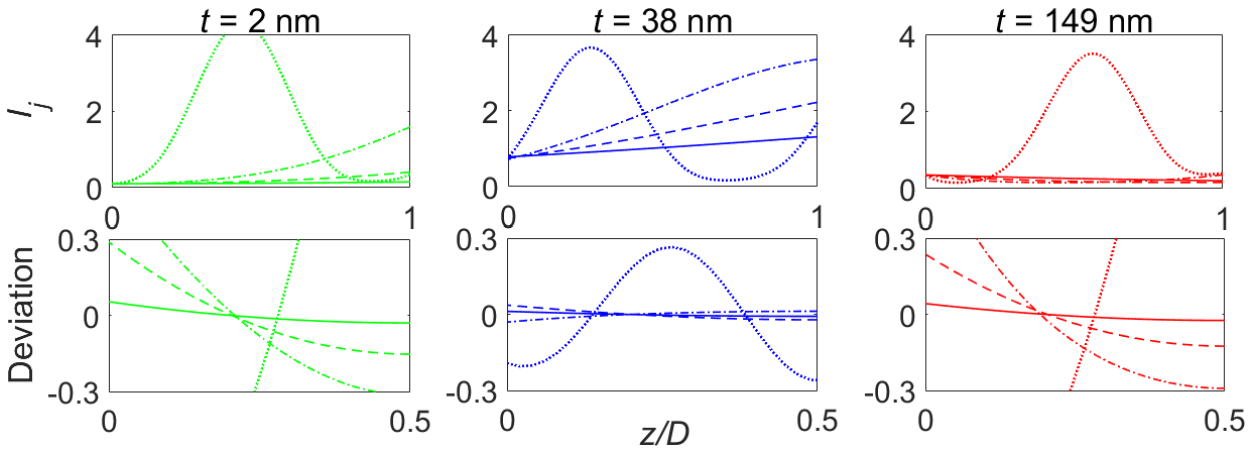


Fig. 4. Intensity of emission of fluorophores calculated for three oxide film thicknesses: 2 nm, 38 nm, and 149 nm. Each plot is shown as a function of scaled distance in the film (z/D) and for 4 different film thickness, $D = 10$ nm (solid line), $D = 25$ nm (dashed), $D = 50$ nm (dot-dashed) and $D = 215$ nm (dotted). The top row shows the intensity, and the bottom row shows the Deviation from mirror symmetry about $z/D = 0.5$. Deviation is defined as $\frac{I_j(z,D) + I_j(D-z,D)}{2 \frac{1}{D} \int_0^D I_j(z,D) dz} - 1$

In the experiments we only use silicon that has an oxide thickness of about 38 nm and the results section focuses on $D < 50$ nm, and therefore we are able to obtain the number of molecules at all D by dividing the measured intensity, I_m , by the average I_j for a particular D :

$$n_f = \frac{I_m}{I_j}, \quad (13)$$

We can obtain the appropriate calibration constant, an effective I_j , simply by measuring the intensity in a calibration solution where we know that the distribution is uniform:

$$n_f = \frac{I_m}{(I_m/DC\lambda)_U}, \quad (14)$$

where C is the concentration and A is the area of the pixel, as above. The U in the denominator indicates that those quantities are measured for the uniform calibration solution. Here we can use a non-adsorbing solution with a short Debye-length for our calibration. In practice, we use the optical model fit to $(I_m)_U$ in the denominator, rather than the experimental data itself because as we show later, the model fits the data very well.

We now consider the error in assuming that the concentration profile is uniform for a 38 nm oxide film. Clearly there are infinitely many profiles to consider, but here we consider two very different profiles that have the same average concentration and mirror symmetry about the mid-plane of the film, consistent with our experiment:

1. Adsorbed – all fluorophores split equally between the two interfaces ($z = 0$ and $z = D$).
2. Mid-plane – all fluorophores concentrated at $z = D/2$.

Figure 5 shows the percentage error, ϵ , in assuming the profile is uniform for $t = 38$ nm. For $D < 50$ nm, the error is $< 4\%$, but for both the adsorbed and midplane profile, the error becomes large at greater separations. Interestingly, the error is also small at 215 nm and 425 nm, an effect that we exploit in the results section.

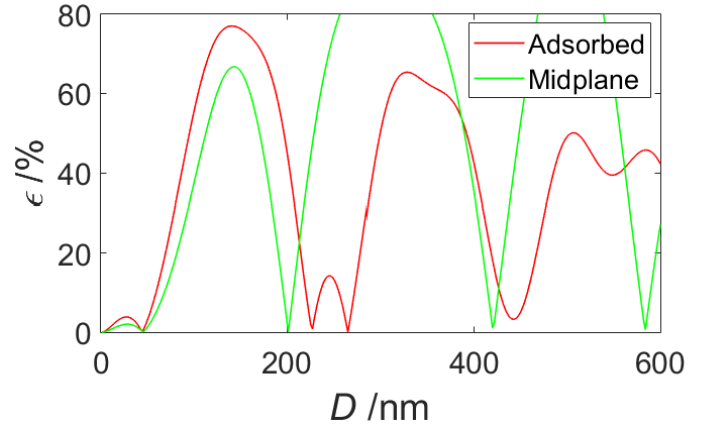


Fig. 5. Relative error in amount when assuming a uniform concentration profile. $\epsilon = \frac{|n_T(D) - n_u(D)|}{n_T(D)}$ where T is the amount calculated for the true profile and u is the amount calculated assuming a uniform distribution.

EXPERIMENTAL

The crack was made by bonding together an oxidized silicon wafer and a borosilicate glass. The silicon (100 mm diameter Silicon <100> N-type) and glass (Schott borofloat 33, 13% B₂O₃, 700 μm thick) (University Wafer Inc.) wafers were cleaned in a Nanostrip solution (Sulfuric acid 90%, Peroxymonosulfuric acid 5%, Hydrogen Peroxide <1%) for 15 minutes at 60°C. The native oxide was then stripped from the Si-wafer using a 10:1 buffered oxide etchant (BOE) solution and subsequently a ~35-40 nm oxide film was grown on the Si wafer by heating in a furnace in O₂ at 1050°C. The silicon and glass wafers are anodically bonded together at 600 V, 230°C with a 440 N tool force. The bond does not extend all the way to the perimeter of the wafer, and the final 1 – 2 mm remain unbonded, with a radial crack with thickness ranging from 0 at the crack tip (bonded) to 5-10 μm at the circumference of the wafer (Fig. S2). The dual-wafer “construct” was cleaved into individual “chips” (~4 mm x 7 mm) after scribing the construct using a diamond scribe. Immediately prior to an experiment, a chip was plasma-treated in oxygen at 200 mTorr vacuum for 30 seconds to clean the surface and expose hydroxyl groups to increase hydrophilicity. Typically wafer cleaning and bonding was performed immediately prior to experimentation to ensure that the interface was clean and free from contaminants.

To test the effect of ionic strength of the solutions on surface excess, the chips were immersed in solutions of constant fluorescein concentration (67 μM) and one of a range of NaCl concentrations (250 μM – 0.4 M). Fluorescein and NaCl were obtained from Sigma-Aldrich and used without further purification. Water was purified in a Milli-Q purification device. The pH was adjusted by addition of NaOH. After a day of immersion, the chips were emersed from solution and then very briefly rinsed in a stream of purified water to clear adsorbed fluorescein from the surface of the chip. Two chips, a reference chip with a short Debye length solution ($c_{\text{NaCl}} = 0.40 \text{ M}$) and a sample chip with a long Debye length solution ($c_{\text{NaCl}} \ll 0.40 \text{ M}$) were then placed on the same hydrophobic microscope slide, spatially separated from each other. A droplet of the appropriate immersion solution was placed at the open mouth of the crack to ensure the thin film in the crack remained in equilibrium with bulk solution of the appropriate concentration. A potential problem is that evaporation of water from the bulk solution (droplet) over the course of the experiment could lead to an increased concentration of fluorophore in the crack. In a typical experiment, it takes about 2-3 minutes to set up and take photographs for analysis. To test whether evaporation was a problem for our experiment, a drop was allowed to evaporate for 5 minutes, and we found no significant changes in intensity over this period (see Fig S3).

An upright fluorescence microscope (Imager.M2, Zeiss) with a CCD camera (Zeiss Axiocam 506 mono) and a programmable stage were used to collect interferometry and fluorescence data. Interferometry was conducted with a $445 \pm 25 \text{ nm}$ filter, in a field of view that included (a) the first few interference fringes for intensity calibration, and (b) the thin (0 – 300 nm) section of the crack. The light source was an X-Cite Series 120Q lamp. A programmable x–y stage and filter cube was used to rapidly switch between locations and filters to enable interference and fluorescence to be measured for both the reference and sample solution conditions.

Details of the optical analysis are contained in the Supporting Information, Details of Analysis for Optical Measurements.

MODELING OF ION DENSITY

The number per area ($\frac{n}{A}$) of fluorescein molecules in each pixel was modelled for each D by first determining the ion concentration at each z from the Boltzmann Equation,⁷⁴ and then integrating over z for each value of D :

$$\frac{n}{A}(D) = \int_0^D n_{F,\infty} \exp\left(-\frac{z_F e \psi(z)}{kT}\right) dz, \quad (15)$$

where ψ is the potential, ϵ is the dielectric constant, ϵ_0 is the permittivity of free space z_F is the valence of fluorescein (–2), e is the charge on the electron, $n_{F,\infty}$ is the number concentration of fluorescein ions, k is the Boltzmann constant and T is the temperature. Recall that the slope of the crack in the y -direction is negligible and the slope in the x -

direction is about 1 nm/ μm . Because the pixel dimension is about 1.4 μm , we assumed that each pixel includes data for a thin film between two flat plates at a uniform film thickness, D , and thus $\left(\frac{n}{A}\right)$ is a function of the z -direction only.

To use Eq. 15, we require $\psi(z)$, which is a function of D and the solution conditions. We calculate $\psi(z)$ from the Poisson-Boltzmann (PB) equation:

$$\frac{d^2\psi}{dz^2} = -\frac{1}{\epsilon\epsilon_0} \sum z_i e n_{i,\infty} \exp\left(-\frac{z_i e \psi(z)}{kT}\right), \quad (16)$$

where $n_{i,\infty}$ and z_i are the number density of each ion in bulk solution, and the valence, respectively.

Silicon oxide and Borofloat 33[®] glass have similar surface chemistry, so we further assume that the crack is symmetric in z about $D/2$. Finally, we make the arbitrary assumptions that the potential is independent of D , but does depend on the background NaCl concentration. Thus,

$$\psi(z = 0) = \psi(z = D) \equiv \psi_0. \quad (17)$$

$\psi(z)$ for each D and for each solution condition was obtained by numerical solution of the PB equation (Eq. 15) using Matlab (bvp4c differential equation solver).

RESULTS

Validation of Optical Model

Our first objective was to validate the optical model for fluorescence emission where interference occurs in a crack. For validation of the model, we require a known distribution of molecules, so we examined a solution with a short Debye-length such that the effects of the surface charge on the ion distribution were limited to a narrow band near the surface. The model was compared to an experiment with 67 μM aqueous solution of fluorescein in water at pH 7.6 in the crack between silicon oxide and glass walls. The solution also contained 0.40 M NaCl such that the Debye-length was 0.5 nm. Since both the fluorescein and the silicon oxide were negatively charged, we did not expect much adsorption directly to the solid, although there may be some adsorption due to van der Waals forces. For these conditions, we expect a distribution of fluorophores that is approximately uniform in z except for a narrow plane of surface excess with small magnitude. Except for the smallest values of D , comparison between the model and experiment should have a small, systematic error because of neglect of this surface excess. This error will be greatest for small D , so we compare model and experiment only for $D > 20$ nm.

The model and experiment are compared in Fig. 6. Since both the experiment and model have arbitrary magnitude of intensity, the model was multiplied by scaling parameter to obtain the least squared difference for $300 \text{ nm} > D > 20 \text{ nm}$, otherwise there are no fitting parameters. Overall, the model captures the shape of the experimental data. The experimental data exhibits weaker curvature than the theory, which may be due to point spread in the microscope image. The agreement is excellent in the range $D < 65 \text{ nm}$ and $D \approx 215 \text{ nm}$, which is the range that we will be using in this work

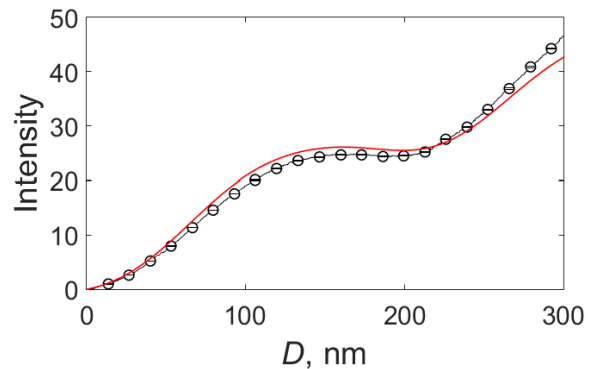


Fig. 6 Comparison between optical model (Eq. 11) and measurement of fluorescence intensity for 67 μM fluorescein at pH 7.6 and $\kappa^{-1} = 0.5$ when the oxide layer is 37 nm thick. The vertical axis has arbitrary units. The model is fit to the data for $D > 20$ nm with a constant scaling factor. The effect of uncertainty in the oxide thickness and the shape of the crack are shown in Fig. S4.

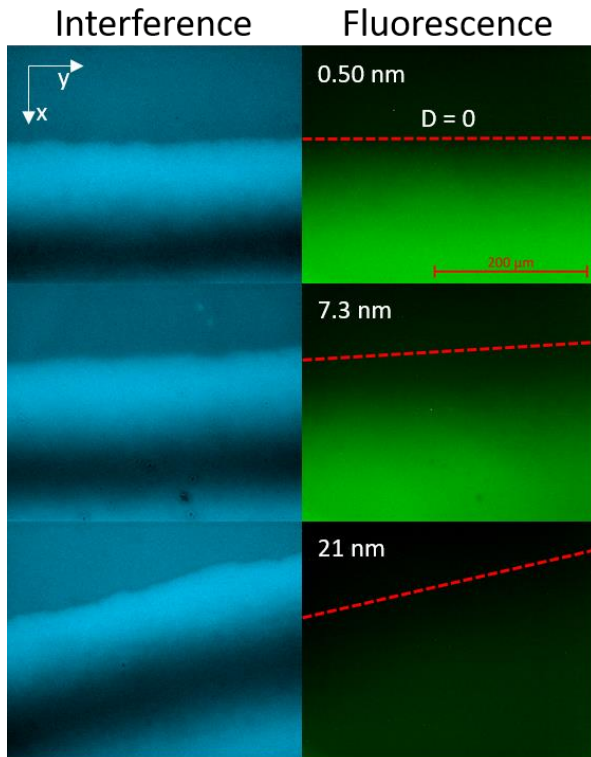


Figure 7: Interference ($\lambda = 445 \text{ nm}$) and fluorescence emission ($\lambda = 525 \text{ nm}$) images of the thinnest part of the crack with Debye length indicated. The part of the crack at the top of each image has approximately zero thickness and the brighter strip is the thinnest part of the crack. The dotted red line on the fluorescence image is a guide, determined from interferometry, that shows the approximate position of the crack tip, i.e. the boundary between where $D = 0$ above and > 0 below.

Qualitative Interpretation of Amounts in the Crack

These results focus on data for an aqueous $67 \mu\text{M}$ solution of fluorescein in water at pH 7.6. The main experimental variables were the distance between the two solids, which was varied merely by examining different x-positions of the crack, and the Debye-length, which was varied by altering the concentration of NaCl. The values for the Debye-length include a contribution from the fluorescein assuming that it was in the fully $-2e$ state. The raw microscopy images for the thinnest part of the crack as a function of Debye-length are shown in Figure 7. The interference was used to measure D and the fluorescence was used to measure n/A . The images for each Debye-length are of a different crack. In each case, the interference shows that each crack was quasi 2-dimensional, and the images have been arranged such that the y axis was approximately with the top of the image. The interference bands are slightly different because in each case the crack has a slightly different opening angle. The maximum and minimum intensity for each crack were used to calibrate the intensity for thickness measurement.

The fluorescence image for each Debye length show a gradient of intensity in the x direction, indicating that there are more fluorescein molecules in the wider part of each crack. In addition, the gradient becomes smaller when the Debye-length is longer, i.e. the negative surface potential is creating a wider depletion zone for the negatively-charged fluorescein in the longer Debye-length solution. For the 21 nm solution, the intensity is still quite low $200 \mu\text{m}$ from the crack tip, whereas at the same distance in the 0.50 nm solution, the intensity is high.

Quantitative Analysis of the Amounts in the Crack.

We used the fluorescence emission from the $\kappa^{-1} = 0.50$ nm solution to calibrate $\left(\frac{n}{A}\right)$ per unit of intensity. An example of the data was shown in Fig. 6. As a reminder, for the short Debye-length solution almost the entire z-range for each pixel is exactly at the bulk concentration so we know the amount from the concentration and the thickness. In principle we could use the experimental data directly as a calibration, but even for a very short Debye length, there could be a surface excess that makes a significant contribution to the amount for very small values of D . Instead we fit the model to the $\kappa^{-1} = 0.50$ nm data in the range 20–65 nm and use this fit. The only fitting parameter is the magnitude. A plot of the fit and the residuals is shown in Fig S5. Note that by using a short Debye-length solution for calibration, we are assuming that the emission intensity is unaffected by the Debye-length. This assumption is validated in Fig. S6.

Figure 8 shows the measured $\left(\frac{n}{A}\right)$ as a function of D for 0.50 nm and 21 nm Debye length solutions. Values of $\left(\frac{n}{A}\right)$ were calculated using from Eq. 13. Since the total fluorescence intensity becomes increasingly dependent on the z distribution of molecules for $D > 65$ nm, we focus on $D < 65$ nm. For any D , $\left(\frac{n}{A}\right)$ for the longer Debye-length solution is less than or equal to the value for 0.50 nm Debye-length solution, showing that the depletion is greater in the longer κ^{-1} solution.

Fig. 8 also shows the results of the simple PB model with a surface potential of -70 mV. The model gives the same features, suggesting that the surface excess is dominated by electrostatic depletion.

Fig. 9 shows the experimentally determined negative surface excess, Γ , as a function of film thickness (calculated from Eq. 1). All the solutions show a negative surface excess (depletion) of fluorescein, as expected for a negatively charged ion in a crack with walls that have a negative potential. The surface excess extends further away from the solid for longer κ^{-1} , as expected. The magnitude of depletion is relatively insensitive to κ^{-1} for $D < 10$ nm, but for thicker films, the surface excess has greater magnitude for longer κ^{-1} . For $\kappa^{-1} = 4.0$ nm, the surface excess has reached a plateau of about -0.0080 fluorescein ions/nm² at about $D = 40$ nm. Greater separations simply have more bulk solution around the film midpoint. Since there are two interfaces in our experiment, we consider half of this, -0.0040 ions /nm² to be the surface excess for a single isolated interface. The isolated surface excess for $\kappa^{-1} = 7.3$ nm is -0.0080 ions /nm², 14 nm is -0.010 ions /nm², and for 21 nm -0.011 ions /nm².

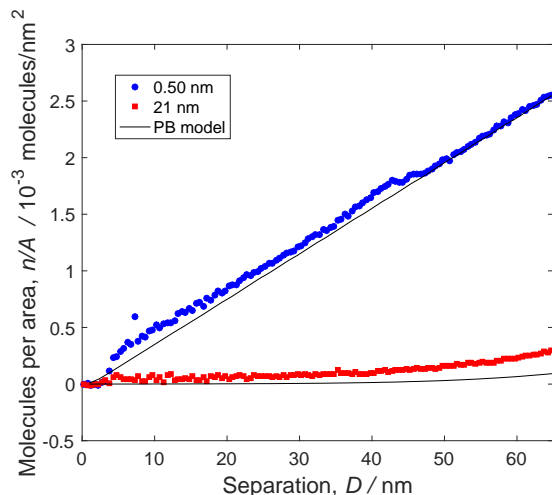


Figure 8: Number, n , of fluorescein molecules per unit area, A , for solutions of constant fluorescein concentration, $C_{\text{Fl}} = 67 \mu\text{M}$. Results are shown for two Debye-lengths. $C_{\text{NaCl}} = 0.40$ M ($\kappa^{-1} = 0.50$ nm), and $C_{\text{NaCl}} = 0$ mM, ($\kappa^{-1} = 21$ nm). Lines show the results from the PB model calculated using a surface potential of -70 mV that was obtained from fits of surface excess at infinite separation. Data is collected over the entire image (239,360 pixels) and binned using a bin width of 0.25 nm.

Fig. 9 also indicates that the trends for the PB model are consistent with the measured data. In comparing the two, it is important to note that there is an error of about ± 2 nm in the position of $D=0$ (See Supporting Information), and a smaller error in the background intensity that propagates into a shift in the surface excess. Each of these affects the comparison between fit and experiment. A more sophisticated model, e.g. including charge regulation instead of constant surface potential may produce a better fit.

One of our objectives in this work is to determine how the surface excess differs in a confined film and an isolated film. From Fig. 9 we see that, for $\kappa^{-1} = 14$ nm or 21 nm, the surface excess has not plateaued even at 65 nm. There are two ways that we could obtain the surface excess for the isolated surface of these longer κ^{-1} solutions. The first is to assume that the PB equation accurately models the surface excess, fit the PB in the range of measurement, obtain the surface potential, and then calculate the surface excess. Such an approach has the obvious disadvantage that it relies on the accuracy of the PB model in representing the data. The PB assumptions of point ions, electrostatics only, and no correlations mean that accuracy is not assured.

Alternatively, we require an accurate measurement of surface excess at even greater D . Unfortunately, our modeling shows that the conversion from intensity to amount is, in general, sensitive to the distribution of molecules for $D > 65$ nm. But at $D = 215$ nm (see Fig. 5) there is a sweet spot where even extremely different distributions – all at the walls, or all at the mid-plane – differ by only 20%. Knowing this, we used $D = 215$ nm to obtain data for the surface excess of an “isolated” surface for the 14 and 21 nm solutions; $215 \text{ nm} > 10 \kappa^{-1}$ for all the solutions. The error for the unknown distribution is probably much smaller than the 20% suggested by Fig 5 because at this large separation much of the z -range of the film is at constant (bulk) density. Using the results at 215 nm, we have calculated Γ_{∞} (the conventional surface excess) for the long Debye-length solutions, where the surface excess had not plateaued at $D = 60$ nm. Γ_{∞} is -4.1×10^{-3} molecules/nm² for $\kappa^{-1} = 21$ nm and -2.2×10^{-3} molecules/nm² for $\kappa^{-1} = 14$ nm. So our technique can be used to calculate the conventional surface excess. Knowledge of Γ_{∞} allows us to achieve our objective of calculating how much the surface excess changes with confinement compared to the isolated case, $\Delta\Gamma =$

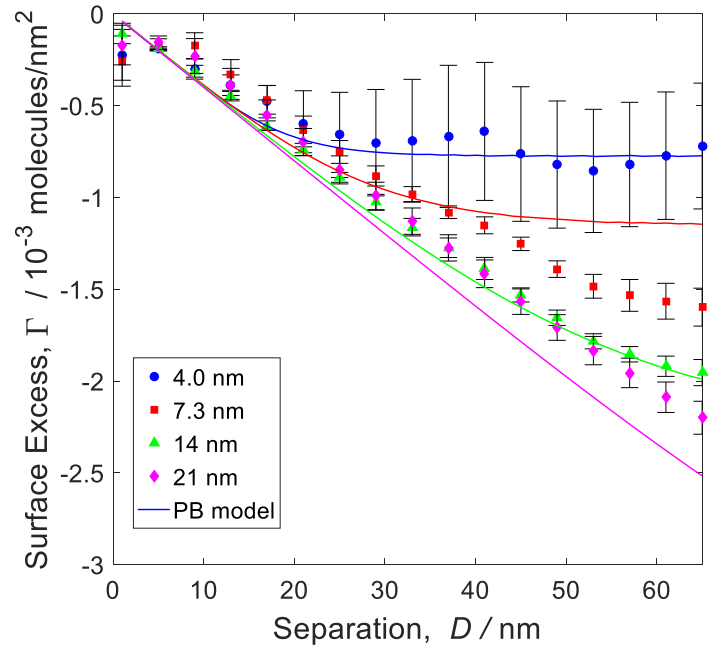


Figure 9: Surface excess of fluorescein as a function of film thickness for different solution Debye lengths. The Debye-length was reduced by addition of NaCl. The PB model includes a fit to the surface potential at infinite separation, which was -65, -50, -50 and -70 mV for κ^{-1} of 4, 7, 14 and 21 nm respectively. The 7 nm data did not fit well to the model. Error bars are \pm standard error of measurements for three different crack chips.

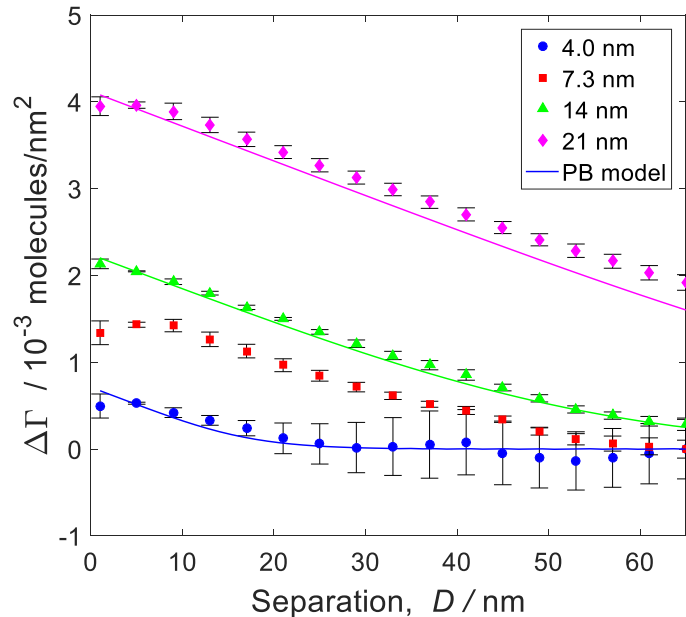
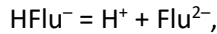


Figure 10: Difference in surface excess of fluorescein in thin film (separation shown) and for isolated film. Isolated film was $D = 65$ nm for 4 and 7 nm solutions and $D = 215$ nm for 14 and 21 nm solutions. The PB fit for the 7.3 nm solution has been omitted. Note that

$\Gamma - \Gamma_\infty$ (Eq. 4), and the results are shown in Fig. 10. Note that about half of the depleted amount at infinite separation for the $\kappa^{-1} = 14$ and 21 nm solutions has already been eliminated at fairly large separations, $D = 3\kappa^{-1}$. At 65 nm separation of the crack walls, the solution is depleted by 28%, 61%, 75% and 85% compared to the bulk for 4, 7, 14, and 21 nm solutions respectively. In cases where the surface excess is zero at $D = 0$, $\Gamma_\infty = -\Delta\Gamma$. Fig. 9 shows that this is a good approximation for fluorescein between silica/glass, so the vertical intercept in Fig. 10 shows minus the conventional surface excess for an isolated interface.

Effect of Fluorescein Equilibria

In bulk solution of fluorescein, there is an equilibrium between the cationic, neutral, monoanion and dianion species. The cationic and neutral species do not concern us at the conditions of the experiments, pH 7.6. The equilibrium between the two charged species:



has $\text{pK} = 6.71$, which is sufficiently far from the solution pH that the bulk solution is predominantly in the Flu^{2-} form. However, the presence of the surface potential affects this equilibrium such:

$$\left[\frac{C_{\text{Flu}^{2-}}^\psi}{C_{\text{HFlu}^-}^\psi} \right] = \frac{K_d}{C_{\text{H}^+}^{\text{bulk}} \exp\left[-\frac{F\psi}{RT}\right]}. \quad (18)$$

Thus a negative potential, which is the situation in the double-layer in the crack, tilts the ratio in favor of the monoanion, which is weakly fluorescent. Calculations of the ion ratio for a variety of surface potentials are shown in in Fig. S7, At pH = 7.6 and

50 mV, $\left[\frac{C_{\text{F}^{2-}}^\psi}{C_{\text{HF}^-}^\psi} \right] \approx 1$. (Note that this is not the ratio for all z, D within the crack, just for locations where the potential is 50 mV.) Thus we would expect that for thinner films and longer Debye-lengths, l would be lower than expected for an all dianion solution because an increasing fraction of the fluorescein should be in the monoanion form.

This is a potentially problematic issue for our measurements so we examined the effect of speciation by comparing the surface excess at pH 7.6 and pH 8.4. For 65mV potential, the $\left[\frac{C_{\text{F}^{2-}}^\psi}{C_{\text{HF}^-}^\psi} \right]$ ratio calculated from Eq 18 is 3.6 for pH 8.4 and 0.5 for pH 7.6. Yet the experimental results in Fig. 11 show only a minor difference in surface excess for the two Debye-lengths (4 nm and 21 nm). Thus the experimental results are consistent with the idea that $\text{F}^{2-}/\text{HF}^-$ speciation is not a very important effect in our experiments. At present, it is not clear to us why this equilibrium is unimportant.

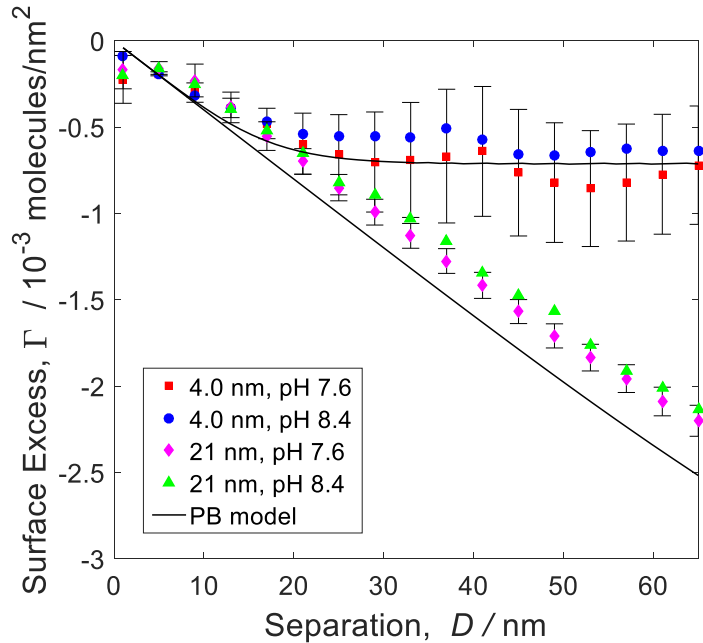


Figure 11: Comparison of Surface Excess measurements at pH 7.6 and 8.4. The surface excess was calculated assuming that all of the fluorescein is in the F^{2-} form. The effect of pH on the surface excess is slight.

DISCUSSION

Determination of the Molecular Distribution, $n(z)$, from the Fluorescence Emission

For the experiments described here, we deliberately added an oxide film to the silicon wafer such that all symmetrical distributions have very nearly the same emission per molecule, (Figs 4 and 5). This enabled measurement of the total n/A without knowledge of the molecular distribution (n/A as a function of z). Fig. 4 shows that different oxide thicknesses result in different *total* emissions, so if one could set up an experiment where there were a variety of oxide layer thicknesses for the same D , then one could obtain additional information about the *distribution of molecules*. For example, one could measure the intensity at $D = 50$ nm for $t = 2$ nm and $t = 38$ nm. From the emission at $t = 38$ nm, one knows the total number of molecules, irrespective of the distribution. At $t = 2$ nm, the emission is asymmetric (e.g. it is $19 \times$ greater at $z = 50$ nm than at $z = 0$) and thus a greater signal will be observed if the molecules are concentrated on the high- z side of the mid-plane, which can then be used to determine whether there are more molecules on the high z -side. The deviation plots are also asymmetric about the mid-plane, which provides information about the distribution even in symmetric cases.

Measurement of Surface Potential

From the best fit of the PB model to the measured surface excess, we can estimate the surface potential, given the assumptions of the PB model.⁷⁶⁻⁷⁸ Fig. 12 compares the fitted surface potential to those measured for silica–glass by Colloid Probe atomic force microscopy (AFM) and Surface Forces Apparatus (SFA) experiments. The comparison is made for the same Debye length and it should be noted that there is no fluorescein in the AFM measurements. The current technique is not at all sensitive to the surface potential for short κ^{-1} which means that the comparison between model and experiment for $\kappa^{-1} = 4$ nm in Figs 9 and 10 has no fitting parameters. The agreement between the measured and modelled surface excess under such conditions is remarkable. For the $\kappa^{-1} = 14$ and 21 nm solutions, the PB fit is sensitive to the surface potential, which allows us to measure a fitted potential. The reasonable agreement between fitted potentials shown here and from forces measurements suggests that the method described here could be used to measure the surface potential for moderate salt concentrations. Because the diffuse layer is strongly perturbed for high potentials and long Debye-lengths, the technique should be well suited for these conditions; this is exactly the condition for which surface forces measurements are not well suited to measure the surface potential.

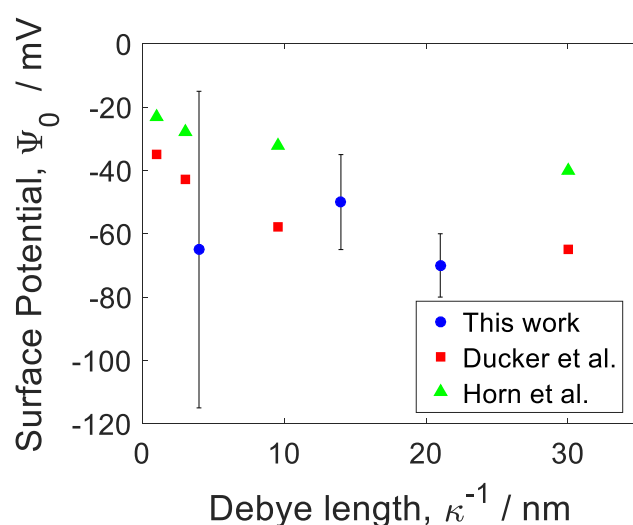


Figure 12: Comparison of surface potential measured from fluorescence intensity and from force measurements for the glass–silica system. AFM results from Ducker et al.⁶⁵ Surface Forces measurement from Horn et al.⁷⁵ The huge error bar for $\kappa^{-1} = 4$ nm indicates that our technique is not useful for measuring potential for this condition.

CONCLUSIONS

We describe a simple, inexpensive method for measuring adsorption in a thin film as a function of the film thickness (confinement) using an optical microscope. The method has high spatial resolution and high resolution in amount. The method also provides an estimate of the surface electrical potential at infinite separation when a charged ion is examined in moderate salt concentration. The surface excess was measured for the divalent anion, fluorescein, as a function of the thickness of an aqueous film between silica and glass. Fluorescein was depleted in the thin film

compared to in bulk. The magnitude of depletion (a) decreases with decreasing film thickness, and (b) increases with κ^{-1} for the same film thickness. The range of variation in depletion increases with increasing κ^{-1} . The method could resolve changes in fluorescein surface excess in films that were up to $7\kappa^{-1}$. The adsorption behavior has semi quantitative agreement with a simple Poisson-Boltzmann model. The lack of adsorption in very thin films (<5 nm) and the agreement with the PB model each suggest that fluorescein adsorption to silica is dominated by electrostatics.

SUPPORTING INFORMATION

The supporting information contains:

- A. Interference terms used to calculate Eq. 10
- B. Figures
 - a. results of calculation of interference fringes
 - b. Image of the wafer
 - c. effect of changes in oxide film thickness
 - d. crack profile
 - e. fit of optical model to data
 - f. Fluorescein emission as a function of Debye-length
 - g. Fluorescein speciation
- C. Details of optical analysis

Chapter 3: Effect of background electrolyte concentration on surface excess of the fluorescein dianion in concentrated electrolytes

This chapter reproduces original work published in *Langmuir* on April 4, 2019 in Volume 35, pages 5719 – 5727. In this chapter I describe the effect of very concentrated (2–10 M) background electrolytes (NaCl, LiCl and CsCl) on the adsorption behavior of fluorescein, a dianion, next to negatively charged interfaces under basic conditions in concentrated electrolytes. This work was undertaken to determine whether the decay length of the potential was equal to the Debye length in concentrated electrolyte.

Dr. William Ducker provided guidance on experiments and contributed to the writing of the paper.

The following article is reprinted (adapted) with permission from Gaddam, P.; Ducker, W., A., Electrostatic Screening Length in Concentrated Salt Solutions. *Langmuir* **2019**, 35 (17), 5719-5727. Copyright 2019 American Chemical Society

The Electrostatic Screening-Length in Concentrated Salt Solutions

Prudhvidhar Gaddam[†] and William Ducker*

Department of Chemical Engineering and Center for Soft Matter and Biological Physics, Virginia Tech,
Blacksburg, VA 24061, USA.

*For correspondence: wducker@vt.edu

Submitted to *Langmuir*

William Ducker ORCID ID: 0000-0002-8207-768X

Prudhvidhar Gaddam ORCID ID: 0000-0002-5909-3999

ABSTRACT

Thin films (0–30 nm) of very concentrated aqueous monovalent salt solutions (2–10 M of LiCl, NaCl and CsCl) were examined to determine how ionic strength affects the screening-length of the electrostatic potential. Measurements were consistent with a screening-length in the range 3–12 nm. The screening-length increased monotonically as a function of salt concentration and the rate of increase was a function of the monovalent salt type. The results were incompatible with the Debye-length of Poisson-Boltzmann theory, but consistent with previous measurements of surface forces. The screening-length was determined from the surface excess of fluorescein, a di-anion under basic conditions, which was present in trace amounts in the thin film, and was detected via its fluorescence emission. That is, we directly observed that the ion concentration in very concentrated solutions is perturbed far from an interface.

INTRODUCTION

Debye-Hückel theory yields an electrostatic screening length in ionic solutions that depends on the number density of ions, $c_{b,i}$:

$$\kappa_D^{-1} = \sqrt{\frac{\epsilon_0 \epsilon_r kT}{\sum_i c_{b,i} e^2 z_i^2}} \quad (1)$$

where ϵ_0 is the permittivity of free space, ϵ_r is the zero-frequency dielectric constant of the continuous medium, k is the Boltzmann constant, T is the temperature, e is the elementary charge, z is the number of charges on an ion, and the sum is over all ionic species, i , in the solution. This screening-length is also the decay-length of double-layer surface forces that are predicted by Poisson-Boltzmann (PB) theory for symmetric electrolytes in the limit of low potential or large separation, and is known as the Debye-length.⁷⁹ The Debye-length of Eq. 1 agrees well with the experimental measurements of the decay length of surface forces in aqueous salt solutions up to about 1 M where double-layer forces are expected to dominate.^{65, 80, 81} The inverse relationship between concentration and κ_D^{-1} means that the decay length predicted from Eq. 1 becomes very small in concentrated solutions. For example, $\kappa_D^{-1} \approx 0.3$ nm in 1 M solution, and $\kappa_D^{-1} \approx 0.10$ nm in 6 M 1:1 aqueous electrolyte solution. With such a short decay length, a range of other short-ranged interactions such as van der Waals interactions, molecular layering,⁸²⁻⁸⁶ and hydration,^{81, 87} would dominate electrostatic double layer forces *at all separations*. Until recently, double-layer forces in concentrated solutions have received little attention, perhaps because even large-scale (e.g. factor of 2×) departures from Eq. 1 might still result in double-layer forces being obscured by other short-range forces.

Interest in concentrated ionic solutions has recently increased because of results that emerged from the study of room temperature ionic liquids. Room temperature ionic liquids can be composed entirely or mainly of ions, and therefore the Debye-length predicted by Eq. 1 would be very small. Surface forces measurements in ionic liquids from Israelachvili's group, however, revealed a decay length of the force, about 10–13 nm, that was much greater than expected from Eq. 1.⁸⁸ Assuming that the force that Israelachvili's group measured is a double-layer force, for a 1:1 electrolyte this corresponds to a concentration of order 10^{-4} M from Eq. 1. The authors explained the much longer decay length using the idea that the ionic liquid acted as if it were not fully dissociated, and estimated a degree of dissociation of about 10^{-4} based on a fit of the decay of force to Eq. 1. An increase in temperature was observed to decrease the decay length, which was explained from an increase in dissociation with temperature.⁸⁹ Subsequent measurements by a variety of groups confirmed the existence of a long-ranged repulsive force in ionic liquids ("anomalous decay"), but there has been extensive discussion about the origins of the long decay length.^{86, 88-98}

PB theory assumes that the ions have point size and are non-polarizable, the solvent is continuous, and importantly, that the local field at an ion is caused only by that ion; that is, there are no ion-ion correlations.⁹⁹ Kjellander has provided an explanation of the long decay length by accounting for the ion-correlations that were excluded in PB theory.^{99, 100} This approach was used previously to account for forces in CaCl_2 solution.^{101, 102} At large separations between surfaces, Kjellander's theory gives a decay similar to Eq. 1, but includes an effective dielectric constant, ϵ_r^* , and an effective charge, z_i^* :

$$\kappa_K^{-1} = \sqrt{\frac{\epsilon_0 \epsilon_r^* kT}{\sum_i c_{b,i} e^2 z_i^* z_i^*}} \quad (2)$$

Rather than considering only a small fraction of ions to be dissociated, this model considers that the ions are all dissociated, and that correlations result in each ion being “dressed” with other ions that reduce each ion’s effect on the screening length.⁹⁹

If ion-correlations cause such a radical departure from the Debye-length for ionic liquids, it seems reasonable that the same physics would apply in concentrated solutions of simple salts such as LiCl, NaCl, and KCl. Such concentrated solutions are important in Li-ion batteries,¹⁰⁴ supercapacitors¹⁰⁵, sea water concentrated by evaporation, in crystallization,^{106, 107} and water-in-salt solutions.¹⁰⁴ In fact a much longer decay length than predicted by Eq. 1 has been measured in aqueous Li⁺ or Cs⁺ solutions by Valtiner’s Group¹⁰³ and in NaCl by Perkin’s group.⁹³ Thus, as a function of concentration, the decay length decreases to about 1 M, then increases (Fig. 1). Lee *et al* have hypothesized that the screening in concentrated simple salts results from an approximately neutral ionic lattice of ions containing defects arising from water and the finite temperature.⁹⁶ This will be considered further in the discussion section. Table 1 shows just how small the average spacing is between ions in very concentrated NaCl solutions, and how few water molecules there are for each ion. In crystalline NaCl at room temperature and pressure, the Na⁺– Na⁺ center–center nearest neighbor spacing is about 0.56 nm along a crystal axis. If we assume the same lattice structure in solution, then the spacing in a 5 M solution is not much greater – about 1.15 nm. Such densely-packed ions make the Poisson-Boltzmann assumption of uncorrelated ions look very doubtful.

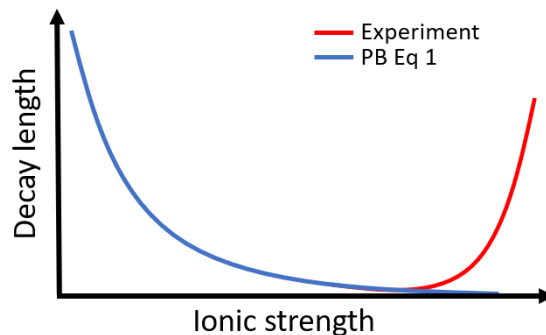


Fig. 1 Schematic of the effect of salt concentration on the decay of double-layer forces. The experimental data is contained in refs ¹⁰³ and ⁹³.

Table 1: Number of water molecules per NaCl unit and ion spacing

Concentration (mol/L)	$n_{\text{H}_2\text{O}} : n_{\text{NaCl}}^{\text{a}}$	Ion spacing ^b (nm)
1	50:1	1.88
2	26:1	1.36
3	16:1	1.30
4	12:1	1.18
5	10:1	1.15
Crystal		0.56 ¹⁰⁸

- n_{ion} is the total number of NaCl units. Results determined by measurement of the mass of water and NaCl required to prepare the stated molar solution.
- Assuming face-centered cubic lattice, this is the center-to-center distance between Na⁺ ions along the crystal axis .

To date, all experimental results showing the increase in decay length with increasing salt concentration at high salt concentration were based on measurements of the force between two interfaces separated by a thin aqueous film (using the surfaces forces apparatus (SFA)⁸⁰). The principal purpose of the current work is to provide evidence of the long decay-length using a completely independent technique. Whereas previous work measured a decay in *force* assumed to arise from a decay in electrical potential, here we measure the *number of ions* in solution between two flat plates,¹⁰⁹ which we also assume depends on the electrical potential in the thin film between two solid–liquid interfaces. We measure the number of trace fluorescent ions in the thin film as a function of the thickness of the film, and extract a fitted decay length. A key aspect of the technique is that we are able to hold the interfaces at a fixed separation in a solution of constant chemical potential until such time as we see no further change. This takes about one day. Thus, we interpret our experiments as

measurements of the equilibrium state, and we are relatively unencumbered by issues of dynamic events such as diffusion, lubrication forces, etc., that are interesting, but more difficult to interpret. Our measurements focus on confined films, so examine the decay length in confinement and leave open the question of whether the decay length is different for a single interface.

Our measurements can be understood qualitatively as follows. If the decay length of the potential were much less than the film thickness, then there would be a region near the midplane between the interfaces where there would be no gradient in concentration. Successive incremental decreases in the film thickness would produce only a linear decrease in the number of ions because a layer of constant concentration would be removed; deviation from this linear relationship corresponds to spatial variation in concentration and thus the existence of a decaying potential. If we assume that the electrical potential is the only potential that decays over more than a nanometer or so from the solid–liquid interface, then by default we measure the decay of the electrical potential. This is essentially the same assumption used in surface forces measurements to infer the decay of double-layer forces and the associated electrical potential.

Our measurements utilize a low concentration of fluorescein, a fluorescent di-anion, in a gently-sloping crack formed by bonding an oxidized silicon wafer to a silica wafer. We photograph the liquid-filled crack twice obtaining: a) a fluorescence image to measure the number of molecules per unit area and b) an interference image to measure the film thickness in the crack for a set of film thicknesses.¹⁰⁹ Each test solution also contains simple 1:1 metal chloride solution in the range 2–10 M, which is about 10^5 times more concentrated than the fluorescein. Our previous measurements using this technique show that PB theory accurately describes the decay-length in solutions that are less than 1 M.¹⁰⁹ Our primary conclusion is that the “anomalous” decay observed in force measurements is also observed in measurements of the number density of fluorescent ions in salt solutions in thin films. We also explore the effect of the cation type (Li^+ , Na^+ , and Cs^+) on the fitted decay length and potential. Finally, we show that concentrated solutions of these simple monovalent ions can reverse the sign of the effective surface potential as predicted by Qiao et al.¹¹⁰ This conclusion diverges from earlier streaming potential measurements at lower concentrations where charge reversal was not observed.¹¹¹

EXPERIMENTAL

Experiments were performed on chips (see schematic in Fig. 2) that were prepared by bonding an oxidized silicon wafer (100 mm diameter Silicon <100> N-type, University Wafer Inc.) to a borosilicate glass wafer (Schott Borofloat 33, 13% B₂O₃, 500 μm thick, flat edge, University Wafer Inc.). Critically, the bond did not extend to the circumference, such there was a very small air gap around the circumference. We refer to the section of the unbonded region where the wafers are separated by only 0–100 nm as “the crack” and the boundary between the bonded and unbonded region as the “crack tip”. At the crack, the wafers were inclined at an angle of about 0.02°. The bonded wafers were broken into chips that contained the unbonded region. The fabrication of the chips and analysis of amount and thickness is described in an earlier publication.¹⁰⁹

Test solutions contained (a) a simple salt of LiCl, CsCl, or NaCl at a concentration in the range 0.5 – 10 M, (b) fluorescein in the range 3.75 – 15 μM (i.e. about 10⁶ more dilute than the simple salt), and (c) NaOH to bring the pH to 9.4 ($c_{\text{NaOH}} \approx 10 \mu\text{M}$, also about 10⁶ more dilute than the simple salt), where the fluorescein exists as a highly fluorescent dianion. The chips were immersed in a solution for at least 12 h prior to an experiment to allow equilibration. The simple salts were roasted overnight in a furnace at 375°C to combust organic contaminants. Water was purified using a Milli-Q purification device. For each concentrated salt solution ($c_{\text{MCl}} \gg 0.50 \text{ M}$) that we examined, we also examined a reference chip with relatively dilute salt solution ($c_{\text{MCl}} = 0.50 \text{ M}$) that enabled calibration of the emission intensity. Salt solutions exhibit significant volume change on mixing, so each solution was prepared in a graduated cylinder by weighing the appropriate mass of salt for a specific concentration and adding in volumes of water (while mixing) using a micropipette until the desired volume for the target molar concentration was reached. The refractive indices of the salt solutions were measured as required for the optical analysis and are provided in Table S1 in the supporting information.

Our standard fluorescein concentration was 15 μM, but for very concentrated salt solutions (>5 M), seemingly anomalous results led us to believe that the concentration at the interface has exceeded the level required for significant quenching, and experiments were repeated at a series of diminishing fluorescein concentrations until (a) we could obtain a plateau in intensity at large separations and (b) we could obtain the same intensity/bulk concentration for successive dilutions. The results were consistent with the idea that the concentrated salt solutions lead to an increase in the concentration of fluorescein at the solid–liquid interface and therefore self-quenching. For the most concentrated salt solutions ($c_{\text{LiCl}} = 7 \text{ M}$ and $c_{\text{LiCl}} = 10 \text{ M}$), experiments were performed at a fluorescein concentration of 3.75 μM.

Separation, D , was measured using interference of 445 nm light and the amounts in the crack per unit area, n/A , were measured using fluorescence microscopy.¹⁰⁹ In the interference images shown in Figure 2, multiple interference fringes are observed orthogonal to the crack tip, (position on the picture is given by the red dotted line) indicating monotonically increasing separation orthogonal to the crack tip. The minimum and maximum intensities were used to calibrate the intensity for the thickness measurement. As the pixel size is fairly large (1 μm x 1 μm) in comparison to the measured gradient in separation ($\approx 0.7 - 0.9 \text{ nm/pixel}$), we treated the sample in each pixel as a pair of parallel plates at a single film thickness. The position of the interference bands vary from image to image as each sample has a different crack angle. n/A was calibrated using a reference chip that contained a solution of fluorescein and the same salt type, but at 0.5 M concentration. We assume that the decay-length is very short at 0.5 M, and so the solution concentration in the thin film is the same as in bulk and therefore known for all but the thinnest films. We fit the experimental data for the 0.5 M solution to the optical model from 10 nm to 150 nm and also set both model and experiment to zero intensity at zero separation. That optical model fits the data very well, as shown in previous work.¹⁰⁹ Once the optical model has been calibrated using the 0.5 M solution, it can be used to determine the amounts in the more concentrated solutions where

the amounts in the thin film is unknown. The dependence of the fluorescence on salt concentration is minor, as shown in Fig. S1.

Each salt condition was measured three to four times using chips from three to four different sets of wafers and three to four fresh salt solutions. Error bars indicate the standard error of a parameter from these four independent measurements. Errors arising from the salt-dependence of the fluorescence, and the optical model are considered in Supporting Information, Fig S1 and S2. Repeat measurements on the same chip showed a much smaller standard error than repeats from different chips, from which we conclude that the main source of variation was differences in the surface chemistry and roughness of the chip.

RESULTS

Surface Excess in Concentrated Salt. Our results utilize aqueous 15 μM solution of the fluorescent compound, fluorescein in water at pH 9.4. Fluorescein is divalent at this pH. The experimental variables are the separation between the two interfaces, D , the concentration of simple salt and the type of cation in the chloride salt (LiCl, NaCl, or CsCl). The separation, D , was measured using interference, and the amounts per area in the crack, n/A , were measured using fluorescence microscopy. The raw microscopy images for the thinnest section between the wafers (the crack) are shown in Fig. 2 for 0.5 M and 5.5 M NaCl solutions. The greater intensity in the $D = 0 - 30$ nm region for the 5.5 M solution indicates a positive surface excess of (anionic) fluorescein, which suggests that the interfaces are now positively charged.

The primary metric that we use to quantify the decay of the electric field is the surface excess. The surface excess of fluorescein, $\Gamma(D)$ is defined as:

$$\Gamma(D) = \frac{n}{A} - c_{b,\text{Fl}}L \quad (3)$$

where $c_{b,\text{Fl}}$ is the bulk concentration of fluorescein in solution and n/A is the number of fluorescein molecules per area the thin film. Fig. 3 shows the experimentally determined surface excess as a function of separation, salt concentration, and monovalent salt type. The surface excess, by definition, should plateau at large separation, which corresponds to the traditional surface excess that is considered for isolated interfaces. The plateau is evident in all our results, with the possible exception of 10 M LiCl which, as we shall see later, has a long decay length). All solutions of LiCl and NaCl show a positive surface excess of fluorescein; this surface excess was evident in Fig. 2 as the increased fluorescence visible to the eye. For LiCl and NaCl the gradient in surface excess decays to zero over a range of order 10 nm, which is much longer than the ≈ 0.1 nm predicted by Eq. 1. This is the central result of the current paper.

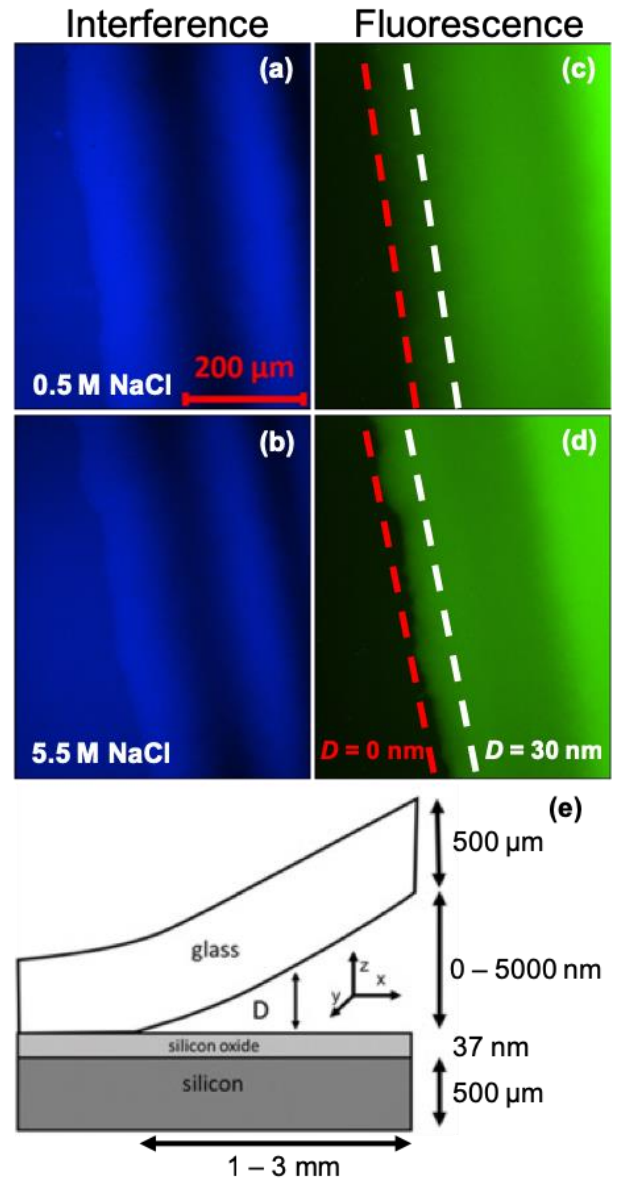


Figure 2: (a) and (b) Interference ($\lambda = 445$ nm) and (c) and (d) fluorescence emission ($\lambda = 525$ nm) images of the thinnest section of the crack with the salt concentrations indicated. The dotted lines serve as an approximate guide to the eye for the $D = 0 - 30$ nm region, as determined from the interference image. Images have been colorized at the interference and emission wavelengths. (e) Schematic of the chip (not to scale). Note that z is the distance from the midplane of the thin film.

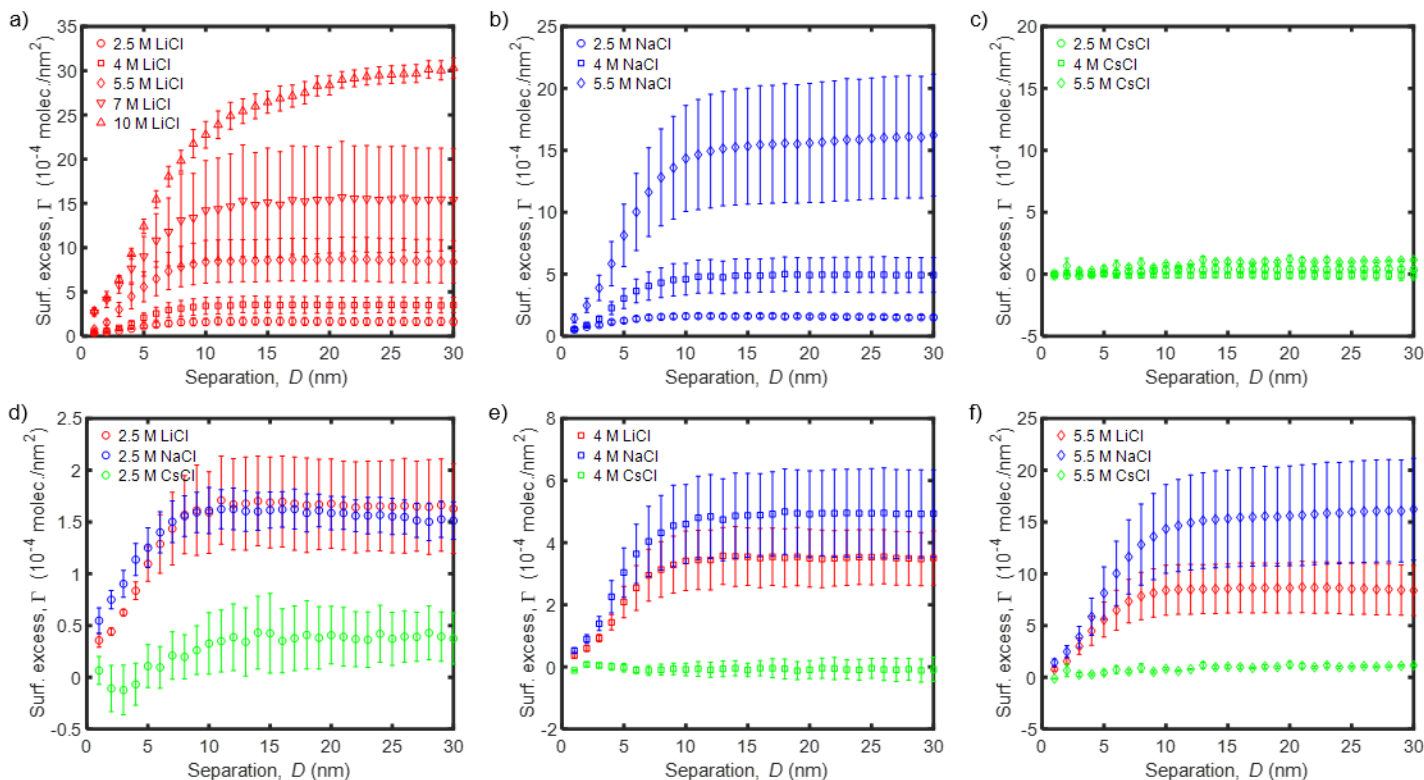


Figure 3. Surface excess of fluorescein as a function of separation (aqueous film thickness) for various salt concentrations and salt cations. The top row (a – c) shows the effect of salt concentration and the bottom row (d – f) shows the effect of salt type at a constant salt concentration. Error bars are the \pm standard error of measurements for three to four replicates; examples of replicates are shown in the supporting information. For the 10 M LiCl solution, the results are consistent with a large amount of fluorescein very near the two solid-liquid walls.

In the absence of a long-range field extending from the solid-liquid interface, the gradient in surface excess should decay over a very small distance. The long-range decay of the surface excess indicates that there is a long-range field, in direct conflict with the Debye result in Eq. 1. A second result is that the surface excess of fluorescein is positive in LiCl and NaCl solutions and that the surface excess grows with increasing salt concentration. Recalling that both silica and fluorescein are negatively charged in water or dilute salt solution, this indicates charge reversal. This charge reversal by a monovalent salt also conflicts with the PB assumption that the ions experience only a local field, and will be considered later. In contrast there is at most a very small surface excess of CsCl, and our resolution of the decay is poor in this salt. The results suggest that there is only a small magnitude of surface potential in the CsCl solutions. The CsCl results will not be considered further.

Quantification of the Decay-Length in Concentrated Salt Solution

Our principal objective is to use an independent technique to verify or contradict the conclusion from surface forces experiments that the electric field decays slowly (i.e. does not follow the Debye-Hückel result of Eq. 1). Surface forces measurements reveal a long-range decay in the surface force. The interpretation is that the force is a double-layer force and that it decays exponentially with a decay length characteristic of the electrical potential. The surface excess measured here, in contrast, increases up to a plateau value. To quantify this increase, we use the following empirical equation:

$$\Gamma(D) = \Gamma_{\infty}(1 - \exp(-D/\kappa_E^{-1})). \quad (4)$$

The two fitting parameters are Γ_∞ , the surface excess of two solid–liquid interfaces at large separation, and κ_E^{-1} , the empirical decay length of the surface excess. The decay lengths indicated in Fig. 4 for NaCl and LiCl are all in the range 3–10 nm, and they increase with salt concentration. These results are inconsistent with the PB result of Eq. 1; if the decay followed Eq. 1, then all values would be < 1 nm and the decay length would diminish with salt concentration. Note that the decay lengths previously measured for dilute (< 0.5 M) salt solutions were consistent with PB theory, i.e. decreasing decay with increasing salt concentration.¹⁰⁹ These results together show that the decay length is a minimum at or around 0.5 M.

Model-Dependent Decay-Length. To proceed further, we need to make a model for the potential. From here we (a) assume the potential acting on the fluorescein is electrostatic in origin, and further (b) use PB theory *but with an experimentally-fitted decay length*, rather than the Debye-length. This is consistent with Kjellander’s result that the potential at large separation decays exponentially if correlations are considered (Eq. 2). In this semi-empirical approach, the object screening the electric field is not necessarily the ions considered in PB theory, but an equivalent combination of concentration and effective charge.

The PB equation is:

$$\frac{d^2\psi}{dz^2} = -\frac{1}{\varepsilon\varepsilon_0} \sum z_i e c_{b,i} \exp\left(-\frac{z_i e \psi(z)}{kT}\right) \quad (5)$$

All solutions to the PB equation do not contain a uniform decay length. For low potentials ($|\psi(z)| < \frac{kT}{ze} \approx 25$ mV for 1:1 electrolyte), an analytic solution for symmetrical, constant surface potential, ψ_0 , boundary condition for a $z:z$ electrolyte does explicitly contain the Debye length:

$$\psi(z) = \frac{\psi_0 \cosh(-\kappa_F z)}{\cosh\left(-\frac{\kappa_F D}{2}\right)}, \quad (6)$$

where z is the distance from the midplane of the aqueous film, and $\kappa_F^{-1} = \kappa_D^{-1}$ for these conditions. Note that even in this case, κ_F^{-1} is not strictly the decay length of the potential, because the potential does not decay exponentially when the film is confined between two interfaces (it is a cosh function), but we will still refer to the scaling factor for z as “the decay length”. In our work we will treat κ_F^{-1} as a fitting parameter obtained from Eq. 6. In some sense, Eq. 6 is simply a convenient functional form for fitting a decay-length that was inspired from and does limit to the PB solution for dilute electrolytes and low potentials. We have used the subscript F as a reminder that this is a parameter fitted from Eq. 6 for concentrated solutions, not the Debye-length that is calculated from Eq. 1.

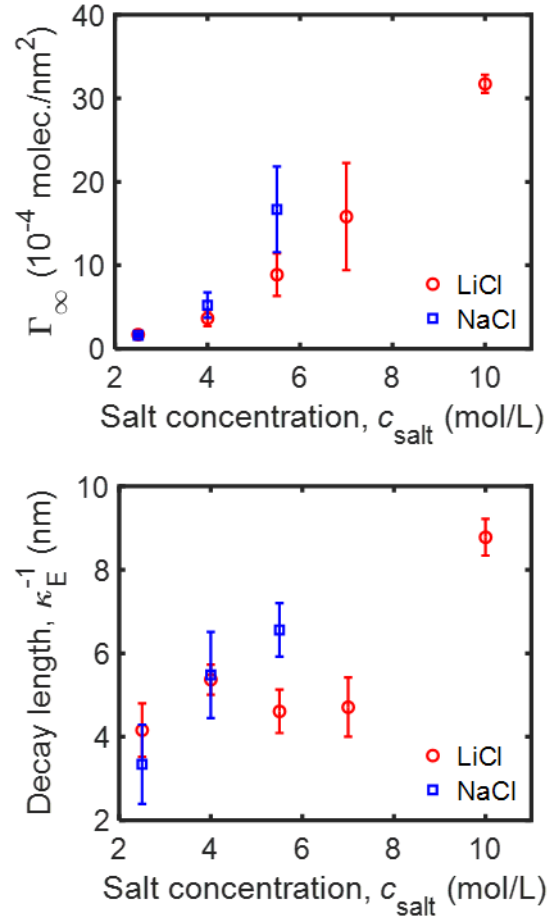


Figure 4. Surface excess of the isolated solid–liquid interfaces and empirical decay lengths and as a function of salt concentration obtained from Eq. 4.

The concentration at any position between the plates can be calculated from the Boltzmann distribution. Again, assuming that the potential is entirely electrostatic, the concentration is:

$$c(z) = c_b \exp\left(-\frac{Ze\psi(z)}{k_B T}\right), \quad (7)$$

where $Z = -2$ for fluorescein at pH 9.4.

The surface excess of adsorption at a given separation is then:

$$\Gamma(D) = \int_{-D/2}^{D/2} c_{b,Fl} \exp\left(-\frac{Ze\psi(z)}{k_B T}\right) - c_{b,Fl} D \, dz. \quad (8)$$

The surface excess data over the range of 0 – 30 nm was fitted to equations 6–8 to determine ψ_0 and κ_F . The fitted values for κ_F^{-1} are shown in Fig 5.

Our results are qualitatively consistent with surface forces measurements, but the decay lengths for NaCl are not quantitatively the same as the decay length of the surface forces obtained by Smith et al,⁹³ albeit for different solid–liquid interfaces. This decay length is also ion specific, with Na^+ showing a greater change in the decay length than Li^+ over the concentration range from 2.5 – 5.5 M.

We conclude the results with a few minor points. A few of the fitted potentials (for the 5.5–10 M solutions) were greater than 25 mV (Fig. S7), which violates an assumption of Eq. 6. As a check we refitted all conditions but with an exact numerical solution to the PB equation. Since that solution does not have an explicit decay length, we fitted the concentration, and converted that to an effective decay length using Eq 1. The difference in fitted decay length for the low potential and exact solution are very small and not important to the conclusions. The important point is that the fitted decay length increases with concentration.

We also note that a constant charge boundary condition was not used here because the constant charge boundary condition causes the concentration of counterions in a very thin film to rise precipitously (see Supporting Information, Fig. S4), which was not observed experimentally (Fig. 3). Measurement of surface excess is very good for distinguishing the constant charge from the constant potential boundary condition because the ion densities have qualitatively different dependence on D : at constant potential, the surface excess decreases with smaller separation whereas at constant charge the surface excess increases.

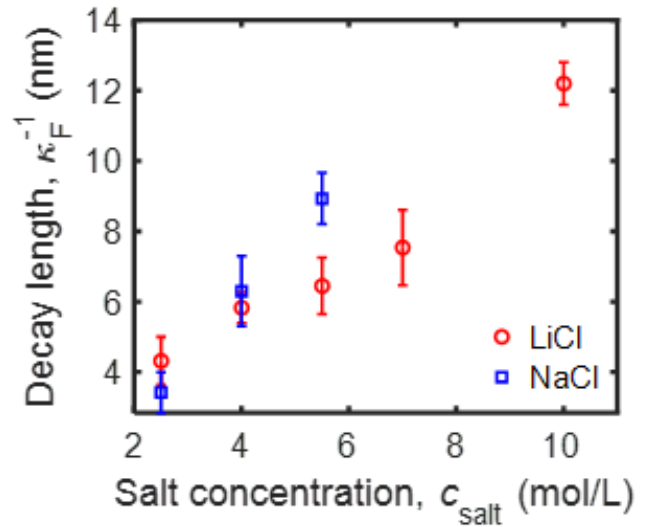


Figure 5. Decay length of the potential obtained from fits to the Poisson-Boltzmann equation (Eq. 6) assuming low potential and constant surface potential, and that the decay length is a fitting parameter, rather than obtained from Eq. 1.

DISCUSSION

The Decay Length. Lee et al. have developed a scaling argument that suggests that the decay length in concentrated salt solution should scale as:⁹⁶

$$\kappa_L^{-1} \sim l_B c_b a^3, \quad (9)$$

where l_B is the Bjerrum length of the solution:

$$l_B = \frac{e^2}{4\pi\epsilon_0\epsilon_r kT} \quad (10)$$

and a is the ion diameter. Lee et al. give a physical interpretation of this scaling starting with a neutral salt lattice that would not screen the potential, but adding charge defects due to water molecules and the finite temperature that leads to screening of the potential. The defect concentration scales with the solvent (water) concentration and inversely with the salt concentration, so the screening is less for more concentrated solutions. For both simple salts and ionic liquids, they find that the decay lengths obtained from surface forces measurements have the appropriate scaling given in Eq. 9.⁹⁶ Substituting Eq. 10 into 9:

$$\kappa_L^{-1} \sim c_b \epsilon_r^{-1} T a^3. \quad (11)$$

There is considerable variation of ϵ_r across the range of salt concentrations that we use, so we have examined the effect of $c_b \epsilon_r^{-1}$ at a fixed temperature. For each individual salt (fixed a), Fig. 6 indicates that $\kappa_L^{-1} \sim c_b \epsilon_r^{-1}$ as predicted by Lee et al.⁹⁶ The larger ion, Na^+ has a greater slope than the smaller ion, Li^+ , qualitatively in agreement with Eq. 11. Quantitatively, $(a_{\text{Na}^+}/a_{\text{Li}^+})^3 \approx 2.1$ and $(a_{\text{NaCl}}/a_{\text{LiCl}})^3 \approx 1.3$, whereas the ratio of slopes is about 5, so the ion size-dependence is not in quantitative agreement. Recall that the surface excess of Cs^+ was too low to enable us to measure the decay-length.

The original model proposed by Gebbie et al.⁸⁸ to explain anomalous decay was based on the assumption that the ions are not fully dissociated in confined concentrated electrolytes, such that the vast majority of ions are in net-neutral ion-pairs that do not contribute to screening. According to this model, the screening by dissociated ions only would be given by

$$\kappa_G^{-1} = \frac{1}{\sqrt{\alpha}} \kappa_D^{-1}, \quad (12)$$

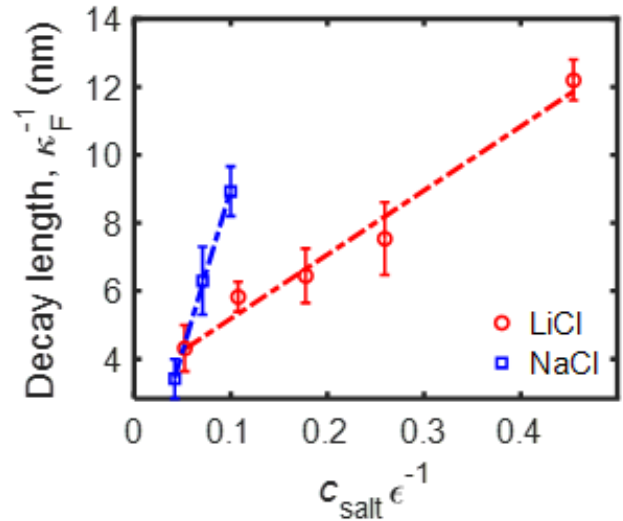


Figure 6. Test of the scaling relationship of Lee et al.⁹⁶ (Eq. 11) to the decay-lengths obtained from PB-fits to surface excess measurements (Fig. 6). The lines are least squared fits to the data for each ion, and have R^2 values of 0.98 for Li^+ and 0.99 for Na^+ .

where α is the degree of dissociation. Fig 8 shows values of α that were obtained from fits to our measured decay lengths. The fitted fraction of putative dissociation drops approximately exponentially with salt concentration from about 10^{-3} to 10^{-5} for salt concentrations from 2.5 to 10 M.

It is not clear why a simple ion pair would associate, or change in degree of association by so much over this concentration range, and Kjellander's explanation of charge correlation and Lee et al's scaling model seem more reasonable explanations. In addition, our fluorescence measurements provide evidence against the ion association hypothesis for LiCl and NaCl. It is well known that the emission intensity of fluorescein depends strongly on the degree of dissociation: when the anion is neutralized with two H^+ cations, the fluorescence is much weaker than when it is dianionic.¹¹² It seems very likely that the fluorescence would also be diminished by neutralization with two Na^+ ions. Yet, when we measure the fluorescence in bulk, we find only a very weak dependence of the emission intensity as a function of salt concentration — a drop of about 7% in the range 2.5–5.5 M compared to a 0.5 M solution, and only minor change in the shape of the spectrum (Fig S1), indicating only a very small effect of ionic strength on the dissociation of fluorescein in bulk. Likewise, in the thinnest part of the crack, the ion-association hypothesis suggests a $\sim 10^3 - 10^5$ reduction in dissociated salt (Fig. 7). If the high salt concentration also caused an association of fluorescein with its protons, there would be a huge reduction in fluorescence, whereas we observe very intense fluorescence in the thin film containing concentrated salt. Thus, our fluorescence measurements appear to contradict the association hypothesis.

Charge Reversal. The PB model is a mean field theory, so it does not consider charge-charge correlations, and in our implementation does not consider ion size effects or density oscillations. Theoretical studies and modelling that do consider charge correlations and finite ion sizes do predict more complex surface structures including overscreening of surface charge at low surface potential and crowding of ions at high surface potential for single interfaces.^{113, 114} Although interpretation of the surface charge and surface potentials obtained from the PB fit is limited by the simplicity of the theory, it is still interesting to examine the sign and magnitude of the PB fits for the charge that we obtain from the fluorescein ion profile.

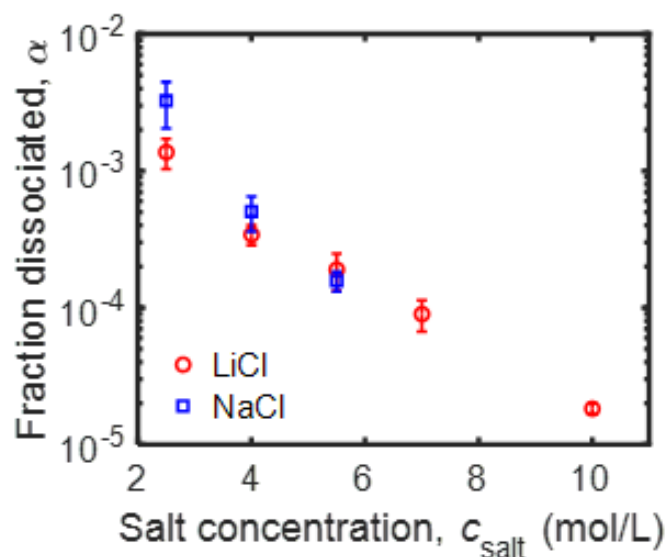


Figure 7. Effective fraction of ions dissociated as a function of salt concentration. The fraction of ions was determined from the decay length obtained in our work (Fig. 6) and Eq. 12. The error bars are the standard error from fits to experimental replicates.

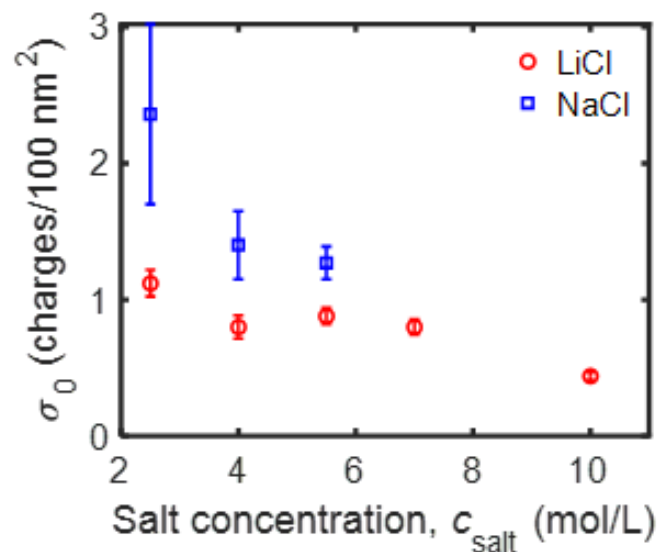


Figure 8. Surface charge density at infinite separation obtained from fits to Eq. 6. The error bars are the standard error from fits to experimental replicates.

Surface force measurements do not directly determine the sign of the surface potential or charge. Electro-osmotic measurements can assess the surface charge based on the mobile charge, but the charge depends on the location of the shear plane. Our measurements of amount can, in contrast, be used to determine the sign of surface charge. If there is an excess of an anionic fluorescein in the diffuse double layer, then the surface charge is positive. Here we observe that the surface excess of fluorescein is positive in concentrated LiCl and NaCl solutions, therefore either the fluorescein has reversed charge or the silica has reversed charge. By silica, we are including whatever layers of cations that are adsorbed to reverse the charge. For reasons outlined above, we consider it very unlikely that the fluorescein has reversed charge by addition of three cations or some protons and cations (that would change its fluorescence emission) so we conclude the silica surface is positively charged in very concentrated NaCl or LiCl solutions.

We are unaware of any prior experimental work showing charge reversal arising from addition of monovalent salt. Van der Haydon *et al.* used electrophoretic measurements to conclude that charge reversal of silica did not occur for monovalent ions up to concentrations up to 0.15 M,¹¹¹ which is much lower than the concentrations that are considered here. Previously Qiao and Aluru have used simulations to show that non-electrostatic contributions to the water-cation interaction can lead to charge reversal.¹¹⁰ These non-electrostatic interactions in the simulation lead to overcompensation of the surface charge in the first layer of cations near an anionic solid.

The surface charge density at infinite separation fitted from solution of the PB equation is shown in Fig 8. Approximately 0.005 – 0.025 charges per nm² are required to explain the observed fluorescein surface excess. Considering that the separation between ions in bulk solution is only on the order of 1 nm (Table 1), this is only a small perturbation of the bulk ion density and may simply be a consequence of where the Stern layer plane is considered to be, or may be due to overscreening of the silica surface charge.

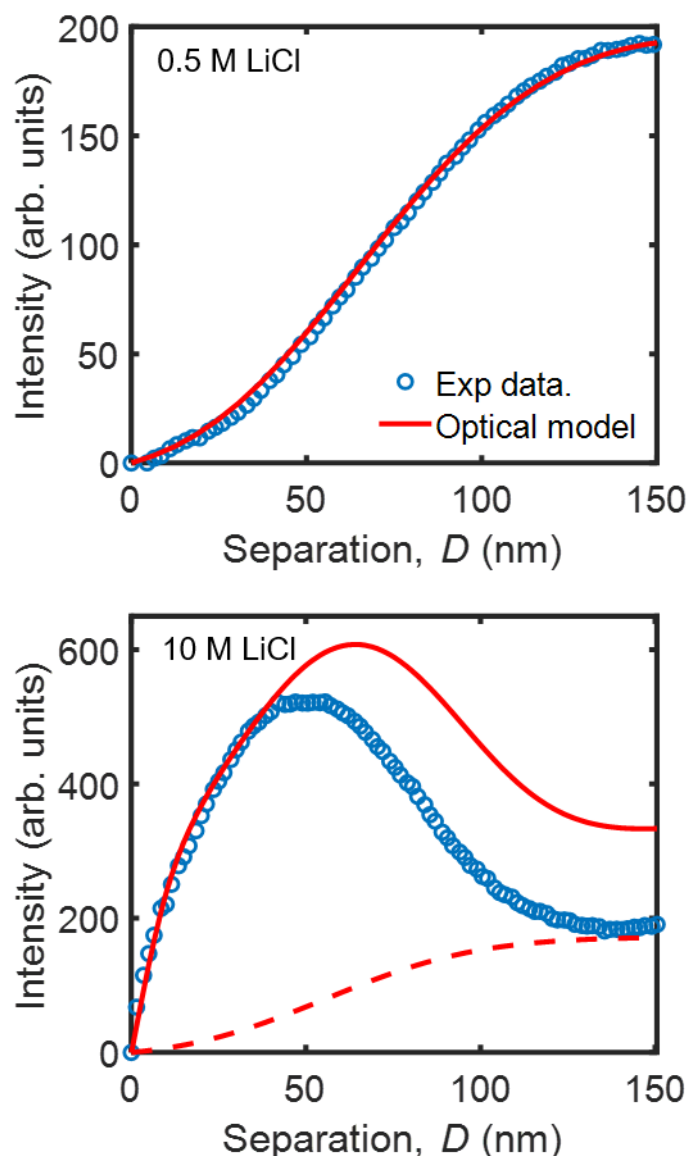


Figure 9. Comparison of measured fluorescence intensity and optical model of intensity. For a 0.5 M LiCl, the model is for a uniform distribution of molecules, and has been multiplied by an arbitrary constant to fit the measurements in the range 10–150 nm. The close correspondence between model and data supports the idea that the molecules are uniformly distributed in the 0.5 M NaCl, even for $D = 0–30$ nm. (see also Fig S9). For 10 M LiCl, two models are shown: (1) a uniform distribution represented by the dashed line and (2) the distribution calculated from the potential obtained from fit of the experimental data to the solution to the PB equation for a range of 0 – 30 nm assuming constant symmetrical potential.

Comparison of Optical Model and Experiment for Thick Films. Thus far, we have only considered results from films that are 0–30 nm thick. The advantage of this range is that the emission per molecule is independent of the distribution of molecules, which is ideal for determining the surface excess. For thicker films, however, the fluorescence emission does depend on the molecular distribution (See Fig S8), which provides an opportunity to examine whether the distribution determined from the thin film data and the PB equation is similar to that observed in thicker films. We have established a fitted surface potential and decay length from data in the 0–30 nm film thickness. If we assume that the decay length and potential are the same in thicker films, we can model the intensity–film-thickness profile for large film thickness. We have again assumed in the model that the potential is symmetric. Fig. 10 shows the measured and modelled fluorescein intensity for 0–150 nm thick film. We first show the data for 0.5 M LiCl where the optical model¹⁰⁹ has been multiplied by a constant – the intensity per molecule – to best fit the data. For 0.5 M LiCl, a model of uniform distribution fits the data very well, and justifies our use of the 0.5 M solution to calibrate the intensity per fluorophore. Also, the uniform distribution model fits the data in the 0–30 nm region, supporting our assumption that the decay length of the field is very short in 0.5 M solutions. See also Fig. S9 for an enlarged view of the fluorescein surface density in the thin film region.

The measured profile for 10 M LiCl is very different than for 0.5 M (Fig 9). There is (a) a distinct maximum and minimum that is absent for the intensity profile of the homogeneous solution, and (b) a much larger intensity. We have compared the data to two models: uniform distribution and the distribution arising from the PB equation with the surface potential and decay length and potential for the 0–30 nm data only. The intensity per molecule was calibrated from the 0.5 M solution. The optical model of a uniform distribution has the wrong magnitude and the wrong shape. The model of the PB distribution with a long decay length (12 nm) and charge reversal produces the overall magnitude and shape. This provides further support for the idea that the decay length is long and the charge is reversed. It is also possible to qualitatively assess the effect of relaxing some restrictions to the PB model. If the decay length of the potential were to diminish with greater film thickness or charge regulation was allowed, then the PB model result would move toward the uniform model and provide a better fit to the data at large film thicknesses. The effect of allowing asymmetric potentials is more complex and is considered in Fig. S10.

CONCLUSIONS

Measurements of the density of ions in a thin film of very concentrated salt solution between two silica surfaces are consistent with a very long-ranged decay (4–13 nm) of the electrical potential in concentrated salt solution. Consistent with surface force measurements, the decay is much longer than expected from the Debye-length derived from Poisson-Boltzmann theory, and the decay increases with salt concentration, rather than decreases with salt concentration. The decay depends on the type of salt (Li^+ vs Na^+), and the decay length scales with $c_b \epsilon_r^{-1}$ as predicted by Lee et al.⁹⁶ Furthermore, our ion-density measurements demonstrate that the surface charge of silica is reversed by addition of very concentrated monovalent salt. These measurements provide independent support, directly from the ion density rather than from force measurements, that the decay of the electrostatic potential is long-ranged in concentrated salt solution.

SUPPORTING INFORMATION

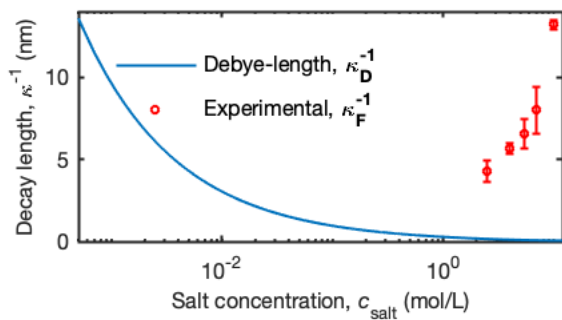
The supporting information contains:

- Table of measured refractive indices of concentrated salt solutions
- Measurements of the fluorescence emission of fluorescein in concentrated salt solution
- Modelling of the effect of the fluorophore distribution on the emission in a thin film
- Examination of the uncertainty when fitting an empirical Decay-length to surface excess measurements.
- Examination of the uncertainty when fitting the Decay-length to surface excess measurements using the Poisson-Boltzmann equation for constant potential and constant charge boundary condition
- Comparison of the low-potential analytical solution to the numerical solution of the Poisson-Boltzmann equation for symmetrical constant surface potential boundary condition
- Surface potentials obtained from a fit of surface excess data to the Poisson-Boltzmann equation
- Optical modeling of the intensities
- Area density of fluorescein for the 0.5 M LiCl solution
- Effect of asymmetry on the fit of the decay length

ACKNOWLEDGMENTS

WAD thanks Professor Vincent Craig and the Australian National University for hosting him on sabbatical where some of this work was developed. The authors thank Professor Richey Davis and Professor Preston Durrill for the use of their refractometer to measure the data in Table S1. We also thank Bryan Curtin and Jared Arkfeld for their assistance performing measurements of the refractive index of concentrated salt solutions.

TABLE OF CONTENTS GRAPHIC



Chapter 4: Symmetrical glass–glass based CAA

1. Motivation

The majority of the work described in the previous chapters was conducted using asymmetrical interfaces of glass and thermal oxide grown on silicon. These two surfaces are very similar, but not identical. The glass contains boron, aluminum and sodium cations whereas the thermal oxide does not. For ease of differentiation, that system will be referred to as silica-glass.

There are two major drawbacks of using such a system

1. The slight asymmetric nature of the interfaces means that the boundary conditions at either surface are not symmetric– we made that assumption when fitting of the decay-lengths in Chapter 3. The effect of asymmetric potentials on one set of data is shown in Fig S10 in Appendix B.
2. For the optical modelling in Chapters 2 and 3, we assumed that the excitation intensity was an odd function around the midplane and that the concentration profile was an even function. The odd approximation was never true, but sufficiently precise for $D < 50$ nm when we optimized the oxide thickness. The even approximation for the concentration profile was only true if the glass were the same as the thermal oxide. We know that they are similar but do not know how similar.

In order to overcome these limitations, I was motivated to developed a symmetrical system and I chose to use two glass wafers.

The main advantages of a symmetric glass-glass system are

1. The interfaces are symmetrical as they are made of identical materials. For modelling, this satisfies the assumption that the interfaces have identical charging characteristics.
2. The lack of a highly reflective interface (the silicon-oxide interface) present in the earlier iteration of the device means there is less interference. Measurements can be performed in relatively thick and thin films whereas previously we were only limited to thin films
3. The ability to measure thick films means that the measurements can be done on films that are so thick that they are essentially all bulk. In this case calibration for the intensity per molecule can be done on the experimental sample; there is no requirement for an additional reference chip.

Specific details on the development of a glass-glass chip are provided in Appendix C

2. Optical Modeling

Fig 1. compares the intensity per molecule for fluorescein calculated using the optical model for a silica-glass based CAA and a Glass-Glass based CAA. The optical modeling shows that regardless of separation, the effect of interference on the intensity per molecule is quite small in glass-glass systems compared to silica-glass based systems. Depending on the position of the fluorophore, in the asymmetric silica-glass system, the variation in intensity can be up to 20 times, whereas in the symmetric system the variation is over an order of magnitude less.

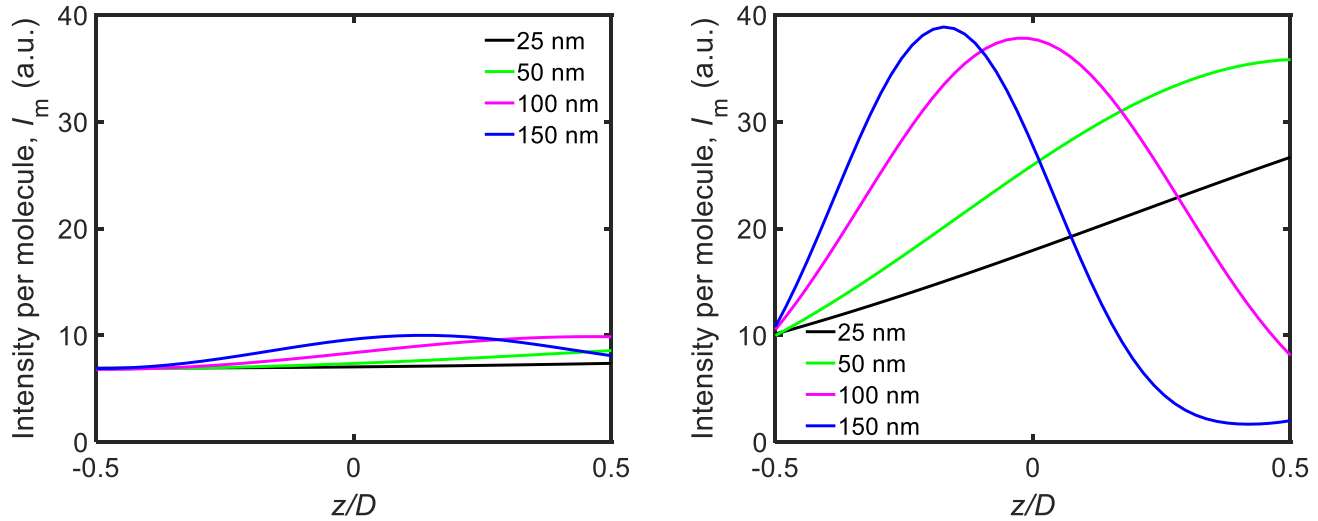


Figure 1: Intensity per molecule I_m as a function of z and D position for films of various thicknesses. Left – Intensity per molecule as a function of z and D in symmetric glass-glass systems. Right – Intensity per molecule as a function of z and D in asymmetric silica-glass systems.

Theoretical intensities can also be calculated for various concentration profiles. Fig 2. shows the n/A and corresponding total measured intensity, I_T for the different types of adsorption detailed in this thesis. While both systems, glass-glass and silica-glass show non-linear variation in the total intensity as a function of film thickness, the oscillations are far smaller in glass-glass systems owing to the minimal interference and look quite similar to the n/A profile. In cases of positive adsorption the variation in I_m in the film exacerbates the problem considerably in silica-glass systems resulting in highly non-monotonic changes in total measured intensity as a function of separation.

Absent any interference, the average intensity per molecule, $I_{M,Ave}$, can be determined in a fairly straightforward manner by using intensity data in very thick films (for example: 300 nm – 1 μ m) via,

$$I_{T,thick\ films}(D) = I_{M,Ave}(c_{bulk}D + \Gamma_{\infty}) \quad (14)$$

in the limit of large separation where Γ_{∞} is the surface excess at large separation i.e. the surface excess when the molecular distribution is sensitive only to one interface and is not influenced by the presence of a second interface. To determine $I_{M,Ave}$, one simply needs to perform a linear fit to the intensity-separation data at large separations i.e. in thick films. For example, in an electrolyte, one would use intensity data $> 5\kappa_D^{-1}$ to perform the linear fit. As $c_{bulk}D$ is known and the surface excess at infinite separation, Γ_{∞} , is invariant with separation when the interfaces are sufficiently far apart and non-interacting, $I_{M,Ave}$ is simply the slope of

linear fit and $I_{M,Ave}\Gamma_{\infty}$ is the intercept. Once the average intensity per molecule is known the number of molecules per area in a thin film can be easily calculated,

$$\left(\frac{n}{A}(D)\right)_{\text{film}} = \frac{I_{T,\text{thin films}}(D)}{I_{M,Ave}} \quad (14)$$

From Figure 2, it can be seen that the above methodology would work poorly in silica-glass systems, owing to the highly non-linear and oscillatory intensity as a function of separation. In glass-glass systems, the oscillations are relatively slight incurring minimal error.

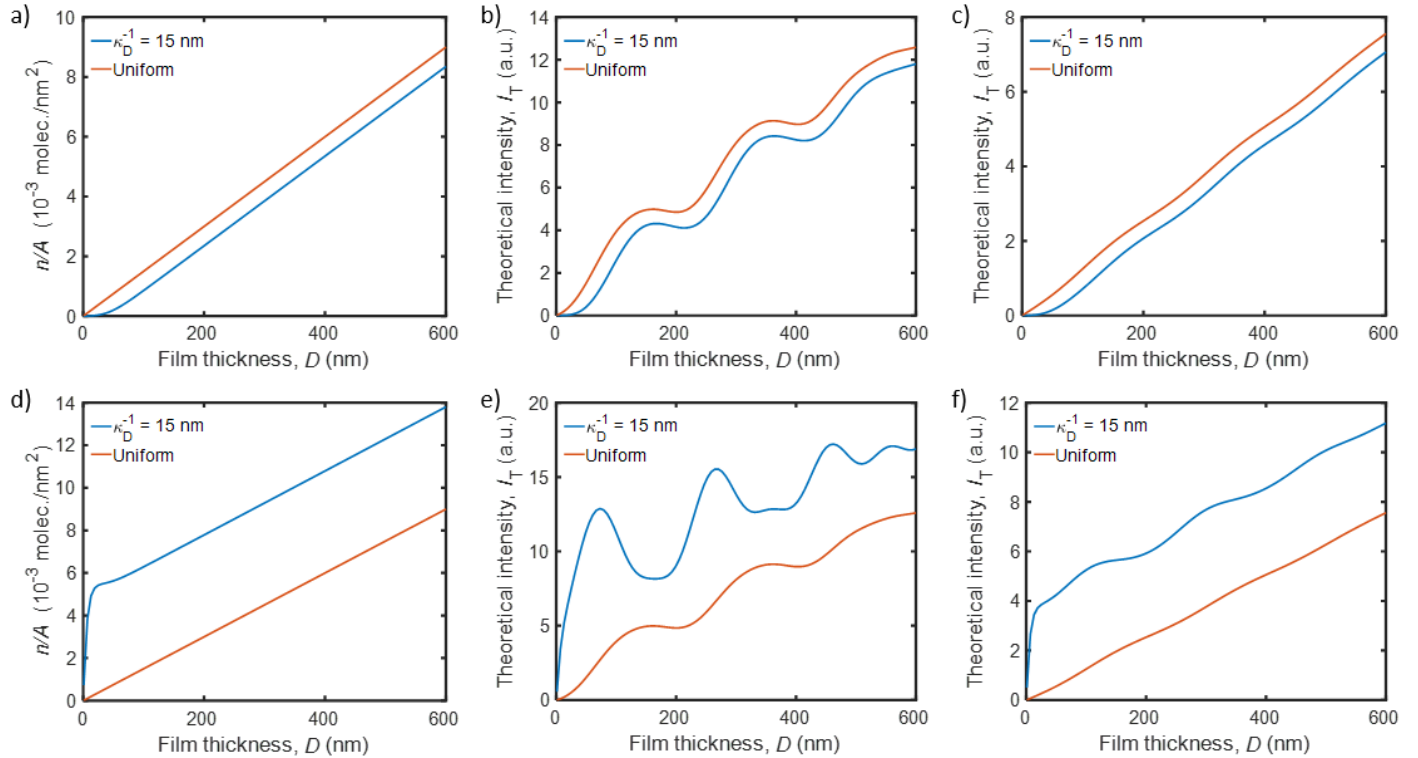


Figure 2: Calculated theoretical fluorescence emissions for ions in a thin film. The first column is the surface excess calculated from PB an ion with charge $\pm 2e$ for a constant symmetrical surface potential of $\psi_0 = 50$ mV with a 15 nm Debye-length. The second column is for the fluorescence emission for silicon-glass and the third column is for glass-glass. The top row is for co-ions and the bottom row is for counterions. Note that the intensity oscillations are much smaller for the glass-glass system.

3. Results

Figure 3 shows interference and fluorescence images for a glass-glass chip infused with fluorescein with a short Debye length. The interference is fairly weak as a result of low refractive index contrast at the glass-water interface ($n_{\text{glass}} = 1.47$ and $n_{\text{water}} = 1.33$). Qualitatively, the fluorescence image shows the correct trend; as the separation increases from the left to the right of image, so too does the fluorescent intensity as the number of molecules per area scales linearly with film thickness.

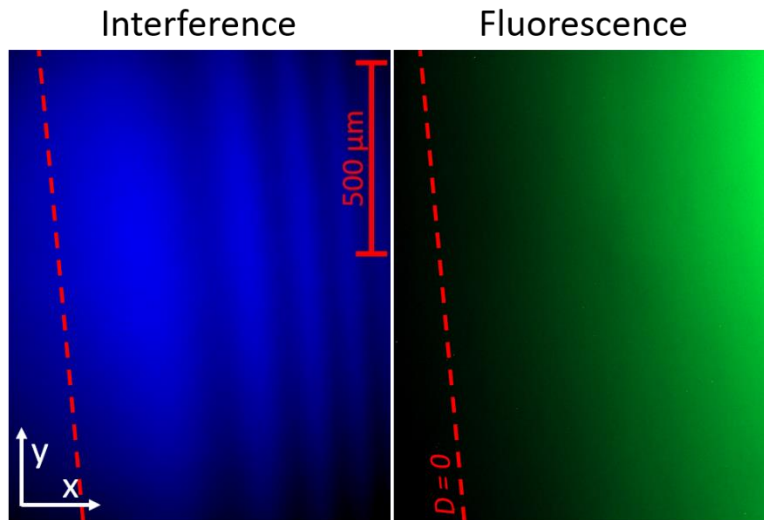


Figure 3: Interference (445 nm) and fluorescence images (Ex: 475 nm, Em: 525 nm) for a glass-glass chip infused with a solution where the fluorescein concentration is 50 μM and a Debye-length is 0.5 nm taken with a 10x objectives. The red dotted line represents separations to the left of which are 0 nm as the two glass surfaces are bonded together and to the right of which the intensity is increasing monotonically as a function of film thickness.

Figure 4 shows that the experimental fluorescent intensity is a linear function of film thickness for a uniformly distributed fluorophore. This is in contrast to silica-glass (see Chapter 2 Fig 3) which oscillates significantly as a function of film thickness.

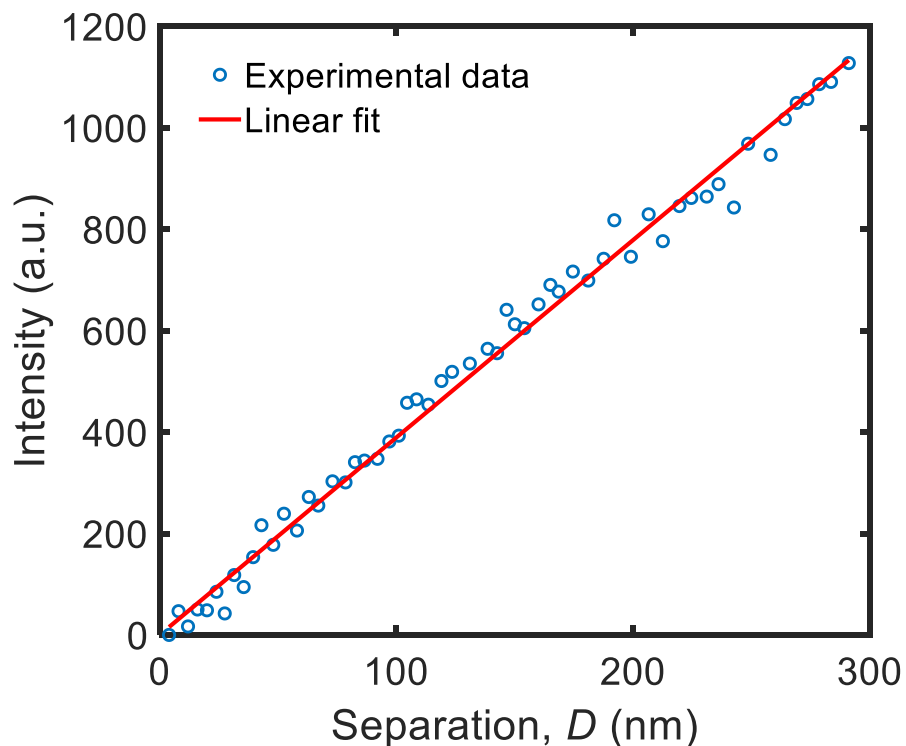


Figure 4: Intensity as a function of separation for a glass-glass chip infused with an aqueous fluorescein solution ($c_{FI} = 50 \mu\text{M}$ and $\kappa_D^{-1} = 0.5 \text{ nm}$). The linear fit to the data is performed from 20 – 300 nm. The R^2 value of the fit is 0.99.

4. Discussion

The work presented here is preliminary but promising. One problem that remains to be solved is getting an accurate separation profile as a function of pixel index in the glass-glass images. In silica-glass systems, while the large interference served as a strength for measuring the film thickness, yet was a weakness for measuring the number of molecules per area in silica-glass chips, the inverse is true for glass-glass. The weak interference results in a significant amount of noise in the interference image which makes it hard to measure the separation accurately. This can be resolved by using a laser to perform the interference microscopy as the primary reason for the poor signal to noise is the incoherent nature of the light source. The incoherence means that only few waves are in phase enough to produce an interference signal. Using a monochromatic, coherent light source such as a laser should increase the contrast between the fringes and thus reduce noise in the interference images allowing measurement of separation with a greater degree of accuracy.

Glass-glass based chips can be used to study solutions with very long Debye-lengths and observe the equilibrium behavior of larger objects. When we were limited to measurements where the maximum film thickness was only 50 nm, we could only study particles that could fit into this film. Now we can study larger particles and longer-ranged forces. I am currently working on investigating the equilibrium adsorption behavior of negatively charged nanoparticles with a hydrodynamic radius of 12 nm to silica interfaces as a function of solution composition using glass-glass systems. We expect the nanoparticles to be highly depleted because of the large negative charge on the particle in addition to the size exclusion from the thinnest section of the crack. This necessitates a device that can measure the number of particles accurately at larger separations than silica-glass based chips.

Chapter 5: Future Work

In Chapter 2 – 4 I describe original work I conducted developing a technique that performs direct measurements of adsorption and in Chapter 4 I describes improvements I made to this technique by switching to a glass-glass based CAA and some preliminary experiments looking at the behavior of electrolytes in this system. In this Chapter, I would like to discuss applications of the technique.

1. *Measurement of diffusion as a function of Debye-length*

One of the experimentally interesting phenomena that I was unable to pursue during my time spent on this project was the time-scale of diffusion into the crack. It is not clear to me why we would need to wait a full day to allow for equilibration and diffusion into the confined channel especially in solutions with short Debye-lengths. The diffusion should be relatively rapid, but it is quite slow. It would be interesting to measure the diffusion coefficient as a function of separation and solution composition in confinement and this question is currently being examined by Zechen Zhang in our group

Diffusion of nanoparticles could also be measured using this technique.

2. *Viscosity measurements in concentrated polymer systems*

It is well known that the addition of polymers to a solvent, organic or otherwise can result in steep increases in the viscosity of the solution. In confinement as polymer begins to get excluded out of solution, one might expect that viscosity changes rapidly as a function of confinement in thin films of fluid.

This experiment would entail taking videos of a polymer solution as it traveled up the crack and measuring the change in intensity in the interference to tease out the fluid velocity and determine the viscosity of the liquid.

3. *Polyelectrolyte behavior in confinement*

Large polyelectrolytes have a rod-like conformation in solutions of long Debye-length and are globular in solutions of short Debye-length due to screening of electrostatic repulsion between the charged monomer groups.

If the polymer was sufficiently long, the effect of confinement on the extension properties of various polymer molecules could be studied as a function of confinement and solution composition

4. *Surfactant adsorption in confinement*

Our group has previously published a number of papers looking at the effect of confinement on surfactants. It would be interesting to use fluorescent surfactants and measure the adsorption profile in confinement.

Chapter 6: Conclusions

1. A technique was developed that can directly measure the static and dynamic behavior of molecules as a function of confinement and solution composition.
2. The surface excess of fluorescein, a di-anion in dilute electrolytes is primarily affected by electrostatics. The degree of depletion in thin films confined between negatively charged interfaces is a function of the separation and the Debye-length of the solution, and the experimental results were in semi-quantitative agreement with predictions from the Poisson-Boltzmann model.
3. In concentrated electrolytes (>2 M), the surface excess of fluorescein is a function of the ion-type and ion concentration. The charge on the interface is reversed and results are consistent with the hypothesis that the electrostatic screening length increases monotonically as a function of salt concentration.
4. A glass–glass sample was developed for the CAA. Because of the lower refractive index contrast, there is much weaker interference of the excitation, which allows surface excess measurements at separations much greater than 50 nm. Previously we assumed in the analysis, even at separations less than 50 nm that the fluorophore profile was symmetric. With the use of a symmetrical system (glass–glass rather than glass–silica) this is no longer an assumption. In addition, the use of a symmetrical system diminishes the number of fitting parameters that must be used in modeling.

Supporting Information for
Adsorption at confined interfaces

Prudhvidhar Gaddam[†], Robert Grayson[†], and William Ducker*

[†]these authors contributed equally to the paper

*For correspondence: wducker@vt.edu

Department of Chemical Engineering, Virginia Tech, Blacksburg, VA 24061, USA.

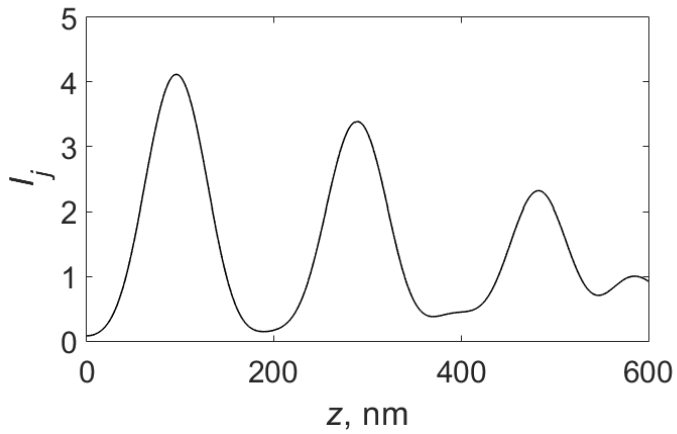
A. Interference Terms

The interference terms for the calculation of Eq 11 are:

$$\begin{aligned}
 \Psi_{in}^{\parallel,p} &= t_{54}^{\parallel,in} t_{43}^{\parallel,in} (1 - r^{\parallel,in} e^{i2pd}) / (1 - r^{\parallel,in} r_{34}^{\parallel,in} e^{i2p(d+\delta)}) \\
 \Psi_{in}^{\perp} &= t_{54}^{\perp,in} t_{43}^{\perp,in} (1 + r^{\perp,in} e^{i2pd}) / (1 - r^{\perp,in} r_{34}^{\perp,in} e^{i2p(d+\delta)}) \\
 \Psi_{in}^{\parallel,n} &= t_{54}^{\parallel,in} t_{43}^{\parallel,in} (1 + r^{\parallel,in} e^{i2pd}) / (1 - r^{\parallel,in} r_{34}^{\parallel,in} e^{i2p(d+\delta)}) \\
 \Psi_{out}^{\parallel,p} &= t_{45}^{\parallel,out} t_{34}^{\parallel,out} (1 - r^{\parallel,out} e^{i2qd}) / (1 - r^{\parallel,out} r_{34}^{\parallel,out} e^{i2q(d+\delta)}) \\
 \Psi_{out}^{\perp} &= t_{45}^{\perp,out} t_{34}^{\perp,out} (1 + r^{\perp,out} e^{i2qd}) / (1 - r^{\perp,out} r_{34}^{\perp,out} e^{i2q(d+\delta)}) \\
 \Psi_{out}^{\parallel,n} &= t_{45}^{\parallel,out} t_{34}^{\parallel,out} (1 + r^{\parallel,out} e^{i2qd}) / (1 - r^{\parallel,out} r_{34}^{\parallel,out} e^{i2q(d+\delta)}) \\
 p &= 2\pi n_3 / \lambda_{in} \cos \theta_3^{in} \\
 q &= 2\pi n_3 / \lambda_{out} \cos \theta_3^{out}, \quad (E1)
 \end{aligned}$$

where \parallel refers to parallel to the plane of incidence and \perp refers to perpendicular to the plane of incidence. The superscripts p and n denote parallel to the interface and normal to the interface, respectively. $t_{ij}^{\perp,in}$ is the Fresnel coefficient of transmission for an illuminating light wave crossing from the i^{th} to the j^{th} layer (Fig. 3) at an angle of incidence ϑ_i^{in} , and wavelength λ_{in} . Similarly the coefficient $r_{ij}^{\parallel,out}$ is the Fresnel coefficient of reflection for an emitted light wave crossing from the i^{th} to the j^{th} layer with an angle of incidence ϑ_i^{out} , and wavelength λ_{out} .

B. Figures



S1. Intensity of fluorescein fluorescence emission as a function of position within the crack, z , with $D = 600$ and $t = 0$. The interference is dominated by the silicon interface such that the shape of this curve is nearly invariant as D changes. For greater D the curve is extended along the horizontal axis; for smaller D reduced. For small t , the curve is shifted left by approximately t . If we wish to minimize changes in emission intensity as a function of z , it is best to have the fluid gap situated near a maximum or minimum. If we wish to minimize the z gradient of $I_j(z) + I_j(D - z)$, the fluid gap should be at an inflection point.

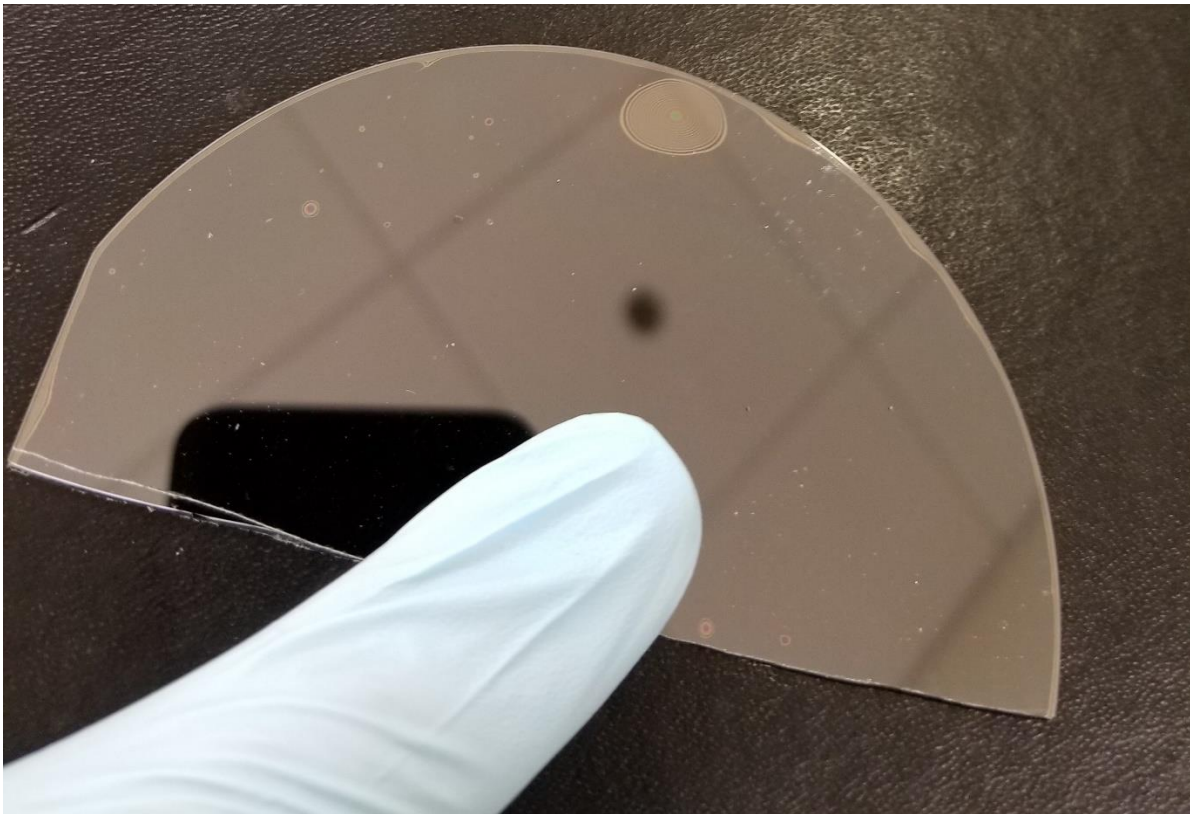


Fig. S2. Photograph of the dual wafer construct showing the radial crack around the perimeter. The light colored region around the perimeter is the region of the crack.

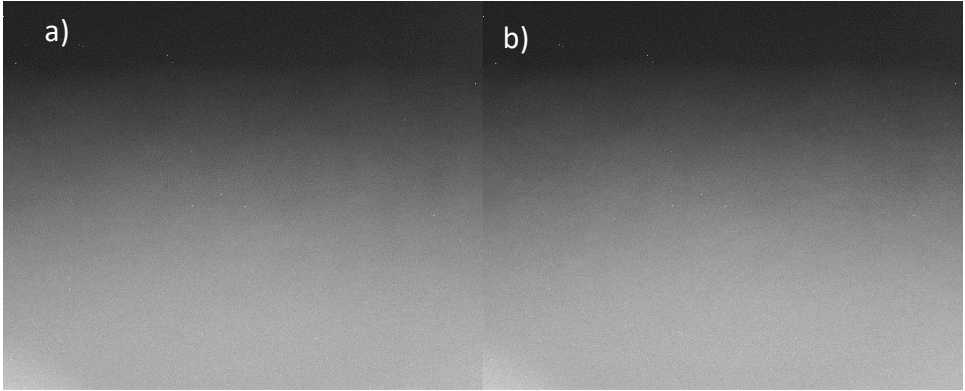


Fig. S3. Optical images of crack spaced 5 minutes apart in time. The lack of change in intensity is consistent with no change to the concentration of fluorescein in the thin film.

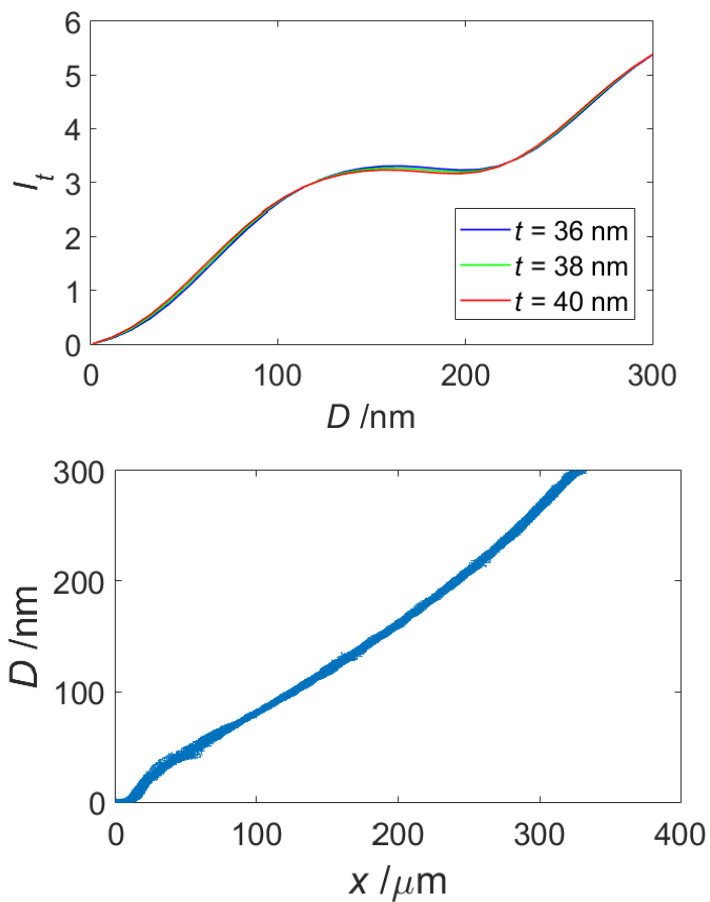


Fig. S4 Top: Intensity vs separation calculated from the model for various oxide thicknesses. Over this range of D , small variations in t cause small changes in the curvature of the I vs D curve. **Bottom:** Crack profile. Every pixel ($\sim 200,000$) where $D > 0$ is represented by a point in the figure. x is the distance perpendicular to a line fitted to the crack tip.

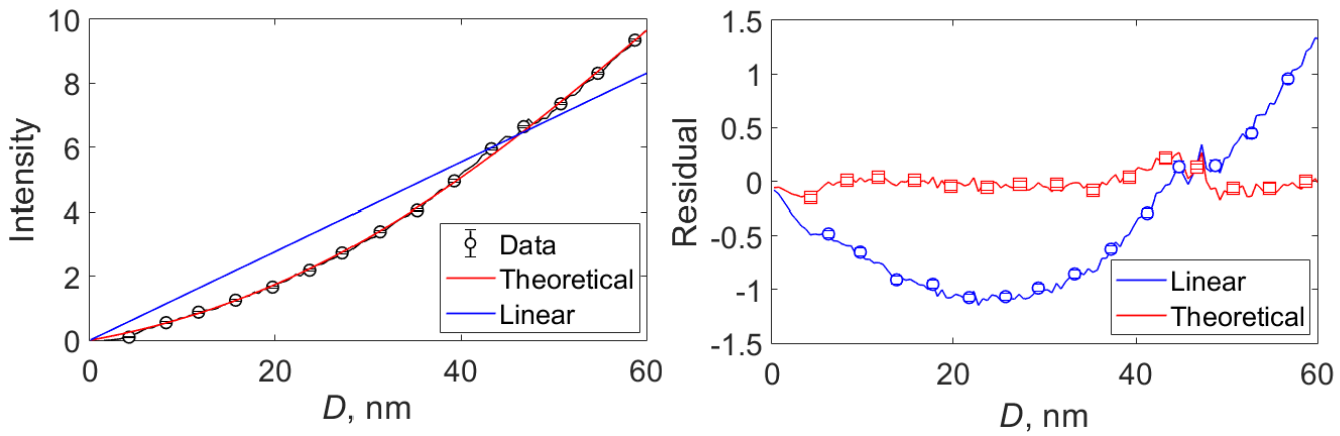


Fig S5.

Left: Fluorescence emission intensity over a range of 0–60 nm for $\kappa^{-1} = 0.50$ nm solution and a model assuming uniform molecular distribution. Plotted data are the average of intensities binned for a 0.5 nm range around each shown D . Error bars represent standard error of the same binned data. An oxide thickness of 36.8 nm was determined from interferometry of the sample, and used in the model. Two fits to the data are shown: (1) the optical model fit and (2) a linear fit. The optical model has one parameter, the magnitude, and the linear fit has a fitted slope with the fit restrained to pass through the origin. The range of the fit is $20 < D < 60$ nm. Right: Residuals for the optical model and the linear fit. The optical model agrees very well with the data, even for $D < 20$ nm. Clearly the optical model is a better fit, so the nonlinearity of I vs D is not negligible.

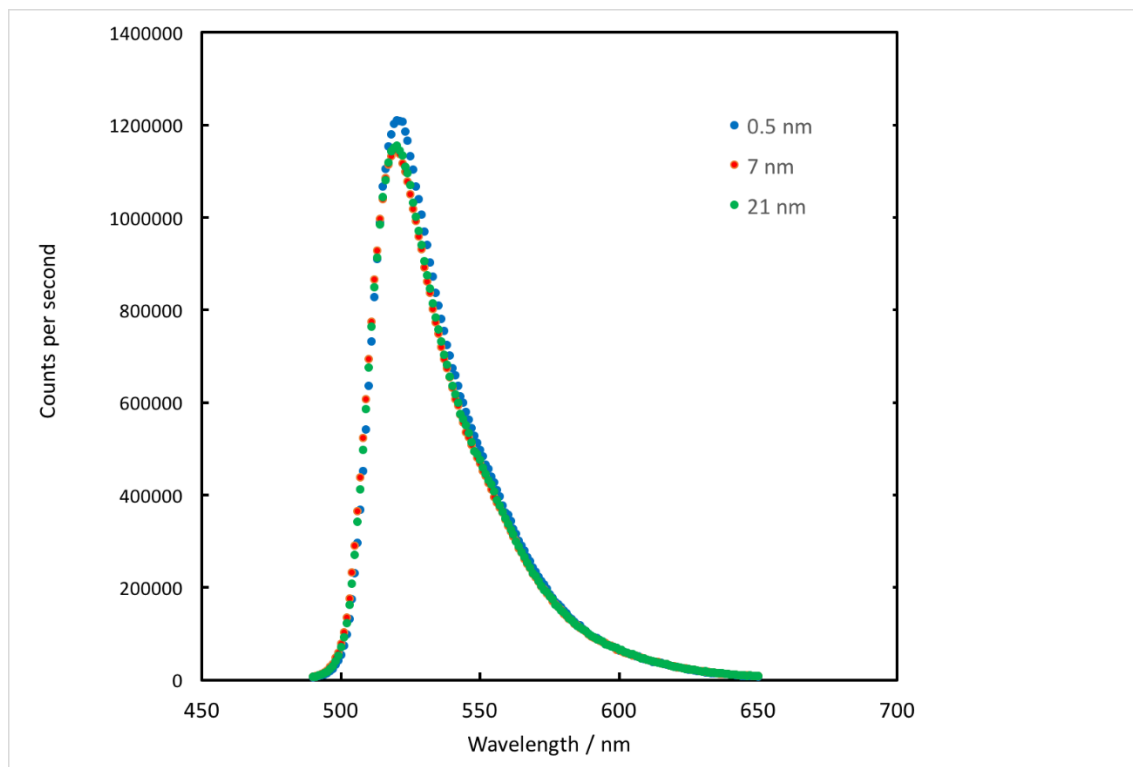


Fig. S6. Emission of 67 μm aqueous fluorescein solution as a function of Debye-length in NaCl solution. The emission filter range in the microscopy was 525 ± 25 nm. The integral over the range 500–550 nm deviates by 7% or less for 7 nm or 21 nm compared to the 0.5 nm solution and was not found significant in a Student's t-test.

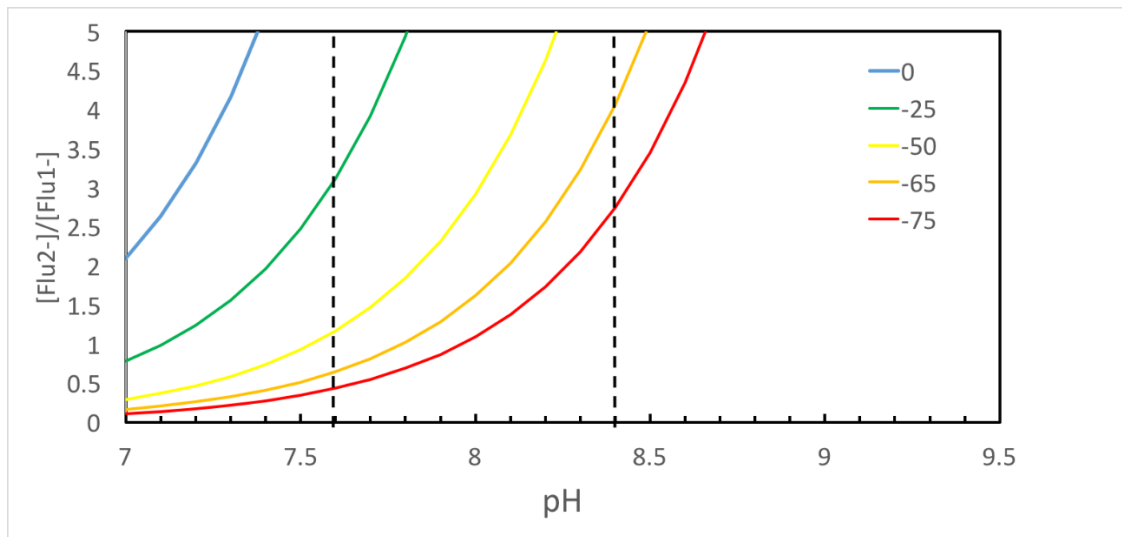


Fig. S7: Ratio of dianion to monoanion as a function of pH calculated from Eq 18 as a function of the potential. The calculation was done for $pK' = 6.68$, which is the activity-corrected pK for the $\kappa^{-1} = 14$ nm and 21 nm solution. The ratio increases slightly for shorter Debye-lengths.

E.g. at 50 mV, the ratio is given the following table:

κ^{-1}	pH	
nm	7.6	8.4
0.5	3	17.6
4	1.4	8.6
7	1.2	7.7
14	1.2	7.3
21	1.2	7.3

C. Details of Analysis for Optical Measurements:

Interferometry:

Optical images are background-corrected using a separate image with no features in the field of view. The background image is smoothed using a moving average, on which each smoothed pixel value is the average of a square grid of pixels around it. The smoothed background intensity data is subtracted from the interferometry picture. Near the perimeter of the image there are not enough pixels to compute the average for a grid of the desired size. Pixels where this is the case are excluded from the analysis.

The oxide thickness was measured using interferometry. The oxide thickness controls the interference at the crack tip such that it can be determined from the pixel intensity as $D \rightarrow 0$. In practice, identifying the crack tip in the image can be difficult due to noise. In most cases we found that the intensity at $D = 0$, i.e. where the glass and oxide are directly bonded, was not independent of position; it increased as a function of x -distance from the crack tip. The intensity as the crack begins to open is known from calculation to increase as a function of x -distance from the crack tip. Thus the intensity passes through a minimum moving from the bonded section to the opening of the crack. The location of the minimum in intensity was regarded as the crack tip in our analysis. We estimate that there is an error of about 2 nm in determining $D = 0$.

Calculating D using the interference pattern involves inverting a squared cosine. The inverse becomes very steep at the limits of its domain, -1 and 1. This means that the measurement of D becomes very sensitive to noise in pixel intensity near points of total constructive and destructive interference. In order to mitigate this issue we smooth over a larger range of pixels near these points. To reduce noise in the interferometry data, we smooth the entire array of pixel intensities using a moving average. The span of the average, i.e. the size of the pixel grid averaged for each point, grows as a function of the gradient in intensity such that it is maximized at intensity maxima and minima (zero gradient) and minimized between. For example, the grid was 13×13 pixels (about $9 \mu\text{m}$ wide) at the maximum and 5×5 pixels (about $3.5 \mu\text{m}$ wide) at the inflection. In the proximity of the crack tip we make an exception to this rule and use minimal smoothing (5×5 pixels) so as not to bias the position of this intensity minimum.

Fluorescence:

The background correction for the fluorescence images is the same as for the interferometry images. The fluorescent intensity data is not smoothed.

Intensity vs Separation:

A separation is computed for each pixel in the interferometry image (where there is a crack) and is mapped to the corresponding pixel in the fluorescence image to give fluorescent intensity as a function of separation. The intensity values are corrected to be zero in the limit of $D \rightarrow 0$ by subtracting the average of the 100 lowest D data points where $D > 0$. These 100 data points spanned a range of less than 0.1 nm.

Supporting information for
**The Electrostatic Screening-Length in Concentrated
Salt Solutions**

Prudhvidhar Gaddam[†] and William Ducker*
Department of Chemical Engineering and Center for Soft Matter and Biological Physics, Virginia Tech,
Blacksburg, VA 24061, USA.

*For correspondence: wducker@vt.edu

Table S1. Refractive indices for concentrated salt solutions

Salt Type	Salt concentration (mol/L)	Refractive index		
		$\lambda = 445 \text{ nm}$	$\lambda = 470 \text{ nm}$	$\lambda = 525 \text{ nm}$
LiCl	0.5	1.3363	1.3374	1.3363
	2.5	1.3527	1.3529	1.3529
	4	1.3645	1.3643	1.3643
	5.5	1.3757	1.3758	1.3758
	7	1.3854	1.3851	1.3850
	10	1.4055	1.4052	1.4052
CsCl	0.5	1.3429	1.3428	1.3412
	2.5	1.3653	1.3652	1.3644
	4	1.3821	1.3820	1.3818
	5.5	1.3991	1.3990	1.3990
NaCl	0.5	1.3463	1.3447	1.3484
	2.5	1.3587	1.3592	1.3596
	4	1.3680	1.3678	1.3679
	5.5	1.3797	1.3795	1.3796

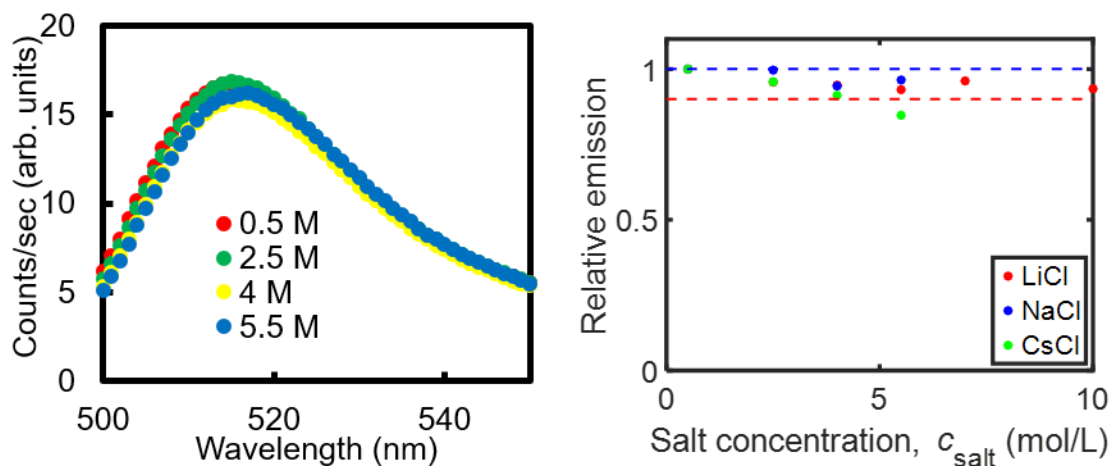


Figure S1. Left: Fluorescence emission of 15 μM aqueous fluorescein solutions for various NaCl salt concentrations. The measured range is from 500 to 550 nm to match the range of the emission filter (550 ± 25 nm) used when measuring the surface excess. Even very large concentrations of salt have a small effect on the spectrum. Fluorescence emission was measured with a Horiba FluoroMax fluorimeter with 475 nm excitation. Right: Relative emission of a 15 μM solution of fluorescein solutions for the different salt types and salt concentrations tested in this work. We define relative emission as:

$$\frac{\text{integral of spectrum for metal chloride solution}}{\text{integral of spectrum for same fluorescein concentration and 0.5 M metal chloride}}$$

The majority of the data has a relative emission of 1 and 0.9 as indicated by the dashed lines. The exception is 5.5 M CsCl, which is 16% less than that of a reference 0.5 M CsCl solution. Since the fluorescence emission of fluorescein solutions is weakly affected by Li^+ and Na^+ concentration, then:

- We are able to use the 0.5 M solution to calibrate the intensity-amount relationship.
- We consider it very unlikely that concentrated salt affects dissociation of fluorescein. The fluorescence spectrum of fluorescein is strongly affected by the degree of dissociation of fluorescein.¹¹⁵

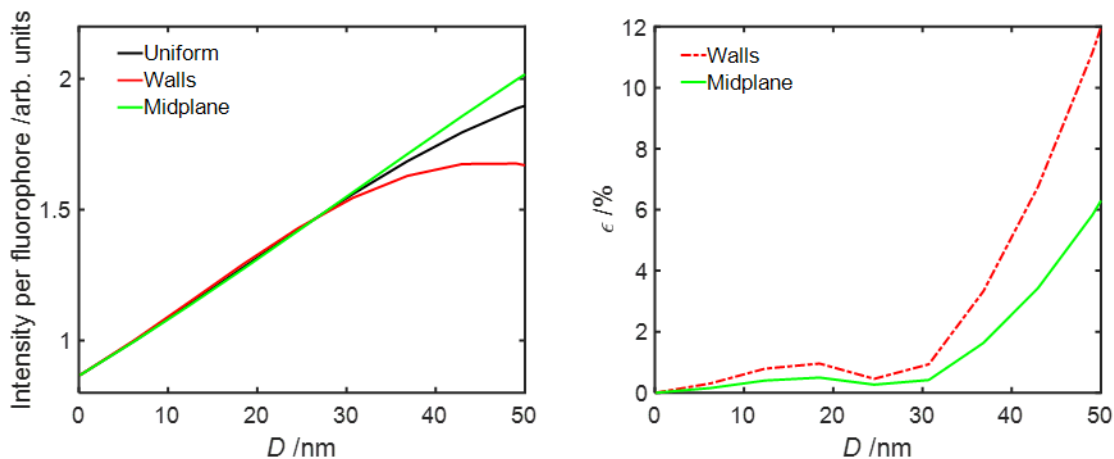


Figure S2. Optical modelling showing the effect of molecular distribution on fluorescence emission. These plots show how the emission is expected to vary for three different z -distributions of molecules: uniform, all molecules at the walls ($z=-D/2$ and $z=D/2$), or all molecules at the midplane ($z=0$). Differences arise because of optical interference in the optical excitation.

Left: Intensity per fluorophore, calculated using the optical model from our earlier publication¹⁰⁹ using an oxide thickness of 41 nm and a fluorescein solution of refractive index, $n = 1.41$, for three examples of fluorophore distribution: uniform, all molecules at the walls ($z=-D/2$ and $z=D/2$), or all molecules at the midplane ($z=0$). At $D > 30$ nm there is a divergence of the emission from the three different molecular distributions.

Right: Calculated error as a result of assuming that the distribution is uniform when the molecules are either all at the surface or all at the midplane. $\epsilon = \frac{I_{\text{Walls or Midplane}}}{I_{\text{Uniform}}} \times 100\%$. For example, at $D = 50$ nm, if the all fluorophores were all at the walls, our assumption that the distribution were uniform would result in an underestimation of the number of fluorophores by $\approx 12\%$. In order to limit this error from dominating our surface excess results, the paper only displays results in the range 0–30 nm. The uncertainty due to the distribution is seen to be relatively low ($< 2\%$) in this range.

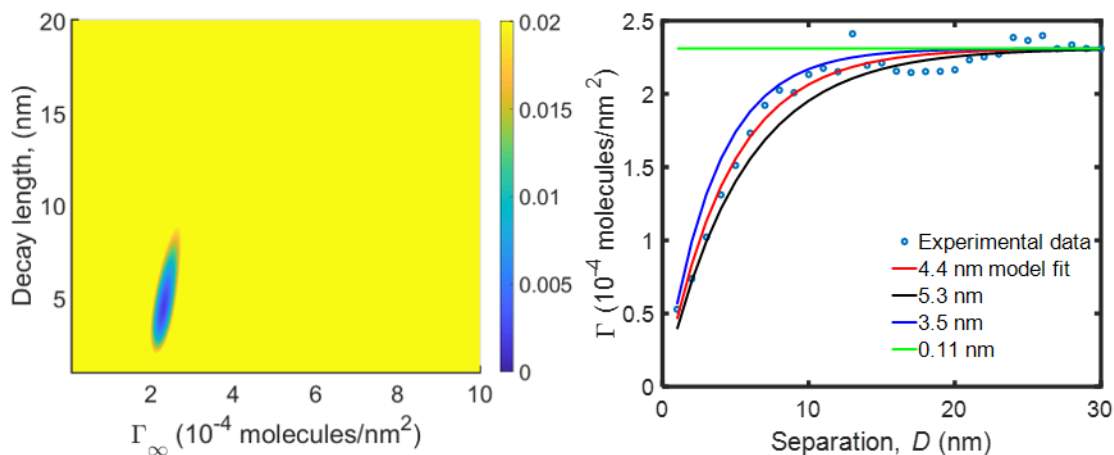


Figure S3. Uncertainty in the fit of the Decay-length from the empirical equation (Eq. 4)

Left: Error heat map showing the least-squared sum of deviations between experimental data from one chip (4 M LiCl) and the surface excess obtained from the empirical model for the surface excess (Eq. 4) for a matrix of terminal surface excesses (Γ_∞) and decay-lengths (κ_E^{-1}). The fit was done over the range 0–30 nm. Color indicates extent of deviation. The minimum error sum is about 0.002 (blue) corresponding to a terminal surface excess of $\Gamma_\infty = 2.31$ molecules/nm² and $\kappa_E^{-1} = 4.4$ nm. The heat map shows that there is a unique minimum, and that the minimum well is narrower in the terminal surface excess than the decay-length.

Right: Experimental data from one chip (4 M LiCl) and four different curves calculated using Eq. 4: red is the best fit of the decay length, the black line was calculated using 120% of the best fit decay length, the blue line 80% of the best fit decay length, and green used a fixed decay length equal to the Debye-length for a 4 M LiCl solution (0.11 nm). Clearly the Debye-length does not allow a good fit.

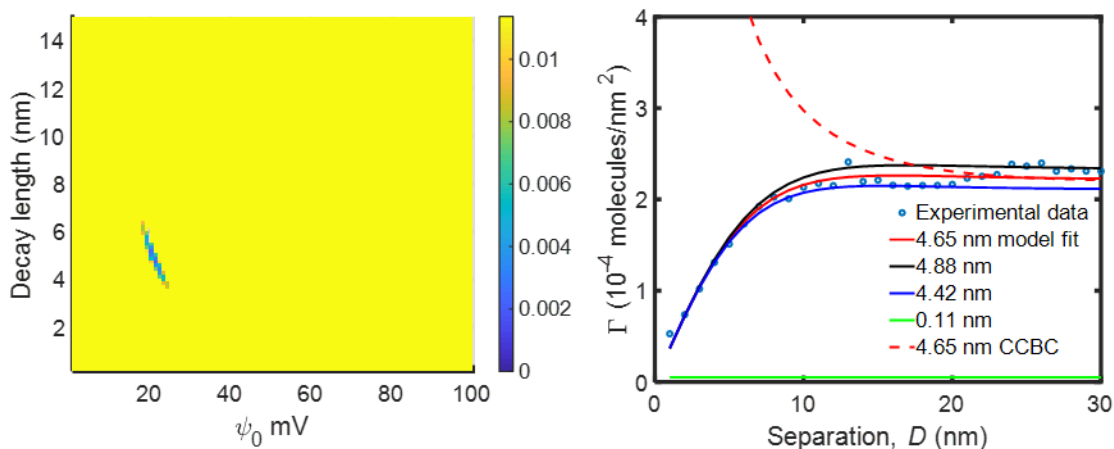


Figure S4. Uncertainty in the fit of the Decay-length from the modified Poisson-Boltzmann equation.

Left: Error heat map showing the least-squared sum of deviations between experimental data from one chip (4 M LiCl) and the surface excess obtained from the analytic low-potential solution of the Poisson-Boltzmann equation (Eq. 6) for a matrix of surface potentials and decay-lengths. The fit was done over the range 0–30 nm. Color indicates extent of deviation. The minimum error sum is about 0.002 (blue) corresponding to a surface potential of $\psi_0 = 21$ mV and $\kappa_F^{-1} = 4.65$ nm. The heat map shows that there is a unique minimum, and that the minimum well is narrow in potential but relatively broad in decay-length, stretching from about 4–6 nm.

Right: Experimental data from one chip (4 M LiCl) and four different theoretical curves using the best fit potential from Eq. 6, but different decay lengths: red is the best fit of the decay length, the black line was calculated using 95% of the best fit decay length, the blue line 105% of the best fit decay length, and green line is the best fit when the decay length was fixed as the Debye-length for a 4 M LiCl solution (0.11 nm). Clearly the Debye-length does not provide a good fit, and the uncertainty of the decay length in the fit is small – a fraction of a nm. The dashed red line is the exact numerical solution with a constant charge boundary condition (CCBC). For this calculation we used the same surface charge density at infinite separation and decay length that were obtained for the best fit at constant potential, $\sigma_0 = 0.000954$ charges/nm². Clearly the constant charge boundary condition is not even qualitatively consistent with the measured data because the measured density of fluorescein does not rise as the separation decreases. According to PB theory, the surface excess is more sensitive to surface charge regulation than the surface forces.

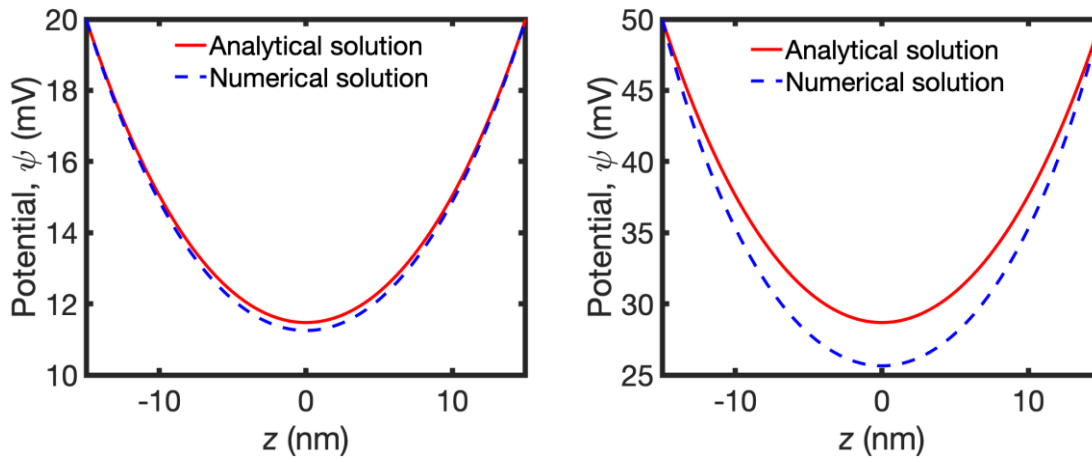


Figure S6. Comparison of exact numerical solution and low-potential analytical solution of the modified Poisson-Boltzmann equation for the constant potential boundary condition.

Left: Comparison of analytical solution for the low-potential approximation and exact numerical solution of the Poisson-Boltzmann equation for a surface potential, ψ_0 of 20 mV, a decay length κ^{-1} of 13 nm and total film thickness, $D = 30$ nm.

Right: Potential plot for the same decay length and total film thickness, but for a greater surface potential, ψ_0 of 50 mV. The plots show that low potential approximation has an increasing error as the potential grows, as expected. This error translates into an error in the Decay-length used to fit our surface excess measurements. For $\psi_0 < 25$ mV, the error in Decay length was $< 2\%$, for 10 M LiCl ($\psi_0 = 45$ mV) the error was 10%.

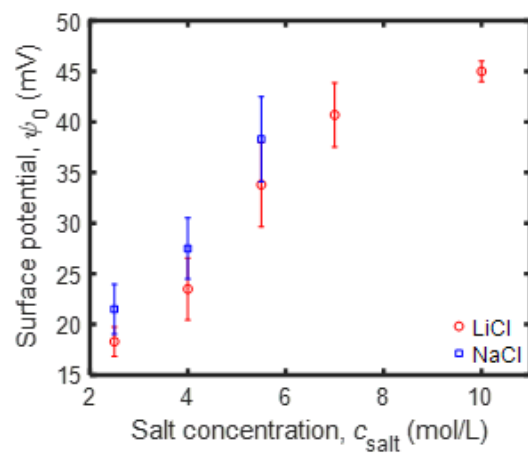


Figure S7. Fitted surface potentials as a function of salt concentration for LiCl and NaCl. The error bars represent standard error for the fitted potential from 4 experimental repeats.

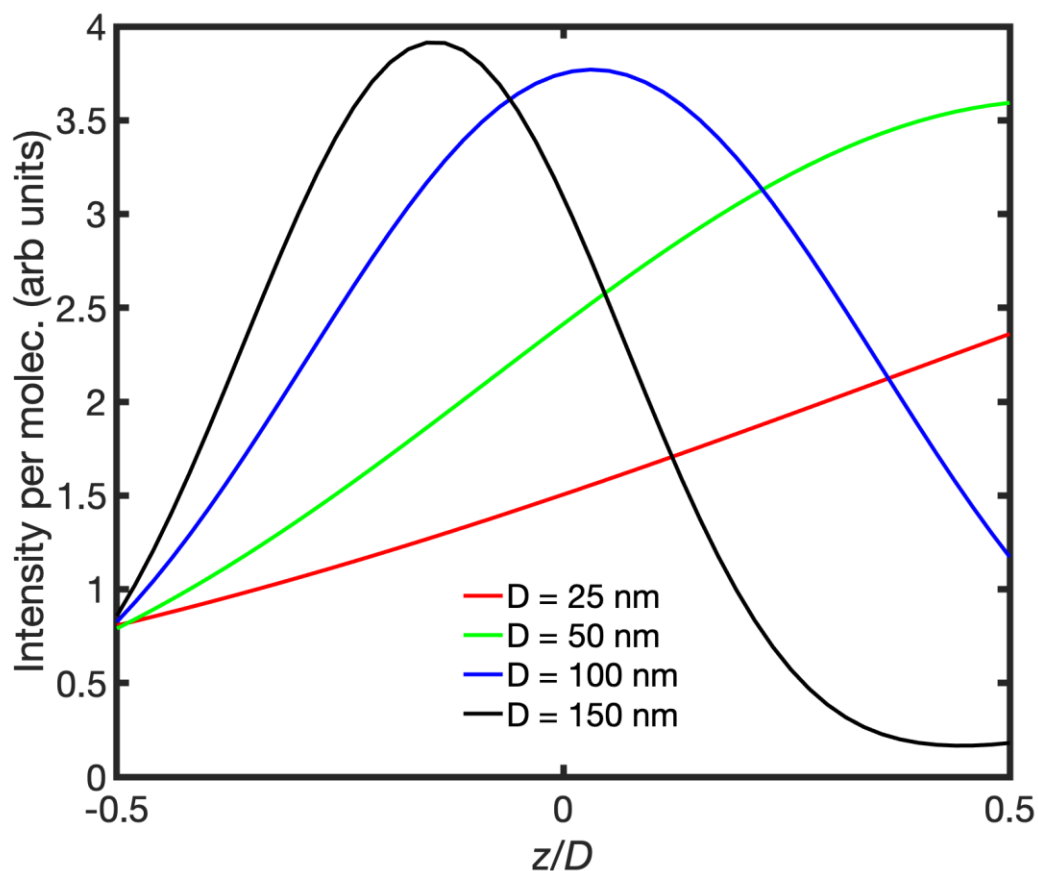


Figure S8. Optical model showing intensity per molecule as a function of position in the film for various film thicknesses. $z/D = 0$ is the midplane and $z/D = -0.5$ are the silicon-oxide-solution and $z/D = 0.5$ are the glass-solution interfaces respectively. Although the overall shape of the curves is similar when plotted on a z -axis, the relative contribution from different parts of the film varies greatly. For a 25 nm film, the emission intensity for a molecule at the glass-solution interface is about $2.5\times$ greater than for a molecule at the silicon-oxide-solution interface. For a 150 nm thick film, the roles are reversed: the intensity is about $4\times$ greater at the silicon-oxide-water interface.

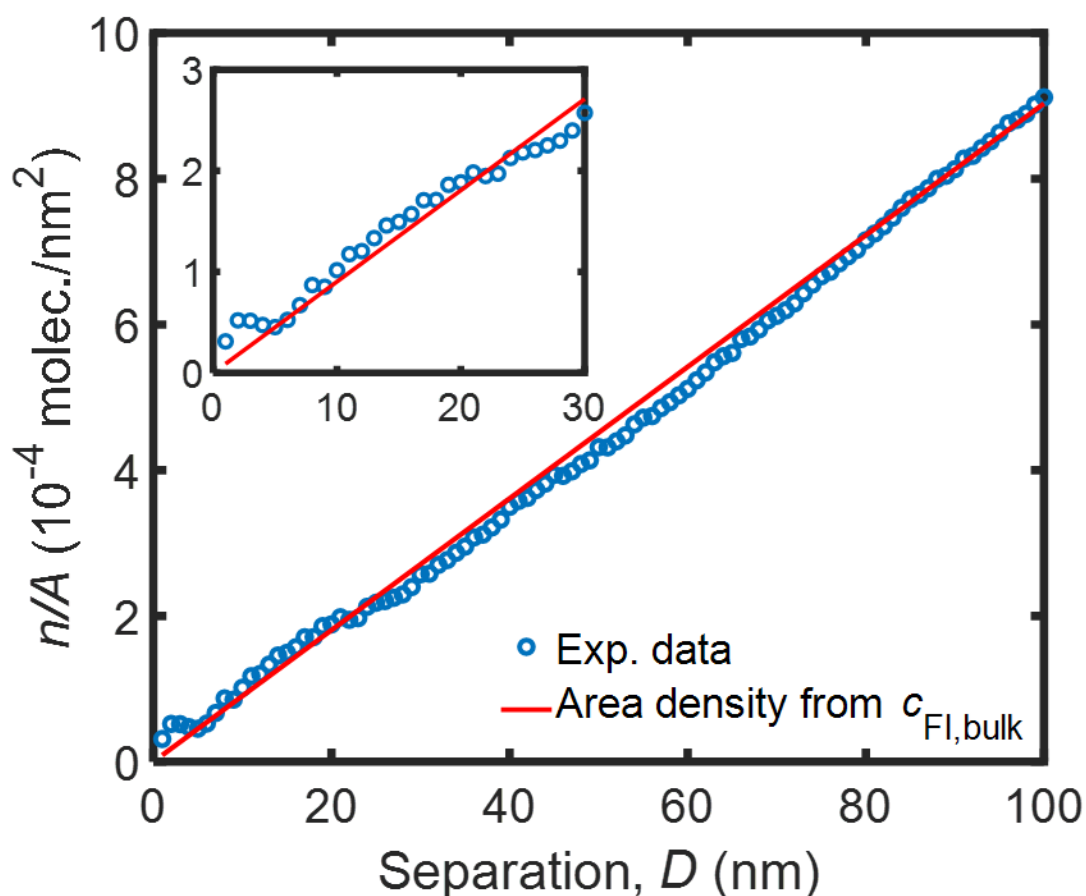


Figure S9. The number of fluorescein molecules per unit area between the two solid–liquid interfaces. The red line assumes that the concentration in the film is the bulk concentration for all thicknesses of film. The red line is the bulk concentration (determined from the mass, molecular mass and volume of the solution) multiplied by the thickness of the film. The blue circles are intensity measurements divided by a single calibration constant, the intensity per molecule, obtained from the fit in Fig 10. The close agreement between the model and the experiment in the region 0–20 nm shows that bulk solution extends all the way to the crack tip: there is no surface excess or no long-range decay in 0.5 M LiCl solution, which is a stark contrast to results in the more concentrated solutions. The inset shows more detail of the thin film region, $D = 0 - 30$ nm.

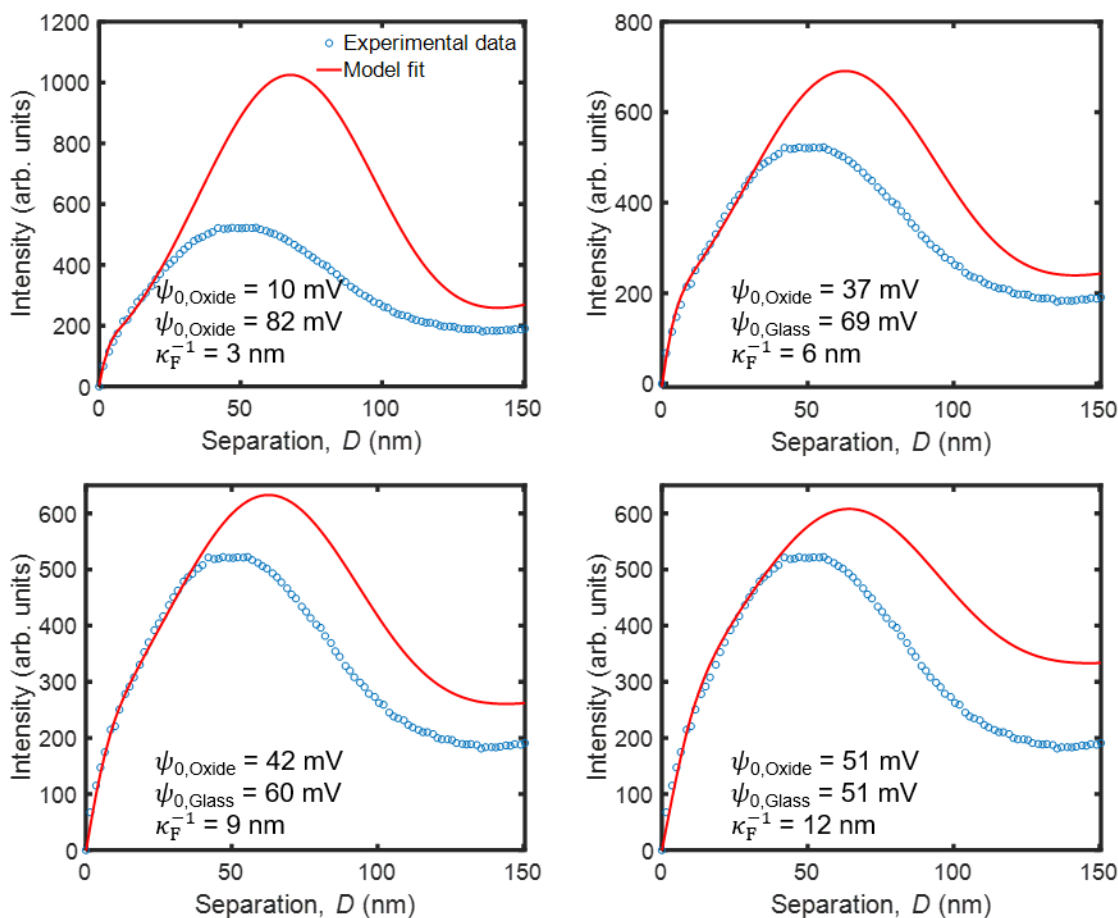


Figure S10. Effect of asymmetry on the fit of the decay length. The glass contains 13% boron, 4% sodium and 2% aluminum substitution for silicon, which could result in a difference in charging behavior between the glass–solution interface and the silicon–oxide–solution interface. In this figure, we have examined how a different potential on each surface affects the PB fit to the data for the 10 M LiCl experiment over the range of $D = 0\text{--}30$ nm. These fits are for the exact numerical solution to PB equation, assuming that the interface potential is independent of D . These are significant assumptions. Each figure shows the best fit for a particular decay-length that is indicated. The fits are reasonable over $0\text{--}30$ nm for all the decay lengths. However, an increasing degree of asymmetry in potential is required for a lower decay length. We consider a large asymmetry to be unlikely. In addition, for the 3 and 6 nm decay lengths, the fit becomes qualitatively more unreasonable for larger separations. The best fit for the asymmetric potentials (decay = 9 nm) is better than the best for symmetric potentials (decay = 12 nm). This is necessarily true because there is an additional fit parameter: the degree of asymmetry.

Summary: In this manuscript we have assumed that the surface potentials are symmetric, but the analysis above suggests that the data could be better fit with an asymmetric potential. The conclusions of the paper would still be retained by allowing asymmetry of the potentials, but it is not clear that the additional degree of freedom in the analysis is justified for a model that already has significant assumptions (functional form of solution to PB equation, constant potential, decay length independent of confinement)

Appendix C: Methods for fabrication of silica-glass and glass-glass cracks

C1. Silica-glass cracks

In the clean room,

1. Turn on furnace and set to 600°C. Set valve in the back to “dry oxide” and turn on N₂ for 1 L/min
2. While furnace is ramping up, set up nanostrip bath in a 2L beaker and heat to 75°C. Place glass wafer in nano-strip while it is heating up and leave it in there. Place a smaller 1 L beaker filled with DI water next to the hot-plate
3. Pour 10:1 BOE in a Teflon container and place silicon wafer to strip the native oxide
4. Remove silicon wafer from Teflon container using Teflon forceps and rinse under running DI water
5. Dry Si wafer using N₂ and place in quartz wafer boat and insert it into the furnace. Make sure the wafer is in line with the middle thermocouple in the furnace
6. Ramp temperature up to 1050°C
7. Once temperature in furnace reaches 1050°C turn on O₂ to 1 L/min and leave on for 16.5 minutes to grow a 37 nm thin film of oxide on the surface
8. After 16.5 minutes are up turn furnace down to room temperature and turn on N₂ flow into the furnace
9. While furnace is cooling, remove glass wafer from nanostrip bath and immediately dip in the DI water to rinse nanostrip. Subsequently rinse the wafer under DI water and place in SRD spinner to rinse and dry
10. At the end of the dry cycle, the glass wafer should be dry and the temperature in the furnace should be < 750°C. If it is, remove the silicon wafer from the furnace and turn off N₂.
11. Turn on wafer bonder and use recipe “Anodic_Gaddam_2”. This should have a voltage of -1000 V, a tool force of 1 bar and temperature of 235°C with the system set to stop once the current reaches 5% of the max value.
12. Place Si wafer on sample holder and place the glass wafer on top of the Silicon wafer
13. Start recipe using the wafer-bonder interface
14. Clean up chemicals appropriately
15. Once recipe is complete, retrieve bonded construct from wafer bonder
16. Break up wafer into individual chips using a diamond scribe.

C2. Glass-glass cracks

In the clean room

1. Set up nanostrip bath in a 2L beaker and heat to 75°C. Place 2 glass wafers in nano-strip while it is heating up and leave them in there. Place a smaller 1 L beaker filled with DI water next to the hot-plate
2. Treat glass wafers for 15 minutes
3. Once 15 minutes are over, remove the glass wafers one by one and rinse nanostrip by immersing it in DI water beaker
4. Rinse again under running DI water and place wafer in wafer boat for SRD spinner
5. Repeat step 3 for second wafer
6. Rinse and dry using the standard setting (200 second rinse, 300 second dry at 2000 rpm) on the SRD spinner

7. Dry with N_2 again after removing from the wafer boat.
8. Bring the two wafers together and align them by lightly gripping both wafers by the edge.
9. Push the two wafers together in the middle. A bond should spontaneously form and propagate to the edge of the wafer leave a small crack at the edge. Place the bonded wafer into an airtight container and transport it back to Goodwin

In our lab

1. Heat furnace to 350°C . Let it run for ~ 1 hour at this temperature to burn off any organic contaminants that may be present in the furnace
2. Place wafer on a ceramic tile inside the wafer. Leave it in there for 1 hour
3. Retrieve wafer from the furnace and cleave into individual chips using a diamond scribe

References

1. Lambourne, R.; Strivens, T., *Paint and surface coatings: theory and practice*. Elsevier: 1999.
2. Whitby, K.; Husar, R.; Liu, B., The aerosol size distribution of Los Angeles smog. *Journal of Colloid and Interface Science* **1972**, *39* (1), 177-204.
3. Hierrezuelo, J.; Sadeghpour, A.; Szilagyi, I.; Vaccaro, A.; Borkovec, M., Electrostatic stabilization of charged colloidal particles with adsorbed polyelectrolytes of opposite charge. *Langmuir* **2010**, *26* (19), 15109-15111.
4. Zhulina, E. B.; Borisov, O. V.; Priamitsyn, V. A., Theory of steric stabilization of colloid dispersions by grafted polymers. *Journal of colloid and interface science* **1990**, *137* (2), 495-511.
5. Vincent, B., The van der Waals attraction between colloid particles having adsorbed layers. II. Calculation of interaction curves. *Journal of Colloid and Interface Science* **1973**, *42* (2), 270-285.
6. Louis, A.; Allahyarov, E.; Löwen, H.; Roth, R., Effective forces in colloidal mixtures: From depletion attraction to accumulation repulsion. *Physical Review E* **2002**, *65* (6), 061407.
7. Tribet, C.; Audebert, R.; Popot, J.-L., Stabilization of hydrophobic colloidal dispersions in water with amphiphilic polymers: application to integral membrane proteins. *Langmuir* **1997**, *13* (21), 5570-5576.
8. Pacheco, L. F.; Carmona-Ribeiro, A. M., Effects of synthetic lipids on solubilization and colloid stability of hydrophobic drugs. *Journal of colloid and interface science* **2003**, *258* (1), 146-154.
9. Romero-Cano, M.; Martín-Rodríguez, A.; Chauveteau, G.; De Las Nieves, F., Colloidal stabilization of polystyrene particles by adsorption of nonionic surfactant: II. Electrosteric stability studies. *Journal of colloid and interface science* **1998**, *198* (2), 273-281.
10. Berg, J. C., *An introduction to interfaces & colloids: the bridge to nanoscience*. World Scientific: 2010.
11. Ducker, W. A.; Senden, T. J.; Pashley, R. M., Direct measurement of colloidal forces using an atomic force microscope. *nature* **1991**, *353* (6341), 239.
12. Israelachvili, J. N.; Adams, G. E., Measurement of forces between two mica surfaces in aqueous electrolyte solutions in the range 0–100 nm. *Journal of the Chemical Society, Faraday Transactions 1: Physical Chemistry in Condensed Phases* **1978**, *74*, 975-1001.
13. Hermansson, M., The DLVO theory in microbial adhesion. *Colloids and Surfaces B: Biointerfaces* **1999**, *14* (1-4), 105-119.
14. Yotsumoto, H.; Yoon, R.-H., Application of extended DLVO theory: I. Stability of rutile suspensions. *Journal of colloid and interface science* **1993**, *157* (2), 426-433.
15. Yoon, R.-H.; Mao, L., Application of extended DLVO theory, IV: derivation of flotation rate equation from first principles. *Journal of Colloid and Interface Science* **1996**, *181* (2), 613-626.
16. Yotsumoto, H.; Yoon, R.-H., Application of extended DLVO theory: II. Stability of silica suspensions. *Journal of Colloid and Interface Science* **1993**, *157* (2), 434-441.
17. Yoon, R.-H.; Ravishankar, S., Application of extended DLVO theory: III. Effect of octanol on the long-range hydrophobic forces between dodecylamine-coated mica surfaces. *Journal of colloid and interface science* **1994**, *166* (1), 215-224.
18. Lhoest, J. B.; Detrait, E.; Van Den Bosch De Aguilar, P.; Bertrand, P., Fibronectin adsorption, conformation, and orientation on polystyrene substrates studied by radiolabeling, XPS, and ToF SIMS. *Journal of Biomedical Materials Research: An Official Journal of The Society for Biomaterials, The Japanese Society for Biomaterials, and the Australian Society for Biomaterials* **1998**, *41* (1), 95-103.
19. Olivares, O.; Likhanova, N.; Gomez, B.; Navarrete, J.; Llanos-Serrano, M.; Arce, E.; Hallen, J., Electrochemical and XPS studies of decylamides of α -amino acids adsorption on carbon steel in acidic environment. *Applied Surface Science* **2006**, *252* (8), 2894-2909.
20. Browne, M.; Lubarsky, G.; Davidson, M.; Bradley, R., Protein adsorption onto polystyrene surfaces studied by XPS and AFM. *Surface Science* **2004**, *553* (1-3), 155-167.

21. Bowker, M.; Madix, R., XPS, UPS and thermal desorption studies of alcohol adsorption on Cu (110): I. Methanol. *Surface Science* **1980**, *95* (1), 190-206.
22. Bowker, M.; Madix, R., XPS, UPS and thermal desorption studies of alcohol adsorption on Cu (110): II. Higher alcohols. *Surface Science* **1982**, *116* (3), 549-572.
23. Marchon, B.; Carrazza, J.; Heinemann, H.; Somorjai, G., TPD and XPS studies of O₂, CO₂, and H₂O adsorption on clean polycrystalline graphite. *Carbon* **1988**, *26* (4), 507-514.
24. Homola, J.; Yee, S. S.; Gauglitz, G., Surface plasmon resonance sensors. *Sensors and Actuators B: Chemical* **1999**, *54* (1-2), 3-15.
25. Tulpar, A.; Ducker, W. A., Surfactant Adsorption at Solid– Aqueous Interfaces Containing Fixed Charges: Experiments Revealing the Role of Surface Charge Density and Surface Charge Regulation. *The Journal of Physical Chemistry B* **2004**, *108* (5), 1667-1676.
26. Mrksich, M.; Sigal, G. B.; Whitesides, G. M., Surface plasmon resonance permits in situ measurement of protein adsorption on self-assembled monolayers of alkanethiolates on gold. *Langmuir* **1995**, *11* (11), 4383-4385.
27. Luk, Y.-Y.; Kato, M.; Mrksich, M., Self-assembled monolayers of alkanethiolates presenting mannitol groups are inert to protein adsorption and cell attachment. *Langmuir* **2000**, *16* (24), 9604-9608.
28. Sigal, G. B.; Bamdad, C.; Barberis, A.; Strominger, J.; Whitesides, G. M., A self-assembled monolayer for the binding and study of histidine-tagged proteins by surface plasmon resonance. *Analytical Chemistry* **1996**, *68* (3), 490-497.
29. Mishra, S. K.; Tripathi, S. N.; Choudhary, V.; Gupta, B. D., SPR based fibre optic ammonia gas sensor utilizing nanocomposite film of PMMA/reduced graphene oxide prepared by in situ polymerization. *Sensors and Actuators B: Chemical* **2014**, *199*, 190-200.
30. Liedberg, B.; Nylander, C.; Lunström, I., Surface plasmon resonance for gas detection and biosensing. *Sensors and actuators* **1983**, *4*, 299-304.
31. Fujimori, A.; Naito, H.; Miyazaki, T., Adsorption of complement, cytokines, and proteins by different dialysis membrane materials: evaluation by confocal laser scanning fluorescence microscopy. *Artificial organs* **1998**, *22* (12), 1014-1017.
32. Anikin, K.; Röcker, C.; Wittemann, A.; Wiedenmann, J.; Ballauff, M.; Nienhaus, G. U., Polyelectrolyte-mediated protein adsorption: fluorescent protein binding to individual polyelectrolyte nanospheres. *The Journal of Physical Chemistry B* **2005**, *109* (12), 5418-5420.
33. Huang, L.-C. L.; Chang, H.-C., Adsorption and immobilization of cytochrome c on nanodiamonds. *Langmuir* **2004**, *20* (14), 5879-5884.
34. Regismond, S. T.; Heng, Y.-M.; Goddard, E. D.; Winnik, F. M., Fluorescence microscopy observation of the adsorption onto hair of a fluorescently labeled cationic cellulose ether. *Langmuir* **1999**, *15* (8), 3007-3010.
35. Kargar, M.; Chang, Y.-R.; Khalili Hoseinabad, H.; Pruden, A.; Ducker, W. A., Colloidal crystals delay formation of early stage bacterial biofilms. *ACS Biomaterials Science & Engineering* **2016**, *2* (6), 1039-1048.
36. Rodahl, M.; Höök, F.; Fredriksson, C.; Keller, C. A.; Krozer, A.; Brzezinski, P.; Voinova, M.; Kasemo, B., Simultaneous frequency and dissipation factor QCM measurements of biomolecular adsorption and cell adhesion. *Faraday Discussions* **1997**, *107*, 229-246.
37. Wang, L.; Xu, G.; Shi, Z.; Jiang, W.; Jin, W., Quantification of protein based on single-molecule counting by total internal reflection fluorescence microscopy with adsorption equilibrium. *Analytica chimica acta* **2007**, *590* (1), 104-109.
38. Hoffmann, F. M., Infrared reflection-absorption spectroscopy of adsorbed molecules. *Surface Science Reports* **1983**, *3* (2-3), 107-192.
39. Bedzyk, M. J.; Bommarito, G. M.; Caffrey, M.; Penner, T. L., Diffuse-double layer at a membrane-aqueous interface measured with x-ray standing waves. *Science* **1990**, *248* (4951), 52-56.

40. Biswas, S.; Chatteraj, D., Kinetics of adsorption of cationic surfactants at silica-water interface. *Journal of colloid and interface science* **1998**, *205* (1), 12-20.
41. Velegol, S. B.; Fleming, B. D.; Biggs, S.; Wanless, E. J.; Tilton, R. D., Counterion effects on hexadecyltrimethylammonium surfactant adsorption and self-assembly on silica. *Langmuir* **2000**, *16* (6), 2548-2556.
42. Eskilsson, K.; Yaminsky, V., Deposition of Monolayers by Retraction from Solution: Ellipsometric Study of Cetyltrimethylammonium Bromide Adsorption at Silica– Air and Silica– Water Interfaces. *Langmuir* **1998**, *14* (9), 2444-2450.
43. Wängnerud, P.; Berling, D.; Olofsson, G., Adsorption of alkyltrimethylammonium bromides on silica: calorimetric study of effect of coions. *Journal of colloid and interface science* **1995**, *169* (2), 365-375.
44. Rennie, A.; Lee, E.; Simister, E.; Thomas, R., Structure of a cationic surfactant layer at the silica-water interface. *Langmuir* **1990**, *6* (5), 1031-1034.
45. Wang, J.; Caffrey, M.; Bedzyk, M. J.; Penner, T. L., Direct Profiling and Reversibility of Ion Distribution at a Charged Membrane/Aqueous Interface: An X-ray Standing Wave Study. *Langmuir* **2001**, *17* (12), 3671-3681.
46. Ash, S. G.; Everett, D. H.; Radke, C., Thermodynamics of the Effects of Adsorption on Interparticle Forces. *J. Chem. Soc. Faraday Trans. II* **1972**, *69*, 1256-1277.
47. Hall, D. G., Thermodynamic Treatment of Some Factors Affecting the Interaction Between Colloidal Particles. *J. Chem. Soc. Faraday Trans. II* **1972**, *68*, 2169-2182.
48. Subramanian, V.; Ducker, W., Proximal adsorption of cationic surfactant on silica at equilibrium. *The Journal of Physical Chemistry B* **2001**, *105* (7), 1389-1402.
49. Lokar, W. J.; Ducker, W. A., Proximal adsorption at glass surfaces: Ionic strength, pH, chain length effects. *Langmuir* **2004**, *20* (2), 378-388.
50. Lokar, W. J.; Ducker, W. A., Proximal Adsorption of Dodecyltrimethylammonium Bromide to the Silica– Electrolyte Solution Interface. *Langmuir* **2002**, *18* (8), 3167-3175.
51. Lokar, W. J.; Ducker, W. A., Forces between Glass Surfaces in Mixed Cationic– Zwitterionic Surfactant Systems. *Langmuir* **2004**, *20* (11), 4553-4558.
52. Fenter, P.; Cheng, L.; Rihs, S.; Machesky, M.; Bedzyk, M. J.; Sturchio, N. C., Electrical double-layer structure at the rutile-water interface as observed in situ with small-period X-ray standing waves. *Journal of Colloid and Interface Science* **2000**, *225* (1), 154-165.
53. Hoogeveen, N. G.; Stuart, M. A. C.; Fleer, G. J., Polyelectrolyte adsorption on oxides .1. Kinetics and adsorbed amounts. *Journal of Colloid and Interface Science* **1996**, *182* (1), 133-145.
54. Israelachvili, J. N., Intermolecular and Surface Forces. 3rd ed.; Academic Press: San Diego, 2011; p 387.
55. Ninham, B. W.; Parsegian, V. A., Electrostatic Potential between Surfaces bearing Ionizable Groups in Ionic Equilibrium with Physiological Saline Solution. *Journal of Theoretical Biology* **1971**, *31*, 405-428.
56. Behrens, S. H.; Borkovec, M., Exact Poisson-Boltzmann solution for the interaction of dissimilar charge-regulating surfaces. *Physical Review E* **1999**, *60* (6), 7040-7048.
57. McCormack, D.; Carnie, S. L.; Chan, D. Y. C., Calculations Of Electric Double-Layer Force And Interaction Free-Energy Between Dissimilar Surfaces. *Journal of Colloid and Interface Science* **1995**, *169* (1), 177-196.
58. Walz, J. Y.; Sharma, A., Effect of long-range interactions on the depletion force between colloidal particles. *Journal of Colloid and Interface Science* **1994**, *168* (2), 485-496.
59. Mao, Y.; Cates, M. E.; Lekkerkerker, H. N. W., Depletion force in colloidal systems. *Physica A* **1995**, *222* (1-4), 10-24.
60. Pethica, B. A., Adsorption Equilibria in Surface Force Balance Studies. *Colloids and Surfaces A*. **1995**, *105*, 257-264.
61. Subramanian, V.; Ducker, W., Proximal adsorption of cationic surfactant on silica at equilibrium. *Journal of Physical Chemistry B* **2001**, *105* (7), 1389-1402.

62. Lokar, W. J.; Ducker, W. A., Proximal adsorption of dodecyltrimethylammonium bromide to the silica-electrolyte solution interface. *Langmuir* **2002**, *18* (8), 3167-3175.
63. Lokar, W. J.; Ducker, W. A., Forces between glass surfaces in mixed cationic-zwitterionic surfactant systems. *Langmuir* **2004**, *20* (11), 4553-4558.
64. Lokar, W. J.; Koopal, L. K.; Leermakers, F. A. M.; Ducker, W. A., Confinement-induced phase behavior and adsorption regulation of ionic surfactants in the aqueous film between charged solids. *Journal of Physical Chemistry B* **2004**, *108* (39), 15033-15042.
65. Ducker, W. A.; Senden, T. J.; Pashley, R. M., Measurement of Forces in Liquids Using a Force Microscope. *Langmuir* **1992**, *8* (7), 1831-1836.
66. Hunter, R. J., *Foundations of Colloid Science*. Oxford Science Publications: Oxford, 1987.
67. Lambacher, A.; Fromherz, P., Fluorescence interference-contrast microscopy on oxidized silicon using a monomolecular dye layer. *Appl. Phys. A-Mater. Sci. Process.* **1996**, *63* (3), 207-216.
68. Hecht, E. H., *Optics*. 4th ed.; Addison-Wesley: Boston, 2001.
69. Section 10 Index of Refraction of Air. In *CRC Handbook of Chemistry and Physics 98th Edition (Internet Version 2018)* Rumble, J. R., Ed. CRC Press/Taylor & Francis: Boca Raton, FL, 2018.
70. BOROFLOAT® 33 – Optical Properties. http://www.schott.com/d/borofloat/bde16ad3-70e5-48a0-b8ac-9146fcd34511/1.0/borofloat33_opt_en_web.pdf (accessed March 16, 2018).
71. Hale, G. M.; Query, M. R., Optical constants of water in the 200-nm to 200- μ m wavelength region. *Applied optics* **1973**, *12* (3), 555-563.
72. Taft, E.; Cordes, L., Optical Evidence for a Silicon-Silicon Oxide Interlayer. *Journal of The Electrochemical Society* **1979**, *126* (1), 131-134.
73. Section 12 Optical Properties of Selected Elements. In *CRC Handbook of Chemistry and Physics 98th Edition (Internet Version 2018)* Rumble, J. R., Ed. CRC Press/Taylor & Francis: Boca Raton, FL, 2018.
74. Stillinger, F., Interfacial solutions of poisson-boltzmann equation. *Journal of Chemical Physics* **1961**, *35* (5), 1584-&.
75. Horn, R.; Smith, D.; Haller, W., Surface forces and viscosity of water measured between silica sheets. *Chemical Physics Letters* **1989**, *162* (4-5), 404-408.
76. Attard, P.; Mitchell, D. J.; Ninham, B. W., Beyond Poisson-Boltzmann - Images And Correlations In The Electric Double-Layer .1. Counterions Only. *Journal of Chemical Physics* **1988**, *88* (8), 4987-4996.
77. Attard, P.; Mitchell, D. J.; Ninham, B. W., Beyond Poisson-Boltzmann - Images And Correlations In The Electric Double-Layer .2. Symmetric Electrolyte. *Journal of Chemical Physics* **1988**, *89* (7), 4358-4367.
78. Ben-Yaakov, D.; Andelman, D.; Harries, D.; Podgornik, R., Beyond standard Poisson-Boltzmann theory: ion-specific interactions in aqueous solutions. *Journal of Physics-Condensed Matter* **2009**, *21* (42).
79. Berg, J., *An Introduction to Interfaces and Colloids*. World Scientific: Singapore, 2010; pp 467-468.
80. Israelachvili, J. N.; Adams, G., Measurement of Forces between Two Mica Surfaces in Aqueous Electrolyte Solutions in the Range 0-100 nm. *J. Chem. Soc., Faraday Trans 1* **1978**, *74*, 975-1001.
81. Pashley, R. M., DLVO and Hydration Forces between Mica Surfaces in Li⁺, Na⁺, K⁺, And Cs⁺ Electrolyte-Solutions - A Correlation of Double-Layer and Hydration Forces with Surface Cation-Exchange Properties. *Journal of Colloid and Interface Science* **1981**, *83* (2), 531-546.
82. Horn, R. G.; Israelachvili, J. N., Direct Measurement of Forces due to Solvent Structure. *Chemical Physics Letters* **1980**, *71* (2), 192-194.
83. Israelachvili, J. N.; Pashley, R. M., Molecular Layering of Water at Surfaces and Origin of Repulsive Hydration Forces. *Nature* **1983**, *306* (5940), 249-250.
84. Perkin, S.; Albrecht, T.; Klein, J., Layering and shear properties of an ionic liquid, 1-ethyl-3-methylimidazolium ethylsulfate, confined to nano-films between mica surfaces. *Physical chemistry chemical physics* **2010**, *12* (6), 1243-1247.

85. Hayes, R.; Borisenko, N.; Tam, M. K.; Howlett, P. C.; Endres, F.; Atkin, R., Double layer structure of ionic liquids at the Au (111) electrode interface: an atomic force microscopy investigation. *The Journal of Physical Chemistry C* **2011**, *115* (14), 6855-6863.
86. Cheng, H. W.; Stock, P.; Moeremans, B.; Baimpos, T.; Banquy, X.; Renner, F. U.; Valtiner, M., Characterizing the Influence of Water on Charging and Layering at Electrified Ionic-Liquid/Solid Interfaces. *Advanced Materials Interfaces* **2015**, *2* (12), 1500159.
87. Ducker, W. A.; Senden, T. J.; Pashley, R. M., Direct Measurement of Colloidal Forces Using an Atomic Force Microscope. *Nature* **1991**, *353* (6341), 239-241.
88. Gebbie, M. A.; Valtiner, M.; Banquy, X.; Fox, E. T.; Henderson, W. A.; Israelachvili, J. N., Ionic liquids behave as dilute electrolyte solutions. *Proceedings of the National Academy of Sciences of the United States of America* **2013**, *110* (24), 9674-9679.
89. Gebbie, M. A.; Dobbs, H. A.; Valtiner, M.; Israelachvili, J. N., Long-range electrostatic screening in ionic liquids. *Proceedings of the National Academy of Sciences of the United States of America* **2015**, *112* (24), 7432-7437.
90. Perkin, S.; Salanne, M.; Madden, P.; Lynden-Bell, R., Is a Stern and diffuse layer model appropriate to ionic liquids at surfaces? *Proceedings of the National Academy of Sciences of the United States of America* **2013**, *110* (44), E4121-E4121.
91. Gebbie, M. A.; Valtiner, M.; Banquy, X.; Henderson, W. A.; Israelachvili, J. N., Reply to Perkin et al.: Experimental observations demonstrate that ionic liquids form both bound (Stern) and diffuse electric double layers. *Proceedings of the National Academy of Sciences of the United States of America* **2013**, *110* (44), E4122-E4122.
92. Lee, A. A.; Vella, D.; Perkin, S.; Goriely, A., Are room-temperature ionic liquids dilute electrolytes? *The journal of physical chemistry letters* **2014**, *6* (1), 159-163.
93. Smith, A. M.; Lee, A. A.; Perkin, S., The Electrostatic Screening Length in Concentrated Electrolytes Increases with Concentration. *Journal of Physical Chemistry Letters* **2016**, *7* (12), 2157-2163.
94. Gebbie, M. A.; Smith, A. M.; Dobbs, H. A.; Lee, A. A.; Warr, G. G.; Banquy, X.; Valtiner, M.; Rutland, M. W.; Israelachvili, J. N.; Perkin, S.; Atkin, R., Long range electrostatic forces in ionic liquids. *Chemical Communications* **2017**, *53* (7), 1214-1224.
95. Hjalmarsen, N.; Atkin, R.; Rutland, M. W., Switchable long-range double layer force observed in a protic ionic liquid. *Chemical Communications* **2017**, *53* (3), 647-650.
96. Lee, A. A.; Perez-Martinez, C. S.; Smith, A. M.; Perkin, S., Scaling Analysis of the Screening Length in Concentrated Electrolytes. *Physical Review Letters* **2017**, *119* (2), 026002.
97. Ludwig, N. B.; Dasbiswas, K.; Talapin, D. V.; Vaikuntanathan, S., Describing screening in dense ionic fluids with a charge-frustrated Ising model. *Journal of Chemical Physics* **2018**, *149* (16).
98. Huang, J., Confinement Induced Dilution: Electrostatic Screening Length Anomaly in Concentrated Electrolytes in Confined Space. *Journal of Physical Chemistry C* **2018**, *122* (6), 3428-3433.
99. Kjellander, R., Nonlocal electrostatics in ionic liquids: The key to an understanding of the screening decay length and screened interactions. *Journal of Chemical Physics* **2016**, *145* (12).
100. Kjellander, R., Focus Article: Oscillatory and long-range monotonic exponential decays of electrostatic interactions in ionic liquids and other electrolytes: The significance of dielectric permittivity and renormalized charges. *Journal of Chemical Physics* **2018**, *148* (19).
101. Kjellander, R.; Marcelja, S.; Pashley, R. M.; Quirk, J. P., Double-Layer Ion Correlation Forces Restrict Calcium Clay Swelling. *Journal of Physical Chemistry* **1988**, *92* (23), 6489-6492.
102. Kjellander, R.; Marcelja, S.; Pashley, R. M.; Quirk, J. P., A Theoretical and Experimental-Study of Forces between Charged Mica Surfaces in Aqueous CaCl₂ Solutions. *Journal of Chemical Physics* **1990**, *92* (7), 4399-4407.

103. Baimpos, T.; Shrestha, B. R.; Raman, S.; Valtiner, M., Effect of Interfacial Ion Structuring on Range and Magnitude of Electric Double Layer, Hydration, and Adhesive Interactions between Mica Surfaces in 0.05–3 M Li⁺ and Cs⁺ Electrolyte Solutions. *Langmuir* **2014**, *30* (15), 4322-4332.
104. Suo, L.; Borodin, O.; Gao, T.; Olguin, M.; Ho, J.; Fan, X.; Luo, C.; Wang, C.; Xu, K., “Water-in-salt” electrolyte enables high-voltage aqueous lithium-ion chemistries. *Science* **2015**, *350* (6263), 938-943.
105. Simon, P.; Gogotsi, Y., Materials for electrochemical capacitors. In *Nanoscience And Technology: A Collection of Reviews from Nature Journals*, World Scientific: 2010; pp 320-329.
106. Li, D.; Chun, J.; Xiao, D.; Zhou, W.; Cai, H.; Zhang, L.; Rosso, K. M.; Mundy, C. J.; Schenter, G. K.; De Yoreo, J. J., Trends in mica–mica adhesion reflect the influence of molecular details on long-range dispersion forces underlying aggregation and coalignment. *Proceedings of the National Academy of Sciences* **2017**, *114* (29), 7537-7542.
107. De Yoreo, J. J.; Gilbert, P. U.; Sommerdijk, N. A.; Penn, R. L.; Whitlam, S.; Joester, D.; Zhang, H.; Rimer, J. D.; Navrotsky, A.; Banfield, J. F., Crystallization by particle attachment in synthetic, biogenic, and geologic environments. *Science* **2015**, *349* (6247), aaa6760.
108. Atkins, P.; de Paula, J., *Physical Chemistry*. Freeman: NY, 2002; p 1101.
109. Gaddam, P.; Grayson, R.; Ducker, W., A., Adsorption at Confined Interfaces. *Langmuir* **2018**, *34* (36), 10469-10479.
110. Qiao, R.; Aluru, N. R., Charge inversion and flow reversal in a nanochannel electro-osmotic flow. *Physical Review Letters* **2004**, *92* (19).
111. Van der Heyden, F. H.; Stein, D.; Besteman, K.; Lemay, S. G.; Dekker, C., Charge inversion at high ionic strength studied by streaming currents. *Physical review letters* **2006**, *96* (22), 224502.
112. Martin, M. M.; Lindqvist, L., The pH dependence of fluorescein fluorescence. *Journal of Luminescence* **1975**, *10* (6), 381-390.
113. Bazant, M. Z.; Storey, B. D.; Kornyshev, A. A., Double layer in ionic liquids: Overscreening versus crowding. *Physical Review Letters* **2011**, *106* (4), 046102.
114. Fedorov, M. V.; Kornyshev, A. A., Ionic Liquids at Electrified Interfaces. *Chem. Rev.* **2014**, *114* (5), 2978-3036.
115. Martin, M. M.; Lindqvist, L. J. J. o. L., The pH dependence of fluorescein fluorescence. **1975**, *10* (6), 381-390.